DI Tobias Abel

Integrated Optical Sensors and Optical Ammonia Sensors

Dissertation

zur Erlangung des akademischen Grades eines
Doktors der technischen Wissenschaften

erreicht an der

Technischen Universität Graz

Univ.-Prof. Dipl.-Chem. Dr.rer.nat. Ingo Klimant
Institut für Analytische Chemie und
Lebensmittelchemie
Technische Universität Graz

Statutory declaration

I declare that I have authored this thesis independently, that I have not used other than the declared sources / resources, and that I have explicitly marked all material which has been quoted either literally or by content from the used sources.

…….. ……..

date (signature)

Acknowledgement

There are of course many people I have to thank for helping and assisting me with this thesis. First of all, my supervisor Torsten Mayr and my PhD advisor Ingo Klimant should be named for helping, assisting and motivating during the thesis. Günter Mistlberger, who was my office colleague for about a year and Birgit Ungerböck, who took his place then for about two years. Also I have to thank Birgit for calculating ratiometric luminescence imaging measurements in MATLAB. Klaus, one of the people I met at the first day of my studies. Sergey Borisov, who helped me in the lab and with whom I shared a lab-office-combination for a year and for all the dyes and indicators he offered me. Philipp Lehner, one of my few project students and helpful counselor in LabVIEW-Issues. Gunter Zenkl, who encouraged me even after he finished his thesis. Fabian Niedermair for synthesizing the $Ir(C_s)_2(acac)$ together with Klaus. Also thanks to Elisabeth Scheucher for the synthesis of ES002-L or OG488StA, to Daniel Aigner and Tijana Jokic for their dyes and indicators. Christian Konrad and Martin Sagmeister for helping and solving all the problems we had with the ISOTEC read-out unit and measurements. Elke Kraker and Bernhard Lamprecht for the continuous supply of organic photo diodes. Eveline for taking over my measurement duties and for helping me to order stuff with the improved ordering system. Also sincere thanks to Rick Baggio for support during the Millipore OAS project and for the free experimental membranes.

Furthermore I really want to thank Clemens Mayer and Johannes Reiter for being the probably most incredible and genuine friends I can imagine, for listening to me complaining or whining about stuff when it was necessary, for experiencing music festivals together, for the Ostereiersuche, for steak nights with Risiko board games and more. Also thank you Georg Oberdorfer and Stefan Lembach, who I must not forget in the context of NARF. And also thanks to my brother, who is a great backer for everything I did and do, even if doesn't realize how much of a backer he is. Thank you to the whole Big Load pubquiz team and friends for accepting me as one of theirs. Thank you Eddie for some party nights. Thank you to the indiepartment for letting me practice my skills concerning concert photography. Thank you to my family for every support I've got during the time of the thesis and before, especially from my grandfather and my mother. And sorry Hedwig that I did not came as often to Leibnitz as I wanted.

And thank you Heike. Sincerely. For everything.

Table of content

Scope of the thesis

Analytical chemistry is a main branch of the chemical sciences. It is required to control development processes of new materials or to monitor known substances in environment and industry. Two main approaches can be simplistically distinguished in analytical chemistry: While the first approach deals with sophisticated laboratory instrumentation and requires predominantly extensive preparation steps carried out by specifically trained personnel, the second approach is aimed to provide cheap and easy to operate instrumentation, which can be used without any sample preparation and outside a laboratory.

Sensors can be attributed to the second approach. Optical sensors are especially noteworthy in this context, since they have found much utilization in academic, industrial, and medical applications in recent decades due to progress in fiber optic technologies, reduced costs of semiconductor devices, development of organic optoelectronics and new chemical compounds. The development of such optical sensors is an interdisciplinary undertaking and requires knowledge from both basic and applied sciences, such as physics, chemistry, material technology, electrical engineering and applied informatics.

This PhD thesis addresses multiple issues regarding the development of optical sensors. It deals with the design of an integrated sensor platform and the combination of already introduced sensor technologies with said platform, the development of sensor technology applicable with pre-existing instrumentation, and the planning as well as programming of easy to use software for the testing of sensors during their research stage. This thesis is based on two research publications, the documentation of the software programming, additional non-published research results and background information.

Theoretical background

Luminescence

Definition and processes

> Luminescence is the emission of light from any substance and occurs from electronically excited states.[1]

The term luminescence is often misused in the meaning of photoluminescence, yet it simply describes the emission of light. The term can be specified by using prefixes such as chemo-, photo- or mechano-, which refers to the source of excitation. Though all luminescence phenomena are scientifically interesting, photoluminescence is the only luminescence phenomenon which will be dealt with in this thesis. The phenomenon of photoluminescence has been known to mankind for some centuries, dating back to at least to 1565[2]. The Jablonski-Diagram (see Figure 1) is helpful for a deeper understanding of photoluminescence and the involved processes.

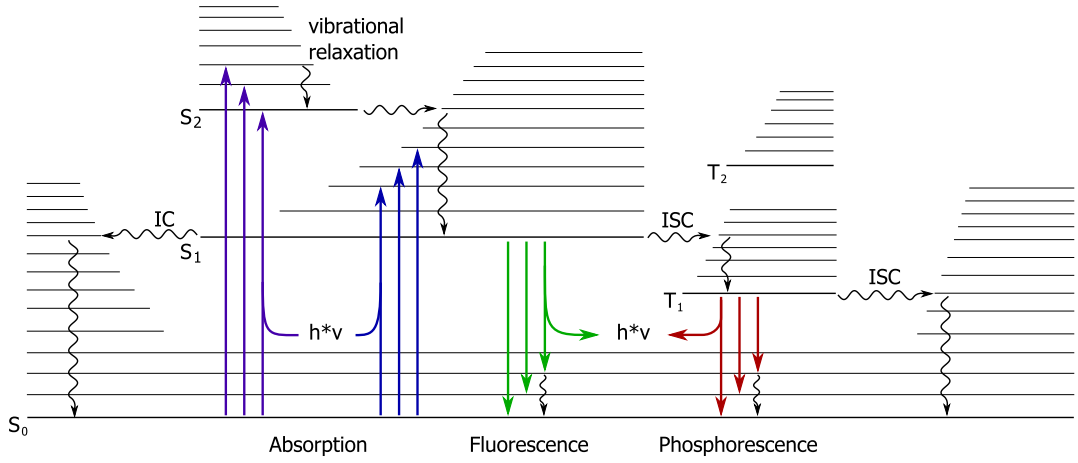

Figure 1: Jablonski-diagram of photoluminescence and other processes occurring during this phenomenon.

Photoluminescence always starts with the absorption of a photon. During this very fast process - it takes about 10^{-15} seconds - an electron takes up the energy of a photon and is lifted into a excited state. For most cases, the starting point is the so called S_0 state, the singlet ground state, and the excited states are called S_1, S_2 or so on for the first excited, second excited state and so on. According to the Frank-Condon principle, the transition - called *vertical transition*[3] - between the ground and an excited state is faster than any vibration relaxation or displacement of the electron in relation to the nuclei or the molecule.

Each state has several vibrational energy levels. The absorption at ambient conditions takes place from the state with the lowest vibrational energy, since the energy is not sufficient to populate higher vibrational energy levels. Also, the high energy gap between S_0 and S_1 is too high to be overcome by thermal energy at room temperature. And even if so, we would not speak of photoluminescence, since the excitation would stem from thermal and not from a photon's energy. Vibrational relaxation takes normally place after the absorption of a photon. This is derived from the Frank-Condon principle, since the absorption is magnitudes faster than the displacement of an electron due to changed electronic states. The duration of vibrational relaxation is about 10^{-12} to 10^{-11} seconds. Only after reaching the lowest vibrational state of S_1, different processes can take place. This rule has a specific impact, to wit that the emission spectrum is not dependent on the wavelength of the absorption ("Kasha's rule").[2]

Internal conversion (IC) is a transition of an electron from a vibrational ground state of an electronic state to a vibrational excited state of a lower electronic state of the same energy and multiplicity. This non-radiative process is normally followed by vibrational relaxation towards the lowest vibrational state of latter electronic state. It takes about 10^{-11} to 10^{-9} seconds. The probability of this process linked to the electronic state, since the energy gap is smaller between higher states and smaller energy gaps facilitate IC. So to say, only internal conversion and vibrational relaxation occur during the de-excitation towards the 0 vibrational state of S_1.[2]

Fluorescence is the main process of relaxation competing to IC. Fluorescence is a relaxation process which occurs between S_1 and S_0, which in contrast to IC, is accompanied by the emission of a photon. The photon's energy corresponds to the relaxation energy between S_1 and S_0 and is always smaller than photon's energy of the absorption. The difference of energy stems from non-radiative deexcitation processes such as the vibrational relaxation. The process of emitting a photon is as fast as absorption, but the excited electron will stay in the S_1 state for about 10^{-11} to 10^{-7} seconds.

Phosphorescence is also a radiative decay of excitation energy, but must not be mistaken as fluorescence. Fluorescence is a spin-conservative process, which normally

occurs between two singlet states. For phosphorescence, the excited electron in the S_1 state undergoes a process called *Intersystem Crossing* (ISC). This process involves a change of spin by an isoenergetic transition from the first excited electronic singlet state S_1 to the first excited electronic triplet state S_1. ISC itself is forbidden, but can be facilitated by heavy atoms in the molecular structure. Also, the transition and radiative decay of T_1 to S_0 is forbidden which results in higher relaxation times. Also due to the ISC and the subsequent vibrational relaxation, the emitted photon of phosphorescence has a longer wavelength (lesser energy) than its counterpart of fluorescence.

Figure 2 gives an overview about the spectral sequence of the different transitions.

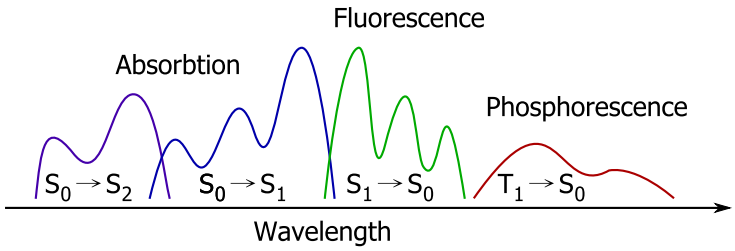

Figure 2: Spectral distribution of transitions occurring during luminescence.

There are more processes of deexcitation, such as conformal change (e.g. Stilben), delayed fluorescence due to thermally activated re-ISC, delayed fluorescence due to triplet-triplet annihilation, FRET (see page 13), electron or proton transfer, exciplex or excimer formation and more; but those processes should not be discussed here[1,2].

Characteristics and parameters

Several parameters characterize luminescence, such as excitation and emission wavelength, Stoke's shift, quantum yield, decay time (lifetime).

A compounds first and obvious characteristic is its absorbance spectrum, specifically if the compound displays absorbance in the visible range. Also, the emission spectrum can be seen without any instrumentation if it is in the visible range. The shape of both spectra can change according to the polarity or the temperature of the environment. Furthermore, the difference "between the maximum of the first absorption band and the maximum of the fluorescence spectrum (expressed in wavenumbers)"[2] is called *Stoke's shift*.

The *quantum yield* Φ is a ratiometric value and compares one or a group of specific deexcitation processes with the entirety of all deexcitation processes. Simplistically speaking, the fluorescence quantum yield indicates how many fluorescence photons are emitted per absorbed photon. Equation 1 shows the calculation of the quantum yield where k_r is the rate constant of radiative decay and k_{nr} is the rate constant of non-radiative decay. This fraction can be expanded for the rate constant of any other process, which might be involved in the deexcitation (e.g. k_{ISC} as the rate constant for ISC)

$$\phi = \frac{k_r}{k_r + k_{nr}} = k_r \cdot \tau \quad (1)$$

The quantum yield is not a constant value for a given molecule; it depends on different parameters, especially temperature and matrix. Quantifying the quantum yield requires pure matrices, because many different compounds can agitate as so called quenchers. Quenchers are decreasing the rate of fluorescence while increasing the rate of non-radiative de-excitation processes.

Quenching can be distinguished in two different types: static quenching and dynamic quenching. Static quenching is the phenomenon which occurs, when the quencher forms a non-fluorescent complex with the former fluorescent dye. Dynamic quenching is based on the presence of some other molecule with which the excited fluorescent dye can interact and so be de-excited. Dynamic quenching can be described by a statistically and is calculated by the Stern-Volmer equation (Equation 2).

$$\frac{I_0}{I} = \frac{\tau_0}{\tau} = \frac{\phi_0}{\phi} = 1 + K_{SV} \cdot [Q] \quad (2)$$

in which I_0 (τ_0, Φ_0) is the fluorescence intensity (lifetime, quantum yield) in the absence of the quencher, I (τ, Φ) is the intensity (lifetime, quantum yield) in the presence of the quencher, K_{SV} is the Stern-Volmer constant and [Q] is the concentration of the quencher.

Measuring luminescence

Fluorescence and phosphorescence are not sudden processes, but display a distinct trend over time. Their time dependent behavior follows a logarithmic decay, similar to the

logarithmic decay of radioactive atoms. τ_S describes the lifetime of the excited state in equation 3 based on rate constant of involved deexcitation processes.

$$\tau_S = \frac{1}{k_r + k_{nr}} \quad (3)$$

The lifetime of the radiative phenomena can be measured with two different methods. One is based on continuous, sinusoidally modulated excitation and the other method is based on a discrete, short excitation pulse (see Figure 3). The former one, phase fluorometry, offer specific advantages in regards of usability and usage in terms of ambient light, while latter method (pulse fluorometry) can't be used under ambient light. While the decay time is easily accessible with pulse fluorometry, the phase fluorometry only offers specific values: the phase shift and the demodulation. But the lifetime can be calculated following equation 4

$$\tau = \frac{tan\,\varphi}{2 \cdot \pi \cdot f} \quad (4)$$

where φ is the measured phase shift and f the modulation frequency of excitation.

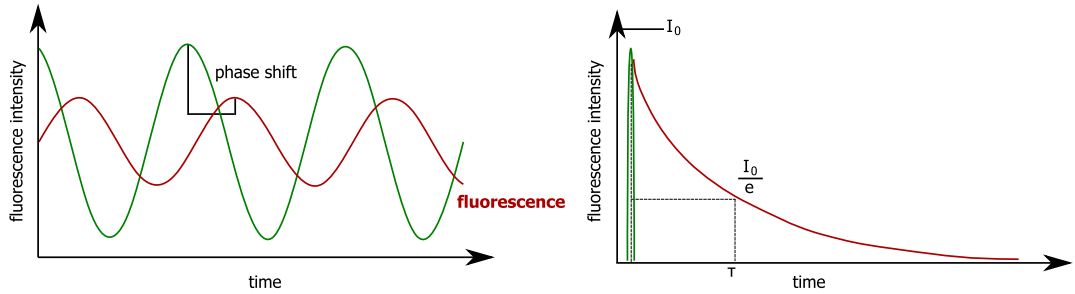

Figure 3: Measurement methods to determine luminescence lifetime: Phase fluorometry (left) and pulse fluorometry (right).

Optical Sensors

What is a sensor?

Although the word sensor, sensoric or sensing is used and misused widely in academic and industrial branches, there is no absolute definition of an sensor. IUPAC defines a chemical sensor as following:

> A chemical sensor is a device that transforms chemical information, ranging from the concentration of a specific sample component to total composition analysis, into an analytically useful signal. The chemical information, mentioned above, may originate from a chemical reaction of the analyte or from a physical property of the system investigated.[4]

Wolfbeis, Cammann, Hall et al. postulated in the *Cambridge Definition of Chemical Sensors*[5], that a chemical sensor can be defined as a "miniaturized analytical device that can deliver real-time and on-line information in the presence of specific compounds or ions in complex samples"[6]. So in general, a sensor is a small measurement device for a specific application or analyte. A sensor is not the compound that reacts to the presence of an analyte, which is merely a probe. Most sensors should fulfill following conditions[7]:

- Conversion of chemical information into measureable signals
- Fast response to the change of the analyte's concentration
- Long period of use
- Small or able to be miniaturized
- Low priced
- Specific towards a single analyte or selective towards a group of analytes
- High sensitivity towards the analyte

Sensors normally consist of a *receptor* and a *transductor*. The receptor reacts to the presence of the analyte or with the analyte itself and changes one or more distinctive properties or characteristics. Depending on the reversibility of this reaction, the sensor might need constant supply of receptor. In case of an irreversible reaction and a finite amount of receptor the sensor is called a dosimeter.

Furthermore the receptor can be used to differentiate types of sensors. Chemosensors employ synthetic compounds as receptors while biosensors employ biomolecules[8]. This distinction can be vague, in case of synthetically modified bio-molecules. The transducer converts the property of the receptor to a measureable signal. The existence of a transducer is imperative unless the changing property or characteristic of the receptor is measureable[7].

Classifications of sensors

Very often sensors are categorized by their transducer or the type of signal in which the chemical information is transformed[4].

- **Optical sensors**: Sensors, which derive the concentration of an analyte from the change of an optical phenomenon. This includes absorption, change of wavelength, polarization, scattering, resonance, time shifted response and more. This thesis deals exclusively with the development of optical sensors.
- **Electrochemical sensors** convert the analytical information based on an electrochemical interaction of the analyte with an electrode. This includes all kinds of voltammetric measurement principles, chemically sensitized field effect transistors and more.
- **Electrical sensors** also provide a measurable electrical signal, but the formation of this signal is not based on electrochemical interaction. Typically measured properties are permittivity and conductivity.
- **Mass sensitive sensors** supply a signal based on a change of mass, mostly by the formation of a bond with an analyte compound.
- **Magnetic sensors**, represented by devices which react towards specific diamagnetic or paramagnetic properties of an analyte and the change of these properties.
- **Thermometric sensors** sense the presence of an analyte based on heat effects, which can occur from reactions of adsorption phenomena.
- **Sensors based on other properties** employ other properties such as nuclear radiation.

A straight forwards approach to classify sensors is based on the analyte. This can be done easily, even with sub classifications (e.g. oxygen sensors, ammonia sensors and carbon dioxide sensors as examples of gas sensors).

Optical sensors

As stated in the previous chapter, the mean of measuring a concentration is light in case of optical sensors. Optical sensors normally consist of a light source, optical elements to filter or prepare the light before the interaction with a transducer, the object or sensor itself, further optical elements which filter the altered light and a detector to quantify the signal or a property of the signal. Not all parts are mandatory for every device, in specific applications some parts can be disclaimed such as light source (thermo- or bioluminescence sensing) or filters. Also, it is possible to integrate specific compartments of the read-out unit into the sensor, such as photo detectors, filters or other parts. Optical

sensors have distinctive advantages over electrical and electrochemical sensors. In comparison to electrochemical sensors no reference electrode is necessary, which eases the process of miniaturization. Also, no wires are specifically necessary to transmit a signal of a planar optical sensor. This also enables the use of imaging techniques. Furthermore, optical signals are not prone to interference by magnetic of electrical fields.

Many different types of optical sensors have been developed in the recent decades, and their shape, appearance and application is manifold. They can reach from nanoparticles for tissue and cellular imaging[9] and miniaturized fiber optical sensors[10] to multianalyte array sensors[11] or planar waveguide sensors[12]. Current reviews give a comprehensive overview over the vast number of different optical sensors[13,14,15,16,17,18]. In this thesis only sensors employing luminescence or absorbance are discussed.

Due to loss of transducer molecules, incoherent characteristics of the sensor layer or read-out device parts, or changing ambient conditions it is sometimes necessary to reference the measured quantity of a property of light. Light intensity measurements are very prone to errors if they are not shielded from ambient light. This can either be realized by an darkened measurement cell or by the use of a sinusoidally modified excitation and a lock-in amplifier to distinguish between the emission which stems from the modified excitation and the emission which stems from the constant ambient light. Still, other factors such as leaching, bleaching, aggregation, background luminescence, scattering, changing alignment have an effect on detected emission intensity. Two solutions are popular among scientists: The ratiometric two wavelength referencing (TWR) approach and the dual lifetime referencing (DLR) approach.

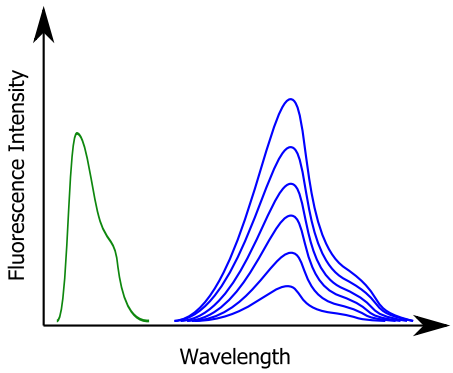

Figure 4: Scheme of a ratiometric measurement of an two wavelength ratiometric reference optical sensor (green: reference, blue: receptor/transducer)

A second dye or compound is introduced into the sensor for TWR referencing. This second compound must not be sensitive towards the analyte and shows a similar characteristic as the transducer (e.g. absorbance, luminescence). In every measurement step the signal of the transducer/receptor is measured as well as the signal of the reference. Since the signal quantity of the reference is constant, changes from e.g. deviating alignments can be compensated. It has to be noted, that changes in the receptor-transducer pair (loss due to aggregation, leaching or bleaching) is not compensated by the TWR unless the reference shows the same characteristics in these processes as the transducer/receptor does.

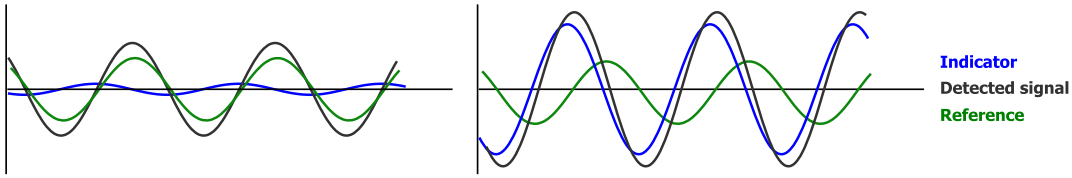

Figure 5: Scheme of a dual lifetime referencing process.

DLR is a referencing method which is primarily used for short lifetime fluorophores. Similar to TWR, a second dye is introduced into the sensor for DLR. This compound also must not be sensitive towards the analyte. Additionally, the reference dye shows a long decay time and is excited by the same modulated light source as the indicator dye. A super positioned modulated emission signal is measured, which changes its phase shift from the exciation's phase by the amount of indicator fluorescence emission. Also similar to TWR, changes in amount of indicator cannot be compensated by an DLR measurement.

---

[1] J. R. Lakowicz, *Principles of Fluorescence Spectroscopy*, Springer, New York, **2006**.

[2] B. Valeur, *Molecular Fluorescence: An Introduction. Principles and Applications*, Wiley-VCH, **2002**.

[3] D. Wöhrle, M. W. Tausch, W.-D. Stohrer, *Photochemie*, John Wiley & Sons, **2012**.

[4] A. Hulanicki, S. Glab, F. Ingman, *Pure and Applied Chemistry* **1991**, *63*, 1247–1250.

[5] K. Camman, G. Guilbault, E. Hall, R. Kellner, M.-L. Schmidt, and O. S. Wolfbeis, *"Cambridge Definition" of Chemical Sensors* **1996**.

[6] R. Narayanaswamy, O. S. Wolfbeis, *Optical Sensors: Industrial, Environmental and Diagnostic Applications*, Springer, **2004**.

[7] P. Gründler, *Chemische Sensoren: Eine Einführung für Naturwissenschaftler und Ingenieure*, Springer DE, **2004**.

[8] F. S. Ligler, *Optical Biosensors: Present and Future*, Gulf Professional Publishing, **2002**.

[9] J. Kneipp, H. Kneipp, B. Wittig, K. Kneipp, *Nanomedicine: Nanotechnology, Biology and Medicine* **2010**, *6*, 214–226.

[10] O. S. Wolfbeis, *Anal. Chem.* **2008**, *80*, 4269–4283.

[11] F. Ligler, C. Taitt, in *Fluorescence Sensors and Biosensors*, CRC Press, **2005**, pp. 263–281.

[12] D. Christensen, S. Tolley, H.-K. Wang, A. Terry, J. Herron, S. Brown, L. Tan, E. Simon, M. Astill, J. Durtschi, et al., in *Fluorescence Sensors and Biosensors*, CRC Press, **2005**, pp. 283–332.

[13] B. Kuswandi, Nuriman, J. Huskens, W. Verboom, *Analytica Chimica Acta* **2007**, *601*, 141–155.

[14] P. C. A. Jerónimo, A. N. Araújo, M. Conceição B.S.M. Montenegro, *Talanta* **2007**, *72*, 13–27.

[15] J. Homola, *Chemical Reviews* **2008**, *108*, 462–493.

[16] C. McDonagh, C. S. Burke, B. D. MacCraith, *Chemical Reviews* **2008**, *108*, 400–422.

[17] N. S. Oliver, C. Toumazou, A. E. G. Cass, D. G. Johnston, *Diabetic Medicine* **2009**, *26*, 197–210.

[18] J. Kneipp, H. Kneipp, B. Wittig, K. Kneipp, *Nanomedicine: Nanotechnology, Biology and Medicine* **2010**, *6*, 214–226.

Design and optimization of Förster resonance energy transfer cascades

Introduction

The Förster resonance energy transfer[1] or FRET is a well-known phenomenon. It has been used in applications of different fields, especially in chemical and biochemical sensing applications[2,3,4,5,6,7,8,9]. It offers the possibility to extend spectral ranges or differences between excitation and emission wavelength of a luminescent system ("Stoke's shift") by combining two or more known compounds.

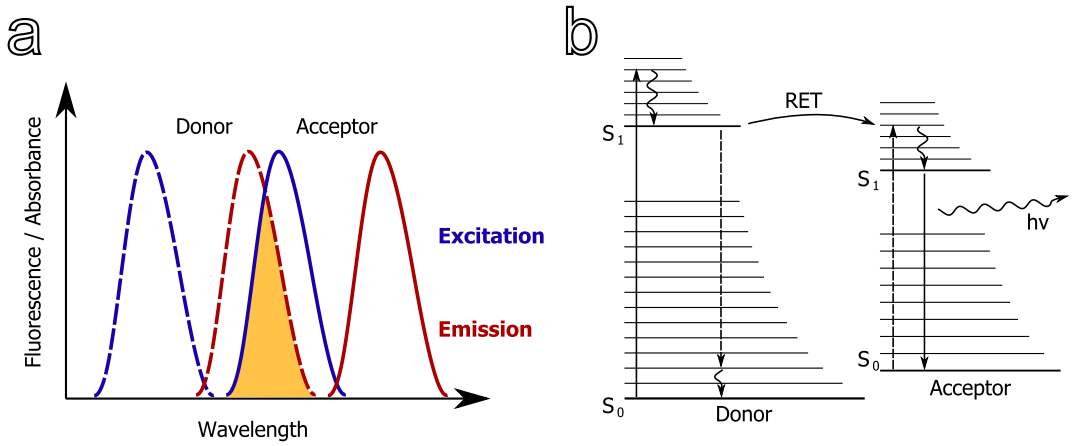

Figure 6: Schematic view of the spectral overlap of a molecule pair for a FRET transfer, shown in a spectrum (a) or a Jablonski diagram (b).

The FRET is a mass-free and radiation-free exchange of energy by resonance vibration. In each transfer two partners are involved: a donor and an acceptor. These two molecules feature a specific, spectral characteristic; to wit the donor's emission spectra and the acceptor's excitation spectra overlap partially or even completely (see Figure 6). The percentage of spectral overlap is one key factor which determines the ratio of transferred excitation energy to emitted excitation energy (in case of a luminescent donor molecule)

Another key factor determining the transfer efficiency is proximity. While there are transfer interactions of molecules due to orbital overlap including electron transfer (Dexter's mechanism), the FRET normally occurs between two molecules with a distance of about 0.1 to 10 nanometers between each other. A specific constant, R_0 or the *Förster radius*, expresses a distance between two particular compounds, at which the probability for a transfer is 0.5 or 50%, i.e. the probability of an occurring transfer is the same as the probability for an excitation relaxation of the donor. Förster derived equation 5[10] to describe the rate constant of emission for the transfer rate based on long-range dipole-dipole interactions.

$$k_T^{dd} = k_D \cdot \left(\frac{R_0}{r}\right)^6 = \frac{1}{\tau_D^0} \cdot \left(\frac{R_0}{r}\right)^6 \quad (5)$$

where k_D is the donor's emission rate constant, τ_D^0 is its lifetime in absence of the donor, r is the distance between donor and acceptor, and R_0 is the previously mentioned Förster radius. It should be noted, that the transfer rate is inversely proportional dependent on the sixth power of the radius, thus making it very sensitive to small distances and changes of that.

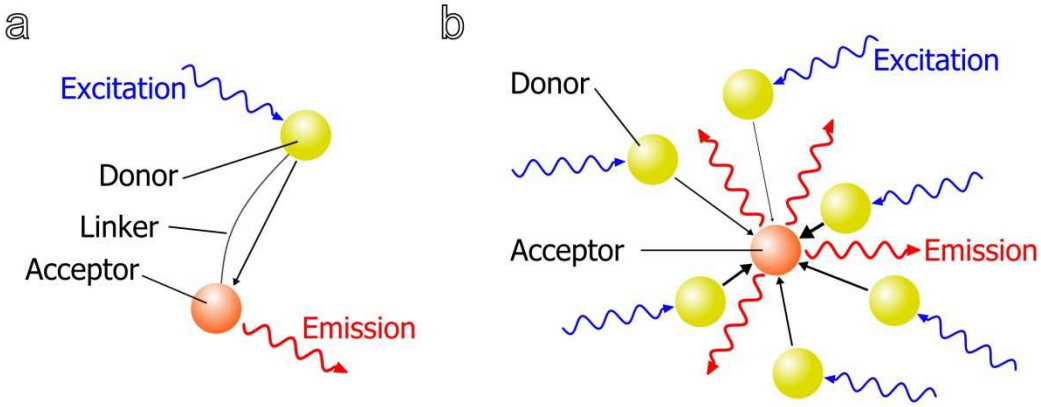

Figure 7: Two different approaches to realize FRET: A tailored (a) approach containing two luminophores linked covalently together or a stochastic (b) with randomly distributed luminophores in a matrix.

There are two different possibilities to optimize the transfer rate between two molecules (see Figure 7). The first approach is a “tailored” approach, in which the donor and the acceptor are covalently linked together. This approach is extensively used in the concept of molecular beacons[11]. Basically said, both molecules are linked together by a spacer or a chain which holds both molecules in the correct distance to gain maximized transfer efficiency. The other method could be described as “stochastic”. In this approach donor and acceptor molecules are randomly distributed in a bulk material (e.g. solution or polymer). The probability of having a pair of donor and acceptor in a distance facilitating the FRET increases with higher amounts of these molecules.

Two different FRET cascades have been designed. Both cascades have different purposes: cascade A is used as an internal lamp whereas cascade B is used for ratiometric imaging techniques. Both cascades are used for specific applications and have therefore specific characteristics. The process of designing and optimizing these cascades is described within this chapter.

Experimental

Materials

Tetrahydrofuran (THF) and polystyrene (MW. 250000) (PS) were obtained from Acros Organics (Geel, Belgium). Hydrogel D7 was obtained from CardioTech International Inc. (Wilmington, MA, United States). 10-(2-benzothiazolyl)-2,3,6,7-tetrahydro-1,1,7,7-tetramethyl-1H,5H,11H-[l]benzopyrano[6,7,8,ij]quinolizin-11-one (Coumarin 545T or C545T) and 3-(2-N-Methylbenzimidazolyl)-7-N,N-diethylaminocoumarin (Coumarin 30 or C30) were purchased from purchased from Sigma Aldrich Chemie GmbH (Steinheim, Germany). Macrolex Fluorescent Red G (MFR) was purchased from Simon & Werner GmbH (Flörsheim am Main, Germany). Lumirror boPET foil with a thickness of 125 nm was purchased from Pütz GmbH + Co. Folien KG (Taunusstein, Germany).

Cocktails and foil preparation

The foils were prepared by dissolving polymers, donor and acceptor in THF (5% (w/w) of solids in 95% (w/w) of solvent). The gained cocktails were spread onto a boPET foil using a drawdown bar film applicator (wet film thickness 25.4 µm) purchased from BYK-Gardner GmbH (Geretsried, Germany). After the evaporation of the solvent the foils were dried in a drying oven for at least one hour at 60°C.

Instrumentation

Absorbance spectra were recorded with a Varian Cary 50 spectrophotometer. Luminescence spectra were recorded using a Hitachi F-7000 fluorescence spectrophotometer.

Results and Discussion

There are different characteristics one has to consider during the design and optimization of such a system. Facing a specific problem, the choice of the donor is often pre-determined by its excitation wavelength and the choice of the acceptor is pre-determined by it emission wavelength. The used concentration of donor or acceptor molecules is limited by factors such as aggregation, solubility or the inner filter effect. Furthermore, both compounds have to be chemically stable in its used matrix.

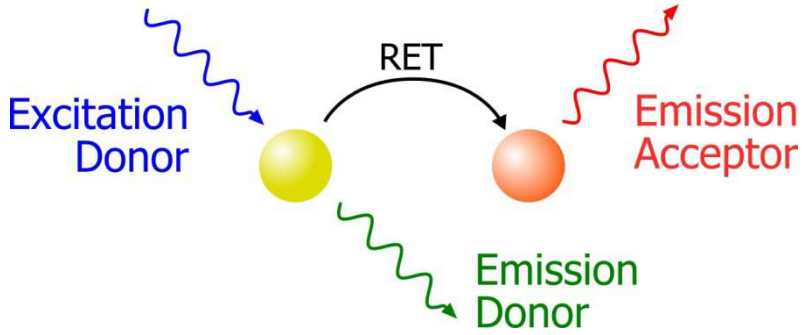

Figure 8: Spectral characteristics of a FRET cascade based on luminescent molecules.

As mentioned in the introduction, two different cascades have been designed: Cascade A and Cascade B. Cascade A was applied in two different projects: It was used in the ISOTEC project as a simple yet effective coupling system for an integrated waveguide sensor. In the Ammonia Sensor project it was used to employ absorbance based pH indicators for fluorescent based ammonia sensing. Both usages had the same requirements: high brightness, large Stoke's shift, an emission focused at 600 nm, and minimized donor fluorescence. Cascade B was only used in the Ammonia Sensor project, where it replaced Cascade A for fluorescence imaging purposes. Its requirements were similar to Cascade A with one exception: Unlike the prior cascade, Cascade B had to show an increased peak of the donor's emission, which had to be easily distinguishable from the acceptor's emission.

Cascade A

Cascade A consisted of two different molecules: Coumarin 545T (C545T) and Macrolex Fluorescent Red G (MFR). This combination covers all requirements: the

absorbance at 450 (excitation wavelength for the ISOTEC project) and 470 nm (excitation wavelength of pH-mini for the ammonia sensor), as well as the orange emission at 600 nm. Figure 9 shows absorbance and fluorescence emission spectra of both compounds.

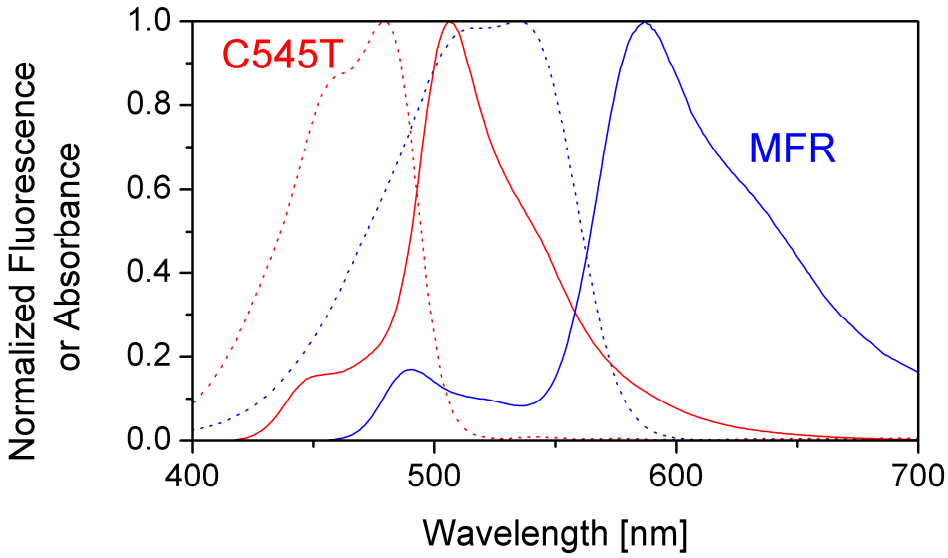

Figure 9: Absorbance (dotted line) and fluorescence emission (solid line) spectra of C545T (red) and MFR (blue).

The first step in creating and optimizing this cascade was to characterize the dependency of the acceptor's concentration on the spectrum and the emission intensity (see Figure 10).

It is easily observable, that the emission intensity of the cascade is highest at an acceptor concentration of 0.1% (w/w). The emission intensity decreases with increasing acceptor content, most likely due to an inner filter effect and self-quenching. On the other hand, the shape of the emission spectra at 0.1% (w/w) acceptor concentration is distinctly different to the shape at higher concentrations, namely the increased emission at 500 to 550 nm. This difference points to a considerable amount of donor's emission, which also decreases with increasing acceptor content (see also Figure 11).

Though it is not apparent in Figure 10, Figure 12 shows the dependency of the peak wavelength towards the acceptor's concentration. The peak wavelength is shifted from 580 to 598 nm at acceptor concentrations at 0.1 and 1% (w/w). This relationship can be

seen in Figure 13 together with the dependency of sensor brightness. This correlation shows no local minimum or maximum at the tested concentration range, which means a compromise of emission wavelength and intensity has to be made depending of the specific application.

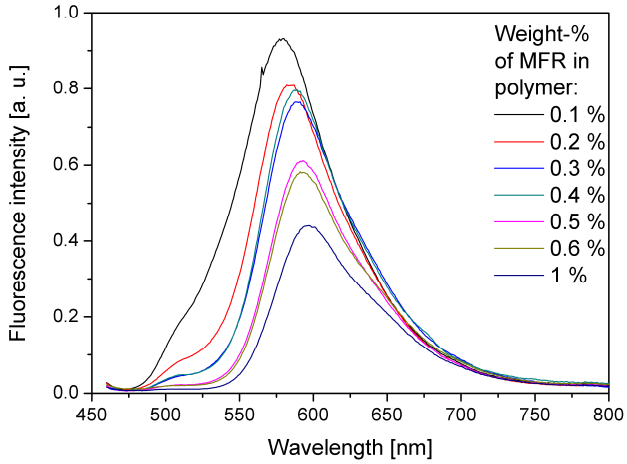

Figure 10: Emission spectra of polymer foils containing fluorescence cascade A with varying concentration of acceptor molecules (C545T: 2% (w/w)).

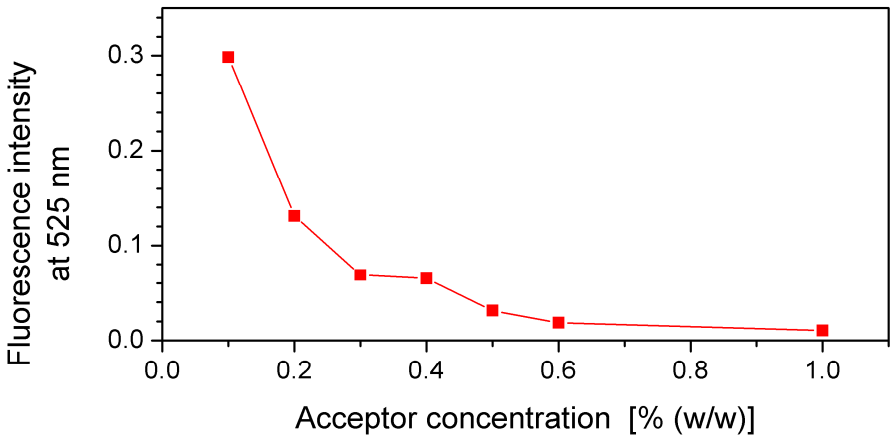

Figure 11: Fluorescence intensity at the donor emission wavelength normalized to acceptor emission maximum.

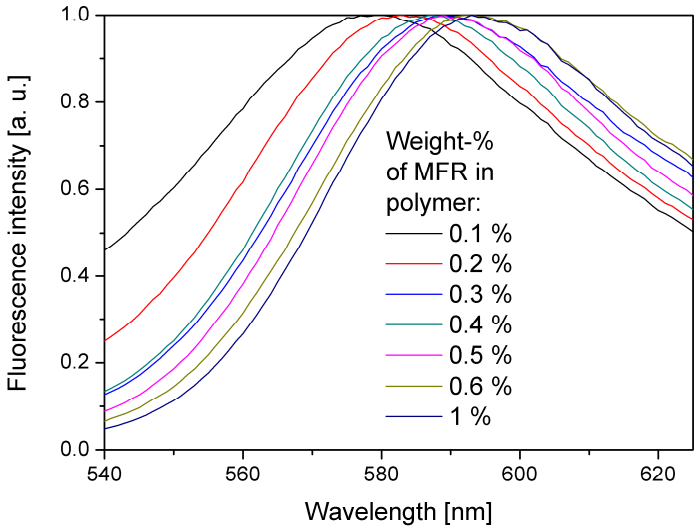

Figure 12: Normalized emission peak of polymer foils containing fluorescence cascade A with varying concentration of acceptor (MFR) (C545T: 2% (w/w)).

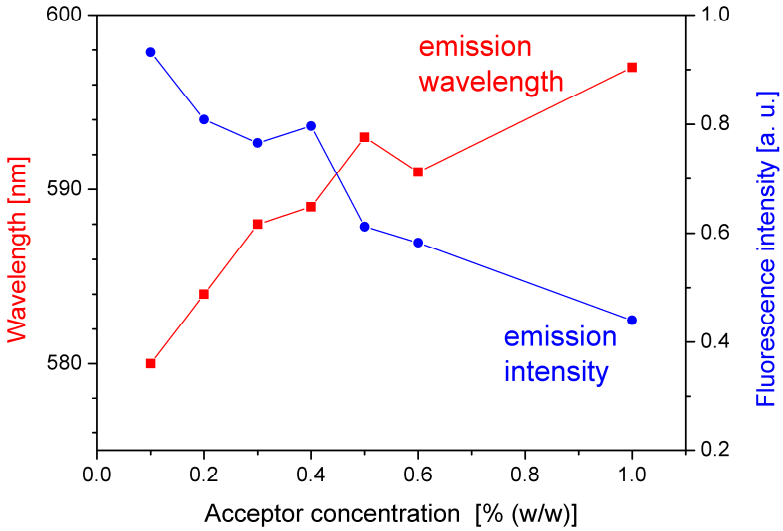

Figure 13: Emission wavelength and intensity of the fluorescence cascade in dependency of varying acceptor concentrations.

The second test, concluding the optimization of cascade A, was an assessment of the consequences of varying the donor's concentration, specifically towards the cascade's fluorescence intensity or spectrum. From the recorded fluorescence spectra (see Figure 14) it can easily be concluded, that there is no dependency towards the donor's concentration in this range. A higher donor concentration is still desirable in some applications, where the donor might be prone to bleaching, so that the higher concentration provides a reservoir of donor molecules.

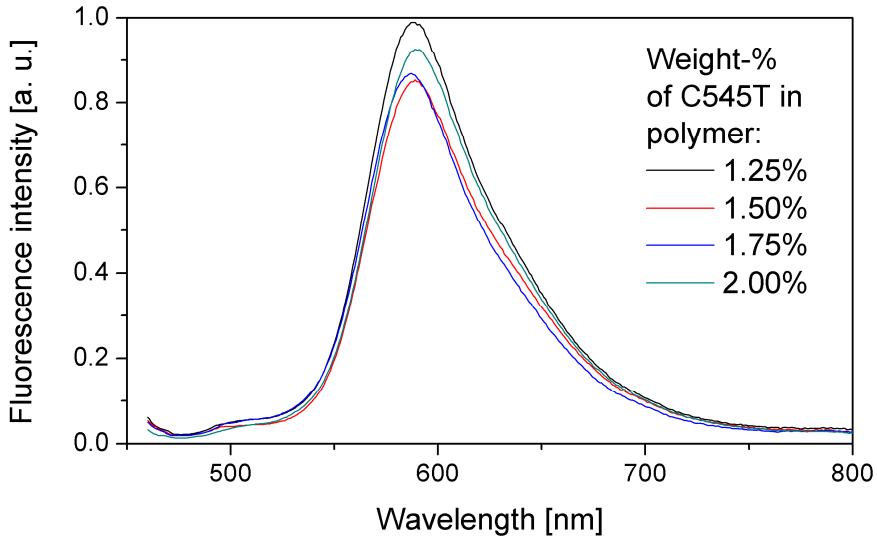

Figure 14: Emission spectra of polymer foils containing fluorescence cascade A with varying concentration of donor molecules (MFR: 0.3% (w/w)).

Cascade B

Cascade B is similar to cascade A. The changed application (ratiometric chemical imaging) led to different requirements of the cascade. For ratiometric measurements two signals have to be detected, which are referenced to each other (ratio). By decreasing the transfer rate of the FRET, the donor‘s emission increases and the acceptor's emission decreases, thus creating two different and distinct emission peaks. The cascade can then be combined with absorbance-based indicators, which introduce a sensitive element and change the emission profile in accordance to the absence or presence of an analyte.

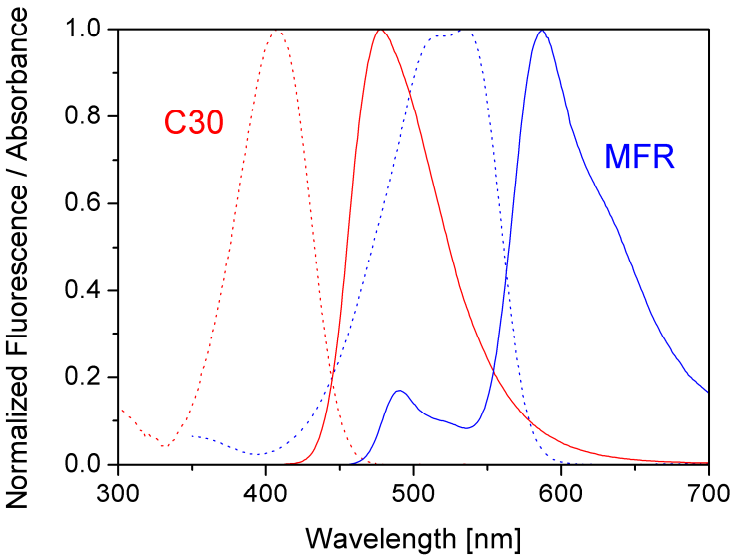

Figure 15: Absorbance (dotted line) and fluorescence emission (solid line) spectra of C30 (red) and MFR (blue).

To achieve this, the donor dye had to be changed. Instead of Coumarin 545T, Coumarin 30 (C30) was employed. C30 features a shorter wavelength of the absorbance peak and a shorter emission wavelength (see Figure 15). Due to the shorter wavelength, the spectral overlap is not as high as for the pair C545T-MFR.

Figure 16 shows the emission spectra of 4 different polymer foils containing the combination of C30 and MFR with varying concentrations of MFR: It is clearly observable, that at increasing acceptor concentration the emission peak at 600 nm increases, while the peak at 485 nm decreases. The ratio can be seen in Figure 17, where the emission spectra are normalized to the intensity value of the donor's emission peak. At an acceptor concentration of 0.3%, the emission intensity of the donor is about 4-fold higher than of the acceptor. This ratio decreases with the acceptor concentration and the acceptor emission (at 0.1%) is lower than the emission of the donor. This marks this system as an easily tunable fluorescent lamp, which can be used for ratiometric imaging.

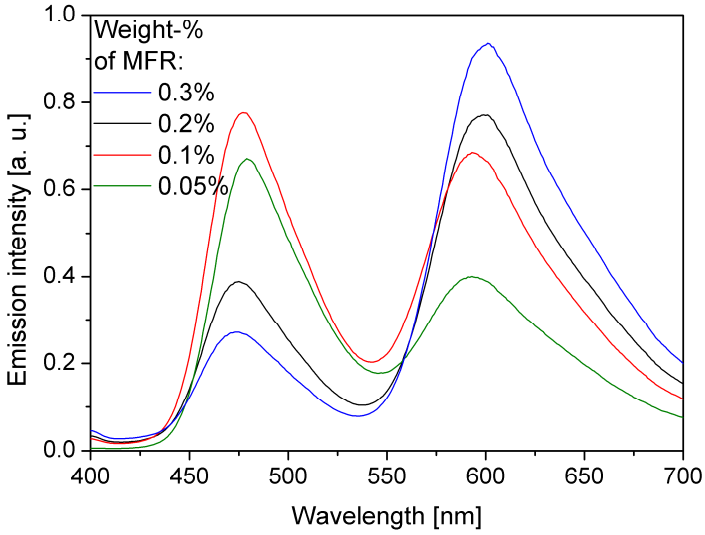

Figure 16: Emission spectra of polymer foils containing fluorescence cascade B with varying concentration of acceptor (C30: 2% (w/w)).

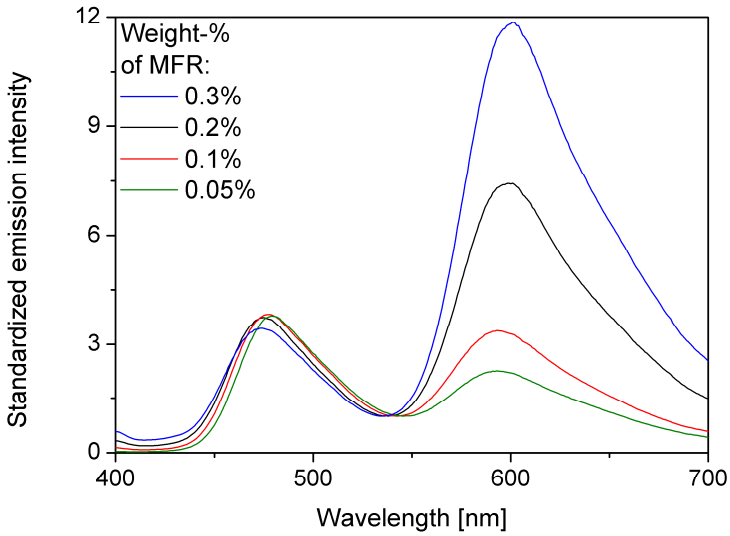

Figure 17: Emission spectra of polymer foils containing fluorescence cascade B with varying concentration of acceptor (MFR), normalized at the donor's emission peak (485 nm). (C30: 2% (w/w))

Conclusion

Two different cascades were designed and evaluated. Both cascades consisted of bright fluorophores, which resulted in bright luminescent systems with a high stokes shift. The cascades have proven themselves to be a reliable and easily tunable system. It is possible to tune the transfer rate by control of the concentration of the cascade's components. The concept of fluorescence cascades in chemo- and biosensors have been used during the entire thesis.

---

[1] T. Förster, *Annalen der Physik* **1948**, *437*, 55–75.

[2] G. Blagoi, N. Rosenzweig, Z. Rosenzweig, in *Fluorescence Sensors and Biosensors*, Taylor & Francis, Boca Raton, **2005**.

[3] H. Ma, E. A. Gibson, P. J. Dittmer, R. Jimenez, A. E. Palmer, *Journal of the American Chemical Society* **2012**, *134*, 2488–2491.

[4] G. Ryu, J. Huang, O. Hofmann, C. A. Walshe, J. Y. Y. Sze, G. D. McClean, A. Mosley, S. J. Rattle, J. C. deMello, A. J. deMello, et al., *Lab on a Chip* **2011**, *11*, 1664–1670.

[5] K. Waich, S. Borisov, T. Mayr, I. Klimant, *Sensors and Actuators B: Chemical* **2009**, *139*, 132–138.

[6] E. A. Jares-Erijman, T. M. Jovin, *Nature Biotechnology* **2003**, *21*, 1387–1395.

[7] J. Wilhelm, A. Pingoud, *ChemBioChem* **2003**, *4*, 1120–1128.

[8] I. L. Medintz, A. R. Clapp, H. Mattoussi, E. R. Goldman, B. Fisher, J. M. Mauro, *Nature Materials* **2003**, *2*, 630–638.

[9] A. Miyawaki, J. Llopis, R. Heim, J. M. McCaffery, J. A. Adams, M. Ikura, R. Y. Tsien, *Nature* **1997**, *388*, 882–887.

[10] B. Valeur, *Molecular Fluorescence: An Introduction. Principles and Applications*, Wiley-VCH, **2002**.

[11] S. Tyagi, S. A. E. Marras, F. R. Kramer, *Nature Biotechnology* **2000**, *18*, 1191–1196.

Development of an carbon dioxide sensor layer for the use with the ISOTEC waveguide platform

Introduction

There are many different approaches for the optical measurement of carbon dioxide. Several solutions and mechanisms have been employed, such as surface plasmon resonance[1], chemically functionalized field-effect transistors[2], potentiometry[3], conductive organic polymers[4] or impedance[5]. Recently Zosel et al. published a review[6] about current techniques and methods to measure and monitor carbon dioxide. One of the most common types of optical CO_2 sensors is a modified pH sensor with a buffer system for bicarbonate and carbonate[7,8,9,10,11]. Mills and Eaton published a review[12] back in 2000 about optical sensors for carbon dioxide, focusing on the pH sensing approach. Chu et al. published a review[13] about recent developments in luminescence based sensing of oxygen and carbon dioxide.

Sensing mechanism

Basically speaking, the pH based carbon dioxide sensing approach is a pH sensor, in which the pH value is determined by the carbon dioxide concentration of the analyte medium. A carbon dioxide permeable material separates the analyte medium from a buffer system. The buffer system changes its pH value due to the uptake of CO_2 and the conversion to carbonic acid, which then forms the acid-base equilibrium with its conjugated base. The change of pH is measured and quantified by an absorptive or fluorescent pH indicator (in case of optical sensors) or a pH electrode (in case of electrochemical sensors).

$$[\mathrm{B^+Ind^-} \cdot \mathrm{nH_2O}] + \mathrm{CO_{2(g)}} \rightleftharpoons \left[\mathrm{B^+Ind^-} \cdot \mathrm{nH_2O} \cdot \mathrm{CO_{2(aq)}}\right] \quad (6)$$

$$\left[\mathrm{B^+Ind^-} \cdot \mathrm{nH_2O} \cdot \mathrm{CO_{2(aq)}}\right] \rightleftharpoons \left[\mathrm{B^+Ind^-} \cdot (\mathrm{n}-1)\mathrm{H_2O} \cdot \mathrm{H_2CO_{3(aq)}}\right] \quad (7)$$

$$\left[\mathrm{B^+Ind^-} \cdot (\mathrm{n}-1)\mathrm{H_2O} \cdot \mathrm{H_2CO_{3(aq)}}\right] \rightleftharpoons [\mathrm{B^+HCO_3} \cdot \mathrm{HInd} \cdot (\mathrm{n}-1)\mathrm{H_2O}] \quad (8)$$

In case of optical sensing systems, a basic compound is used as a counterion for the indicator. It keeps the indicator in its deprotonated form in the absence of carbon dioxide and also serves as a stabilizer, if lipophilic or nonpolar buffer matrices (e.g. polymers) are used. The equations 6 to 8[14] describe the three main processes, which occur during the sensor response towards carbon dioxide. They also show explicitly, that the sensor's response is linked to the presence of humidity. Without any humidity the formation of carbonic acid (see equation 7) could not take place. Furthermore, an excess content of base is desirable, since it can buffer other acidic gases (e.g. SO_2, NO_x), which prolongs the sensor's shelf life.

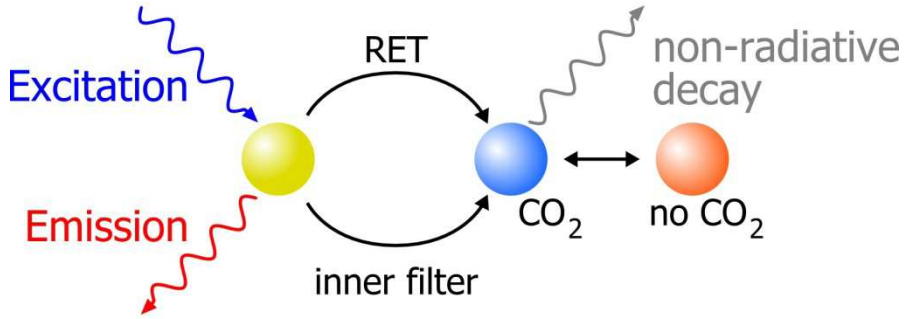

Figure 18: Functional scheme of the sensing mechanism employing a luminescent compound (yellow sphere) and an absorptive indicator dye (blue and red sphere). The luminescent compound emits light unless in presence of CO_2 the indicator dye is protonated and the excitation energy is transferred to it by either inner-filter effect or Förster resonance energy transfer (FRET).

Many different indicators have been used, both absorptive (such as meta-cresol purple[15], cresol red[16] and bromothymol blue[17]) as well as fluorescent (such as HPTS[18]). Fluorescent indicators offer the ease in instrumentation of measuring fluorescence. There is a broader variety in commercially available absorptive indicators, but the measurement of absorbance is not as easy as the measurement of fluorescence. This issue can be avoided by the combination of a non-sensitive luminescent compound with an absorptive indicator dye in the sensor's matrix or buffer. The luminescent compound acts as a "lamp" and shows luminescence, which can be decreased by the indicator. The lowering of emission can happen by either a FRET if the luminescent compound is close enough to the absorptive indicator dye, or by re-absorption of emitted luminescence. This offers certain autonomy in terms of spatial sensor design.

Some requirements have to be fulfilled, so that a sensor can be manufactured based on this concept: The emission spectrum of the luminescent compound has to overlap the indicator's absorbance spectrum. Furthermore the luminescent compound has to be soluble in the sensor matrix and also chemically stable towards the basic compound which stabilizes the indicator. Other characteristics, such as a high absorption coefficient, a high quantum yield and a large Stoke's shift are desirable.

Instrumental constraints

The ISOTEC platform with its integrated waveguide offers on one hand some degrees of freedom, but also constraints in other terms. The most important prerequisite is given by the integrated organic photodetector (OPD). Its spectrum of external quantum efficiency limits the wavelength range of detected emission to 550 to 750 nm.

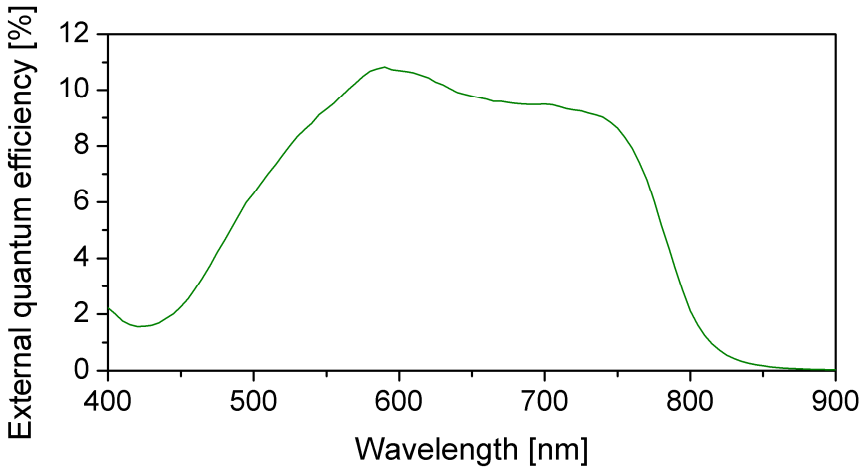

Figure 19: External quantum efficiency of the integrated organic photodetector.

Another key factor is the excitation wavelength. Although an interchangeable LED block for excitation was included in later versions of the read-out unit, the initial specification of the excitation wavelength was 450 or 470 nm.

Finally, the geometry of the integrated sensor platforms (see Figure 20) adds another stipulation towards the sensing chemistry. While in case of the absorbance based sensor platform the luminescent compound is spatially separated from the indicator (the former is in the incoupling spot, the latter in the waveguide layer), both compounds share the same

matrix in case of the luminescence based platform. This means, that the luminescent compound has to be chemically stable towards the indicator stabilizing lipophilic base.

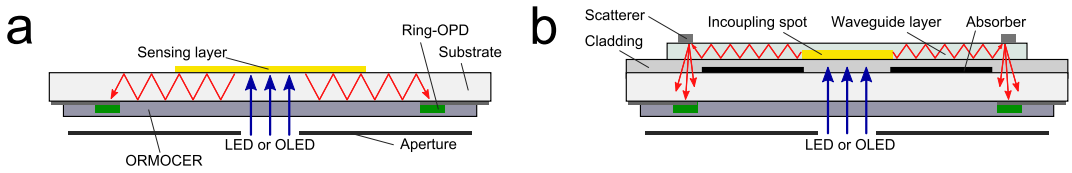

Figure 20: Geometry of the luminescence based (a) and absorbance based (b) integrated sensor platforms.

Subsequently, the sensor cocktails had to be processed by screen printing. This means, that a suitable viscosity of the sensor cocktails had to be fulfilled at concentration values which are necessary to print layers of desired thicknesses.

Experimental

Materials

Ethyl cellulose (48% ethyloxy content) (EC) was purchased from Scientific Polymers Inc. (Ontario, NY, United States). Tetra-N-octylammonium hydroxide (TOA^+OH) (20% solution in methanol) and m-Cresol Purple (mCP), were purchased from Sigma Aldrich Chemie GmbH (Steinheim, Germany). Ethanol and toluene was bought from Carl Roth GmbH (Karlruhe, Germany). $Ir(C_s)_2(acac)$ was synthesized in-house. Nitrogen was purchased from AIR LIQUIDE AUSTRIA GmbH (Graz, Austria). 5% carbon dioxide in nitrogen and 1% oxygen in nitrogen gas mixtures were purchased from LINDE GAS GmbH (Stadl-Paura, Austria).

Formation of the indicator ion pair

An ion pair of the indicator m-cresol purple and m-Cresol purple tetra-N-octylammoinum (mCP-TOA) was prepared in analogy as reported before[14]. A solution of 500 ml TOA^+OH (20% in methanol) was added to a solution of 51 mg mCP in 50 ml water. 50 ml toluene was added, the solution was vigorously shaken, the organic phase was collected with a separating funnel and washed three times with toluene, and the obtained

organic phase was dried with sodium sulfate and evaporated. The gained blue, oily substance was recollected in 4 ml of toluene/ethanol 8+2.

Sensor cocktails and layers

The sensor layers were manufactured in two steps. The first step was dissolving of indicator ion pair, luminescent compound, lipophilic base and polymer in a mixture of toluene and ethanol (8+2). In the second step the cocktail was spread with a drawdown bar film applicator (wet film thickness 25.4 µm) purchased from BYK-Gardner GmbH (Geretsried, Germany) onto a boPET foil. After the evaporation of the solvent the foils were dried in a drying oven at 60°C for about an hour. The manufactured sensing layers were stored in a desiccator over a 1 molar solution of sodium hydroxide for the absorption of acidic gases.

Instrumentation

Absorbance spectra were recorded with a Varian Cary 50 spectrophotometer. Luminescence spectra were recorded using a Hitachi F-7000 fluorescence spectrophotometer. Sensor responses were recorded using a SR830 lock-in amplifier (Stanford Research Systems, Inc., Sunnyvale, CA, United States) a home-made flow-through cell and a home-made optobox. This box consisted of a 450 nm LED (Roithner Lasertechnik, Vienna, Austria) combined with an Schott BG12 bandpass filter from (Edmund Optics GmbH, Karlsruhe, Germany), a H5701-02 photomultiplier tube (Hamamatsu, www.sales.hamamat-su.com) combined with an Carl Zeiss 575-625 nm band pass filter (Edmund Optics GmbH, Karlsruhe, Germany) and a bifurcated fiber bundle. Gas mixtures were provided using a gas blender consisting of mass flow controllers from MKS Instruments Deutschland GmbH (Munich, Germany).

Results and discussion

Choice of materials

Meta-cresol purple (mCP) was chosen as indicator, since it is commercially available, has a high absorption coefficient and shows suitable spectral and chemical properties[19]. In absence of carbon dioxide the protonated form of mCP is present, which does not decrease the luminophore's emission at about 600 nm. In presence of carbon dioxide the protonated state is formed and the luminescence is decreased. Tetraoctylammonium was used as stabilizing dye, as it has been reported before[14].

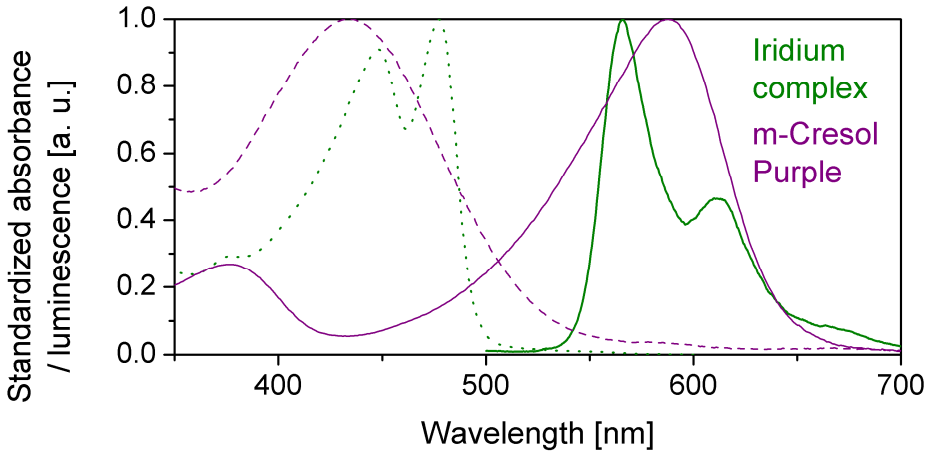

Figure 21: Absorbance spectra of deprotonated (solid purple graph) and protonated (dashed purple graph) forms of meta-Cresol Purple and absorbance (dashed green graph) and emission (solid green graph) spectra of $Ir(C_s)_2(acac)$.

Different luminescent materials have been tested, but most dyes failed to fulfill the chemical stability criterion towards tetraoctylammonium. This list covers Macrolex Fluorescent Red G, Macrolex Fluorescent Yellow 10 GN, Lumogen Yellow, Lumogen Orange, Lumogen Red, Coumarin 545T and Nile Red. A specific Iridium based metal-complex, called $Ir(C_s)_2(acac)$[20] showed chemical stability. The spectral properties of both compounds are depicted in Figure 21. Furthermore, the complex excels in terms of molar absorbance (92 800 M^{-1} cm^{-1}), quantum yield (0.54) and Stoke's shift (~90 nm). It has to be noted, that this complex is designed as a oxygen probe and therefore shows a cross-sensitivity towards oxygen. Also, since the Iridium complex displays long

phosphorescence decay times, it is possible not only to measure luminescence intensities as analytical signal, but also decay times. Latter is limited to the fluorescence based platform, because the decay time is only affected by the energy transfer and not by an inner-filter effect.

Ethyl cellulose has been chosen as host polymer, since it has been reported numerous times as a reliable material[12]. Ethyl cellulose polymers with different ethyloxy contents, ranging from 46.5% to 51% have been tested, displaying a slight increase of sensitivity with higher ethyloxy content. The used ethyl cellulose holds an ethyloxy content of 48%. The choice was determined by its extraordinary low viscosity (4 cP or 0.4 Pa·s in a 5% solution in 80+20 toluene/ethanol at 25°C), which allows concentrated sensor cocktails (up to 25% (w/w) in 80+20 toluene/ethanol). This offers the possibility to form high layer thicknesses with screen printing.

Evaluation of the sensor layer's composition

Different test were carried out to determine the optimal composition of the sensor components. The concentration of indicator (meta-cresol purple) was investigated in terms of maximized signal (measured intensity and phase shift) and in terms of maximized signal difference between the absence and presence of oxygen.

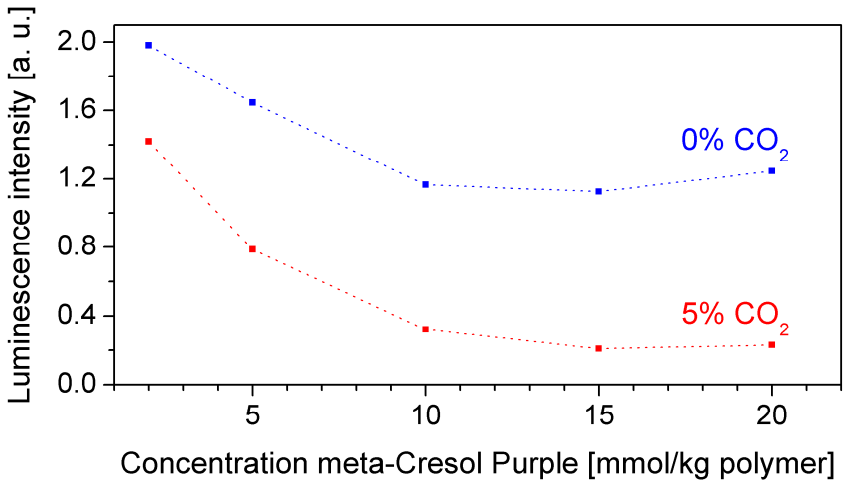

Figure 22: Luminescence intensities of sensor foils with different indicator contents at 0% and 5% CO_2 ($Ir(C_s)_2(acac)$: 1% (w/w), TOA^+OH^-: 200 mmol/kg polymer).

A dependency of maximum sensor brightness towards indicator content (see Figure 22) was identified. This can be related to the slight absorbance at about 600 nm of the deprotonated form of meta-cresol purple in absence of carbon dioxide. This dependency is only relevant in a concentration range of 2.5 to 10 mmol indicator per kilogram polymer; at higher contents it becomes negligible. On the other hand, the luminescence intensity carbon dioxide concentration of 5% (v/v) shows the same trend as the 0% carbon dioxide concentration graph towards indicator content, but in a stronger characteristic. This means, that in case of sufficient sensor brightness, an optimum ratio of brightness between 0% and 5% carbon dioxide is reached at an indicator content of 10 to 20 mmol/kg polymer.

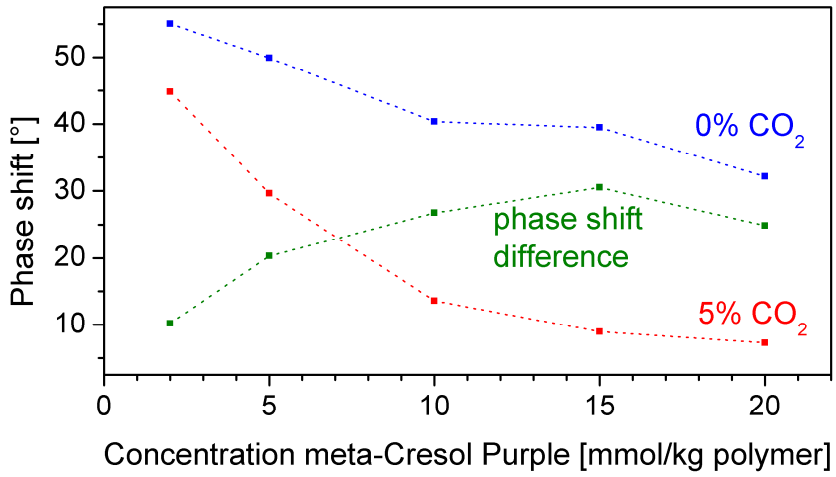

Figure 23: Phase shift and difference in phase shift of sensor foils with different indicator contents at 0% and 5% CO_2 ($Ir(C_s)_2(acac)$: 1% (w/w), TOA^+OH^-: 200 mmol/kg polymer).

A similar characteristic can be found in terms of dependency of phase shifts towards varying indicator dye content. Again, phase shift values are lesser with higher indicator concentrations, but the trend is even more pronounced at 5% (v/v) CO_2 and lesser at 0% CO_2. Again, the maximum in the difference of phase shifts are situated at indicator concentrations of 10 to 20 mmol/kg polymer.

Almost no dependency of the phase shift and its difference between the absence and presence of carbon dioxide towards TOA^+OH^-, the stabilizing lipophilic base, could be detected (see Figure 24). Although a slight increase can be noticed, a higher content of TOA is desirable due to the prolonged shelf life of the sensor.

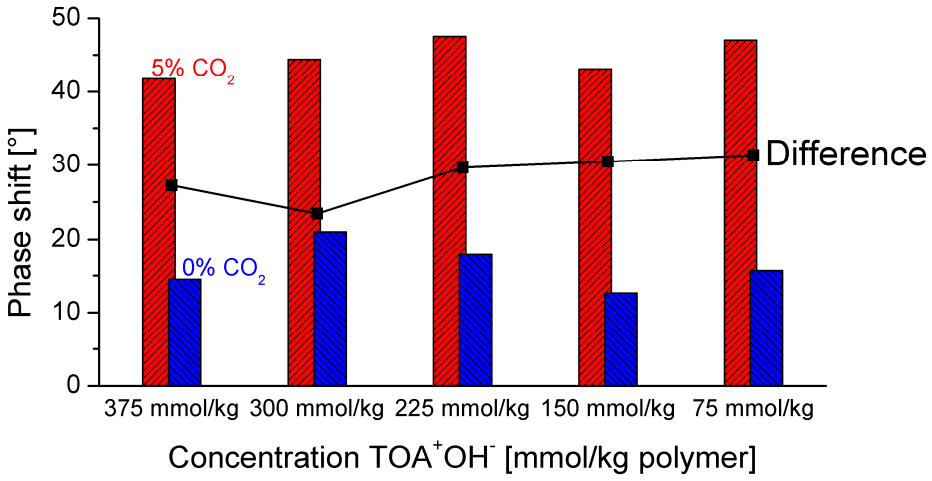

Figure 24: Dependency of the phase shift (blue and red bars) and difference of phase shift (black graph) at carbon dioxide concentrations of 0% and 5% towards the content of the lipophilic base ($Ir(C_s)_2(acac)$: 1% (w/w), TOA^+mCP^-: 15 mmol/kg polymer).

Sensor response

The optimized sensor layer consists of 1% (w/w) $Ir(C_s)_2(acac)$ as luminescent compound, 15 mmol TOA^+mCP per kilogram polymer as indicator ion pair and 300 mmol TOA^+OH^- per kilogram polymer as excess base for stabilization and prolonged shelf life. The sensor response of this mixture can be seen in Figure 26. The sensor layer displays a cross-sensitivity towards oxygen (between 20 and 40 minutes within a cycle in the graph) and an ideal response concentration of 0.25 to 2 % of carbon dioxide. The average response time t_{90} and t_{99} was determined to 5.5±1.5 and 11 minutes respectively. A drift of the sensor's calibration could be observed, which is shown in Figure 25. This can be attributed to photobleaching of the complex, which would lead to decreasing phase shifts and intensities.

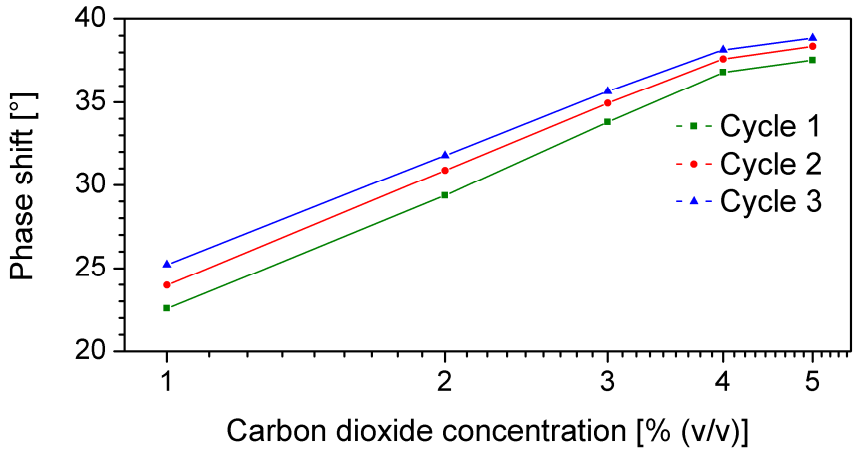

Figure 25: Calibration graphs of the sensor's response curves of each cycle (see Figure 26).

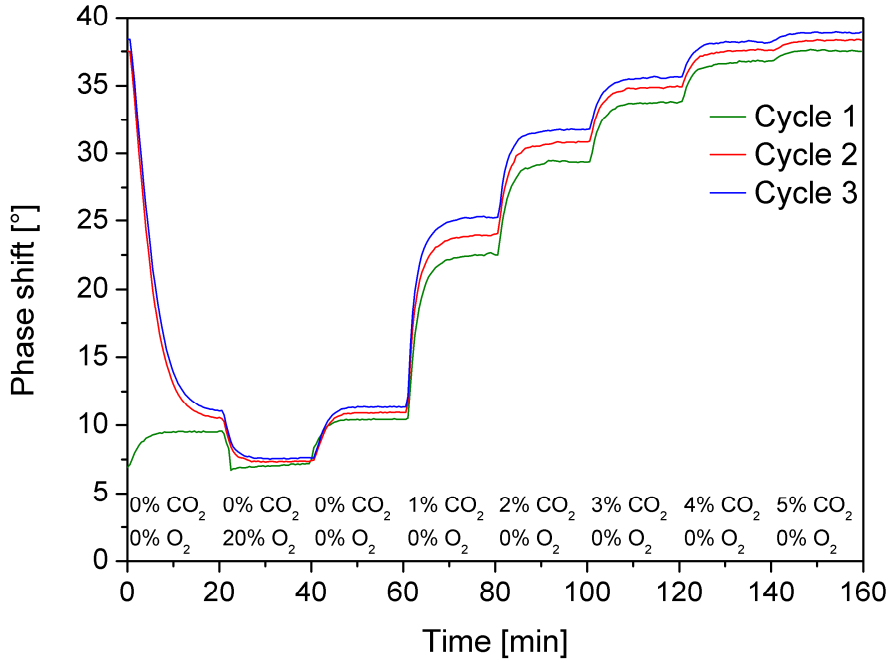

Figure 26: Response of a carbon dioxide sensor layer in 3 subsequent cycles. [($Ir(C_5)_2(acac)$: 1% (w/w), TOA^+mCP^-: 15 mmol/kg polymer, TOA^+OH^-: 300 mmol/kg polymer)

Adaptation to ISOTEC read-out unit

Since the sensing layer should have been employed with the ISOTEC integrated sensor platform, it was necessary to check if a sufficiently high difference in phase shifts could be measured with lower modulation frequency. This was required because the capacity of the OPDs and their influence on phase-modulated measurements at this state of the project were not known. Figure 27 shows the difference of the phase shift values at CO_2 concentrations of 5% and 0% in dependency of the modulation frequency. It was determined that a modulation frequency of 5 kHz or higher would have guaranteed a sufficiently high difference.

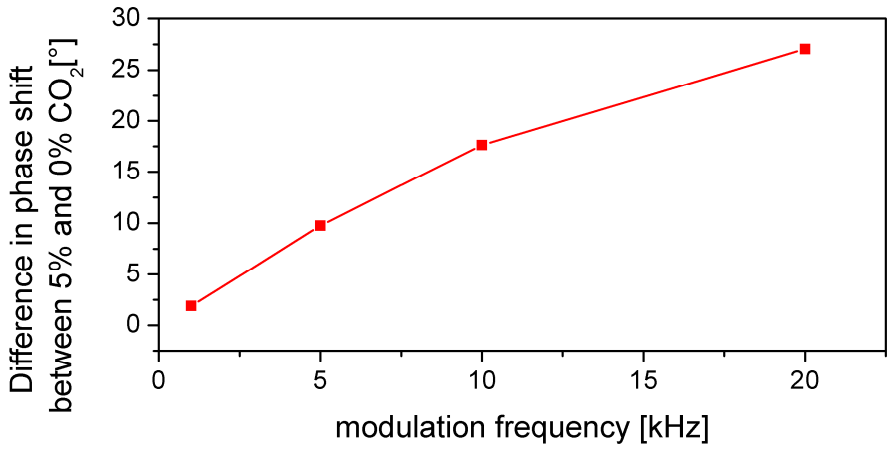

Figure 27: Difference of phase shift values at 5% and 0% CO_2 at different modulation frequencies.

Conclusion

A carbon dioxide sensitive sensing layer for the use with the ISOTEC integrated sensor platform was developed. The content of each compound was optimized for an ideal combination of brightness and signal change. A host polymer suitable for optimal screen printing results was chosen. The response time and calibration of the sensor layer was characterized. Cross-sensitivities towards oxygen were expected to be compensated mathematically by oxygen monitoring within the sensor platform.

It was only possible to optimize the layer for the luminescence based sensor platform (see Figure 20a), since the geometrical characteristics of the absorbance based sensor platform (see Figure 20b) could not be simulated. But, due to the fact that the components are separated in latter platform design, it was not necessary to examine potential dependencies of concentrations. Also, the separation of the compounds forecloses the employment of a phase-modulated lifetime measurement.

Unfortunately, the read-out electronics turned out to be based on a different measurement method. Due to the higher number of measurement points needed for a lifetime determination with this different measurement method, problems with photobleaching would have been imminent. Eventually a carbon dioxide sensitive layer based on HPTS was chosen which did not exhibit photobleaching.

---

[1] J. Homola, S. S. Yee, G. Gauglitz, *Sensors and Actuators B: Chemical* **1999**, *54*, 3–15.

[2] A. Star, T.-R. Han, V. Joshi, J.-C. P. Gabriel, G. Grüner, *Advanced Materials* **2004**, *16*, 2049–2052.

[3] T. Maruyama, S. Sasaki, Y. Saito, *Solid State Ionics* **1987**, *23*, 107–112.

[4] S. A. Waghuley, S. M. Yenorkar, S. S. Yawale, S. P. Yawale, *Sensors and Actuators B: Chemical* **2008**, *128*, 366–373.

[5] J. Herrán, G. G. Mandayo, E. Castaño, *Sensors and Actuators B: Chemical* **2008**, *129*, 705–709.

[6] J. Zosel, W. Oelßner, M. Decker, G. Gerlach, U. Guth, *Measurement Science and Technology* **2011**, *22*, 072001.

[7] J. W. Severinghaus, A. F. Bradley, *Journal of Applied Physiology* **1958**, *13*, 515–520.

[8] D. W. Lubbers, N. Opitz, *Zeitschrift fur Naturforschung. Section C: Biosciences* **1975**, *30*, 532–533.

[9] Z. Zhujun, W. R. Seitz, *Analytica Chimica Acta* **1984**, *160*, 305–309.

[10] O. S. Wolfbeis, L. J. Weis, M. J. P. Leiner, W. E. Ziegler, *Analytical Chemistry* **1988**, *60*, 2028–2030.

[11] A. Mills, Q. Chang, N. McMurray, *Anal. Chem.* **1992**, *64*, 1383–1389.

[12] A. Mills, K. Eaton, *Quimica Analitica* **2000**, *19*, 75–86.

[13] C.-S. Chu, Y.-L. Lo, T.-W. Sung, *Photonic Sensors* **2011**, *1*, 234–250.

[14] C. R. Schröder, I. Klimant, *Sensors and Actuators B: Chemical* **2005**, *107*, 572–579.

[15] T. Mayr, T. Abel, B. Enko, S. Borisov, C. Konrad, S. Köstler, B. Lamprecht, S. Sax, E. J. W. List, I. Klimant, *Analyst* **2010**, *134*, 1544–1547.

[16] B. H. Weigl, O. S. Wolfbeis, *Analytica Chimica Acta* **1995**, *302*, 249–254.

[17] R. Ali, S. M. Saleh, R. J. Meier, H. A. Azab, I. I. Abdelgawad, O. S. Wolfbeis, *Sensors and Actuators B: Chemical* **2010**, *150*, 126–131.

[18] O. S. Wolfbeis, B. Kovács, K. Goswami, S. M. Klainer, *Microchimica Acta* **1998**, *129*, 181–188.

[19] J. Sipior, S. Bambot, M. Romauld, G. M. Carter, J. R. Lakowicz, G. Rao, *Analytical Biochemistry* **1995**, *227*, 309–318.

[20] S. M. Borisov, I. Klimant, *Anal. Chem.* **2007**, *79*, 7501–7509.

Organic optoelectronics in integrated sensors

> "In 20 years from now, will we have the Star Trek Tricorder that tells us at a distance the identity of a target of interest, be it chemical, biological, or mineral?"[1]

As, of course, there can't be a definitive answer to this question, it illustrates the desire of scientists, developers and users towards future sensor functionality. The concept of integrated sensors is an expression as well as a solution to this wish. "Normal" or basic chemo- and biosensors consist of a receptor (and sometimes a transducer) which is controlled and read out by external instrumentation. Integrated sensors contain further components, inheriting functions which are otherwise executed by the external instrumentation[2]. These functions can extend from redundant copies of the same sensor for extended reliability, to the integration of electronic or signal processing components.

Kohl et al. list following benefits of integrated sensors[3]:

- The integration of single- or multi-stage signal preparation combined with methods to increase accuracy and precision.
- The combination of multiple or different sensors to compensate perturbation or cross sensitivities mathematically.
- The connectivity to host systems for an external access of sensor data and for the adaptation of measurement or sensor parameters.
- The linking of spatially distributed and separated sensors by suitable means of wire-based and also wireless technologies.

A variety of advantages is responsible for the progress the field of integrated sensors[4]; techniques such as soft lithography, hot embossing or vapor deposition played a very important part in this matter[5]. Especially miniaturized total chemical analysis systems[6] (µTAS) have benefitted greatly from these improvements. µTAS integrate several process steps up to the functionality of a typical laboratory into one platform[7,8] which allows ideally usage by untrained personnel. These are auspicious systems for point-of-care diagnostics[9] or public health application in the developing world[10].

An obvious necessity for integrated optical sensors is the integration of optoelectronic components. Although miniaturization and integration of existing technology is demanded, it is also important to invent strategies to render previously necessary components unnecessary and to develop new materials, which overcome preexisting technical restrictions[11]. The miniaturization of some technologies is simply unfeasible.

Xenon arc lamps, which can be found in conventional fluorescence spectrometers, haven't been scaled down to the size of a credit card yet, and will probably never be. In contrast, semiconductor based elements, such as light emitting diodes[12] (LEDs), complementary metal–oxide–semiconductors[13,14] (CMOS) and charge-coupled devices[15,16] (CCDs) have successfully been employed in miniaturized systems. However, they are too expensive for disposable systems[17]. Organic optoelectronics, to wit organic light emitting diodes (OLED) and organic photodetectors (OPD), have been a very promising answer to the question of miniaturization and integration[18].

A typical OLED is composed of organic layers, embedded sandwich-like between two electrodes. Conductive layers of electronic compartments consist generally of metal, which is mostly not transparent to the visible light. This can be circumvented by using transparent metal oxide layers, such as indium tin oxide (ITO, In_2O_3, used in most OLEDs or OPDs) or organic substances, which are conductive due to delocalized π-electrons. Between the generally transparent anode and the cathode, which is optionally transparent, lie three active layers: an electron transport layer (ETL), an emitting layer (EL), and a hole transport layer (HTL). The active layers are typically fabricated by thermal vacuum deposition, but efforts have been made to employ other techniques such as spin-coating or inkjet printing. During an OLED's operation, h^+ (holes) and e^- (electrons) are injected from the anode or cathode respectively and wander towards each other. After the formation an exciton upon their recombination in the EL, the exciton undergoes relaxation and produces radiation. The wavelength of the radiation is determined by the energy difference between the HOMO and the LUMO of the material, the so-called "band gap". Of course, this is a basic schematic principle of an OLED's structure and operation, the reality knows single-layer, stacked, top-emitting, hybrid and other types of OLEDs[18].

OPDs and OLEDs are similar in terms of structure and principle. Again, one or more organic layers are enclosed between two electrodes, of which at least one is transparent[19]. This simplistic example is naturally exceeded by the complexity of current photo detectors, which can hold multiple organic layers, PEDOT:PSS[20] (poly[3,4-(ethylenedioxy)-thiophene]:poly(styrene sulfonate) electrodes and fullerenes[21]. Their working principle is basically the OLED's working principle in reverse: The absorption of a photon in the organic layers forms an excited electron-hole pair, an exciton. The exciton then undergoes charge separation to form separated electrons and holes, which subsequently travel to cathode (electrons) and anode (holes). Hereafter a current can be detected[22].

Both devices have been employed in optical sensors. Savvate'ev et al. reported an optical oxygen sensor based on phosphorescence lifetime quenching and employing an integrated OLED[23]. Choudhury et al. presented in 2004 an optical sensor for gaseous and

dissolved oxygen, which featured a structurally integrated OLED on a glass substrate[24]. Also, Shinar et al. reported a further development of prior oxygen sensor, resulting in a glucose biosensor based on glucose oxidase (GOX) with an integrated OLED as excitation source[25],[26]. Lately (2008), the platform was used for multianalyte sensing[27]. Ohmori et al. processed a polymeric OLED and a tailored OPD onto different polymeric films to form an integrated waveguide platform[28]. A green OLED was employed as integrated excitation source of a microfluidic device by Qiu et al.[29]. The deMello group reported several approaches and devices using organic photonics, such as a diagnostic microchip with a green OLED for microalbuminuria detection[30] and microfluidic chemoluminsecence assays with integrated OPDs for the detection of hydrogen peroxide[31,32] or cardiac markers[33] (myoglobin and CK-MB). An integrated fluorescence biosensor based on OLED and inorganic photo detectors was presented by Azam et al.[34]. Papautsky et al.,[35] and Kraker et al.[36] reported a simple yet universal filter setup employing both OLED and OPD in integrated sensing platforms. Bürgi et al. realized an absorption based bio-test with mouse immunoglobulin G on a waveguide platform employing an OLED and an OPD[37]. A competitive fluorescent bioassay with an OLED was created by Shin et al.[38]. Sax et al. employed an oxygen sensitive organic complex in an OLED's active layer to manufacture an oxygen-sensitive OLED[39].

Besides the need for further optimization to increase efficiency, precision and stability of OPDs and OLEDs[40,41] the sensor platform itself has to be designed purposefully to meet the demands of the used photonic compartments. This includes manufacturing and processing steps, spectral properties and electronic engineering of the read-out instrumentation. The following chapter deals with the design and evaluation of an integrated sensor platform employing OPDs.

---

[1] F. S. Ligler, *Anal. Chem.* **2009**, *81*, 519–526.

[2] P. V. Lambeck, *Measurement Science and Technology* **2006**, *17*, R93–R116.

[3] F. Kohl, P. Loschmidt, T. Sauter, *e & i Elektrotechnik und Informationstechnik* **2006**, *123*, 377–382.

[4] K. D. Wise, *Sensors and Actuators A: Physical* **2007**, *136*, 39–50.

[5] O. Brand, *Proceedings of the IEEE* **2006**, *94*, 1160 –1176.

[6] A. Manz, N. Graber, H. M. Widmer, *Sensors and Actuators B: Chemical* **1990**, *1*, 244–248.

[7] D. Erickson, D. Li, *Analytica Chimica Acta* **2004**, *507*, 11–26.

[8] J. El-Ali, P. K. Sorger, K. F. Jensen, *Nature* **2006**, *442*, 403–411.

[9] J. S. Erickson, F. S. Ligler, *Nature* **2008**, *456*, 178–179.

[10] P. Yager, T. Edwards, E. Fu, K. Helton, K. Nelson, M. R. Tam, B. H. Weigl, *Nature* **2006**, *442*, 412–418.

[11] K. D. Wise, K. Najafi, *Science* **1991**, *254*, 1335–1342.

[12] E. J. Cho, F. V. Bright, *Analytica Chimica Acta* **2002**, *470*, 101–110.

[13] M. L. Adams, M. Enzelberger, S. Quake, A. Scherer, *Sensors and Actuators A: Physical* **2003**, *104*, 25–31.

[14] J. M. Song, M. Culha, P. M. Kasili, G. D. Griffin, T. Vo-Dinh, *Biosensors and Bioelectronics* **2005**, *20*, 2203–2209.

[15] J. P. Golden, F. S. Ligler, *Biosensors and Bioelectronics* **2002**, *17*, 719–725.

[16] S. Moon, H. O. Keles, A. Ozcan, A. Khademhosseini, E. Hæggstrom, D. Kuritzkes, U. Demirci, *Biosensors and Bioelectronics* **2009**, *24*, 3208–3214.

[17] J. R. Wojciechowski, L. C. Shriver-Lake, M. Y. Yamaguchi, E. Füreder, R. Pieler, M. Schamesberger, C. Winder, H. J. Prall, M. Sonnleitner, F. S. Ligler, *Analytical Chemistry* **2009**, *81*, 3455–3461.

[18] J. Shinar, R. Shinar, *Journal of Physics D: Applied Physics* **2008**, *41*, 133001.

[19] H. Spanggaard, F. C. Krebs, *Solar Energy Materials and Solar Cells* **2004**, *83*, 125–146.

[20] S. Günes, H. Neugebauer, N. S. Sariciftci, *Chemical Reviews* **2007**, *107*, 1324–1338.

[21] B. C. Thompson, J. M. J. Fréchet, *Angewandte Chemie - International Edition* **2008**, *47*, 58–77.

[22] H. Hoppe, N. S. Sariciftci, *Journal of Materials Research* **2004**, *19*, 1924–1945.

[23] V. Savvate'ev, Z. Chen-Esterlit, J. W. Aylott, B. Choudhury, C.-H. Kim, L. Zou, J. H. Friedl, R. Shinar, J. Shinar, R. Kopelman, *Applied Physics Letters* **2002**, *81*, 4652–4654.

[24] R. Shinar, Z. Zhou, B. Choudhury, J. Shinar, *Analytica Chimica Acta* **2006**, *568*, 190–199.

[25] B. Choudhury, R. Shinar, J. Shinar, *J. Appl. Phys.* **2004**, *96*, 2949.

[26] R. Shinar, D. Ghosh, B. Choudhury, M. Noack, V. L. Dalal, J. Shinar, *Journal of Non-Crystalline Solids* **2006**, *352*, 1995–1998.

[27] Y. Cai, R. Shinar, Z. Zhou, J. Shinar, *Sensors and Actuators B: Chemical* **2008**, *134*, 727–735.

[28] Y. Ohmori, H. Kajii, M. Kaneko, K. Yoshino, M. Ozaki, A. Fujii, M. Hikita, H. Takenaka, T. Taneda, *Selected Topics in Quantum Electronics, IEEE Journal of* **2004**, *10*, 70 – 78.

[29] Y. Qiu, B. Yao, G. Luo, L. Wang, Y. Gao, G. Lei, K. Ren, L. Chen, Y. Wang, Y. Hu, *Lab on a Chip* **2005**, *5*, 1041—1047.

[30] O. Hofmann, X. Wang, J. C. deMello, D. D. C. Bradley, A. J. deMello, *Lab Chip* **2005**, *5*, 863–868.

[31] O. Hofmann, P. Miller, P. Sullivan, T. S. Jones, J. C. deMello, D. D. C. Bradley, A. J. deMello, *Sensors and Actuators B: Chemical* **2005**, *106*, 878—884.

[32] X. Wang, O. Hofmann, R. Das, E. M. Barrett, A. J. deMello, J. C. deMello, D. D. C. Bradley, *Lab on a Chip* **2007**, *7*, 58.

[33] G. Ryu, J. Huang, O. Hofmann, C. A. Walshe, J. Y. Y. Sze, G. D. McClean, A. Mosley, S. J. Rattle, J. C. deMello, A. J. deMello, et al., *Lab on a Chip* **2011**, *11*, 1664–1670.

[34] A. B. M. S. Azam, M. Boukadoum, R. Izquierdo, A. Acharya, M. Packirisamy, in *2008 Joint 6th International IEEE Northeast Workshop on Circuits and Systems and TAISA Conference, 2008. NEWCAS-TAISA 2008*, **2008**, pp. 173 –176.

[35] A. Pais, A. Banerjee, D. Klotzkin, I. Papautsky, *Lab Chip* **2008**, *8*, 794–800.

[36] E. Kraker, A. Haase, B. Lamprecht, G. Jakopic, C. Konrad, S. Köstler, *Applied Physics Letters* **2008**, *92*, 033302.

[37] M. Ramuz, L. Bürgi, C. Winnewisser, P. Seitz, *Organic Electronics* **2008**, *9*, 369–376.

[38] K.-S. Shin, Y.-H. Kim, K.-K. Paek, J.-H. Park, E.-G. Yang, T.-S. Kim, J.-Y. Kang, B.-K. Ju, *IEEE Electron Device Letters* **2006**, *27*, 746 –748.

[39] S. Sax, E. Fisslthaler, S. Kappaun, C. Konrad, K. Waich, T. Mayr, C. Slugovc, I. Klimant, E. J. W. List, *Advanced Materials* **2009**, *21*, 3483–3487.

[40] M. Granström, K. Petritsch, A. C. Arias, R. H. Friend, *Synthetic Metals* **1999**, *102*, 957–958.

[41] M. Jørgensen, K. Norrman, F. C. Krebs, *Solar Energy Materials and Solar Cells* **2008**, *92*, 686–714.

Filter-free integrated sensor array based on luminescence and absorbance measurements using ring-shaped organic photodiodes

Tobias Abel[1], Martin Sagmeister[2], Bernhard Lamprecht[2], Elke Kraker[2], Stefan Köstler[2], Birgit Ungerböck[1], and Torsten Mayr[1*],

[1] Institute of Analytical Chemistry and Food Chemistry, Graz University of Technology, Stremayrgasse 9, 8010 Graz, (Austria)

[2] JOANNEUM RESEARCH - Institute for Surface Technologies and Photonics, Franz-Pichler Straße 30, 8160 Weiz, Austria

*Corresponding author

Telephone: +43 (316) 873 – 32504

Fax: +43 (316) 873 - 1032504

E-Mail: torsten.mayr@tugraz.at

Published in: Analytical and Bioanalytical Chemistry© Springer-Verlag 2012

Received: 15 April 2012

Revised: 22 May 2012

Accepted: 30 May 2012

Published online: 17 June 2012 - 10.1007/s00216-012-6175-4

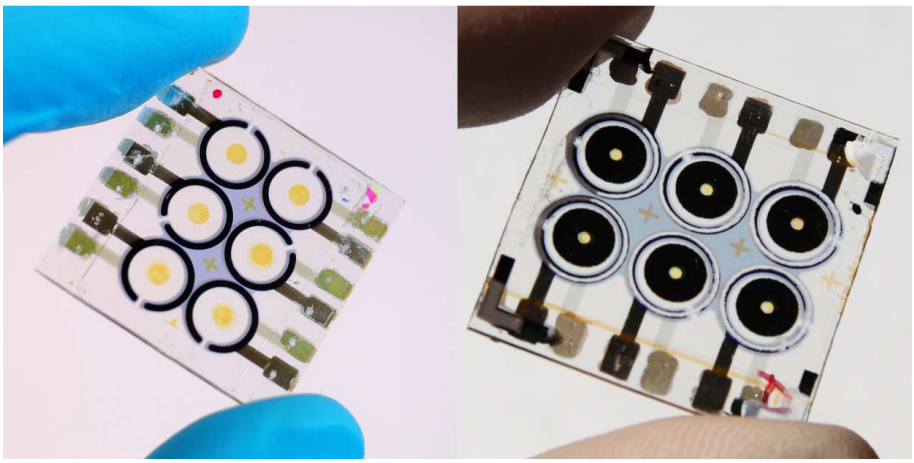

Online abstract figure

Abstract

An optical waveguiding sensor array featuring monolithically integrated organic photodiodes as integrated photo-detector, which simplifies the readout system by minimizing the required parts, is presented. The necessity of any optical filters becomes redundant due to the proposed platform geometry, which discriminates between excitation light and sensing signal. The sensor array is capable of measuring luminescence or absorption, and both sensing geometries are based on the identical substrate. It is demonstrated, that background light is virtually non-existent. All sensing and waveguide layers, as well as in- and out-coupling elements are assembled by conventional screen-printing techniques. Organic Photodiodes (OPD) are integrated by layer-by-layer vacuum deposition onto glass or common polymer foils. The universal and simple applicability of this sensor chip is demonstrated by sensing schemes for four different analytes. Relative humidity, oxygen, and carbon dioxide are measured in gas phase using luminescence based sensor schemes, the latter two analytes are also measured by absorbance based sensor schemes. Furthermore oxygen and pH in aqueous media were enabled. The consistency of calibration characteristics extending over different sensor chips is verified.

Keywords

Optical sensor, organic photodiode, sensor array, integrated sensor, optoelectronic, screen-printing

Introduction

Optical sensing of physical and chemical parameters has gained huge interest over the last decades and found many different applications such as diagnostics, marine and atmospheric research, clinical monitoring, and biotechnology [1,2]. It has proven to be a rugged, flexible, and universally applicable method, which stands out due to its ease of miniaturization, fabrication, and low-cost manufacturing potential. Therefore optical sensing is the favored sensing mechanism [3,4] in miniaturized analytical instruments (*Lab-on-a-Chip*[5]). An issue in recent years has emerged from functional integration of optical, optoelectronic, electronic, and sensing components[6,7] within monolithic substrates. This trend has been supported by progress in the field of organic electronics[8,9]. These elements based on organic semiconductors offer new possibilities in terms of integration due to their ease of processing by low-temperature vacuum layer-by-layer manufacturing, their potential to tune the spectral response[10], and the fact that they can be deposited on almost any kind of substrate[11]. Different approaches toward an integrated sensor platform have been described, using conventional detection systems and excitation by organic LEDs[12,13], or common inorganic light sources and organic photodiodes (OPD) for detection of luminescence[14,15,16]. For a state-of-the-art analysis of organic optoelectronics we refer to an excellent review, published by Shinar et al.[17].

In this paper we show an optical sensor chip for parallel detection of different analytes in a compact sensor array. We utilize ring-shaped OPDs as light detectors, which are integrated together with the analyte sensitive layers on the same substrate. The circular geometry of the sensor-setup maximizes the amount of in- and out-coupled light. We used manufacturing procedures that are simple and cost-effective such as spin-coating and screen-printing. Furthermore, it is possible to employ different sensing mechanisms for different media, based on luminescence and absorbance, maintaining the proposed geometry. This universal applicability is demonstrated by measuring relative humidity, oxygen, and carbon dioxide on a luminescence sensor chip and the latter two analytes based on an absorbance sensor chip in gaseous media. The adaptability for aqueous media is also shown by sensors for pH and dissolved oxygen in water.

Experimental

Organic photodiodes (OPDs)

The OPDs were manufactured by low temperature layer-by-layer deposition in vacuum chambers from Oerlikon Leybold Vacuum GmbH (Cologne, Germany). They consist of four active layers sandwiched by two electrodes, a 6 nm semitransparent gold electrode and a 150 nm silver topelectrode. The active layer is composed of four different materials (beginning from the gold electrode): a 5 nm layer of molybdenum oxide, a 25 nm layer of copper(II)phthalocyanine (CuPc), a 25 nm layer of 3,4,9,10-perylenetetracarboxylicbisbenzimidazole (PTCBi), a 30 nm layer of 4,7-diphenyl-1,10-penantroline (Bphen). The OPDs were encapsulated in ORMOCER®.

Materials

Anisole, polystyrene (MW. 250000) (PS), bromophenole blue (BPB) were obtained from Acros Organics (Geel, Belgium). Ethyl cellulose (48% ethyloxy content) (EC) was purchased from Scientific Polymers Inc. (Ontario, NY, United States). Hydrogel D7 was obtained from CardioTech International Inc. (Wilmington, MA, United States). Tetra-N-octylammoinum chloride (TOA^+Cl^-), tert-Octylimino-tris(dimethylamino)phosphorane (P_1-t-Oct), m-Cresol Purple (mCP), 10-(2-benzothiazolyl)-2,3,6,7-tetrahydro-1,1,7,7-tetramethyl-1H,5H,11H-[l]benzopyrano[6,7,8,ij]quinolizin-11-one (Coumarin 545T or C545T), 8-Hydroxypyrene-1,3,6-trisulfonic acid trisodium salt (HPTS-Na), Tetra-N-octylammonium hydroxide (TOA^+OH) (20% solution in methanol), Glucose oxidase (GOX) from Aspergillus niger were purchased from Sigma Aldrich Chemie GmbH (Steinheim, Germany). Ethanol, toluene, 1,4-dioxane, Dichloromethane ($CHCl_3$), alpha-D(+)-Glucose monohydrate, 2-(N-morpholino)ethanesulfonic acid (MES), N-Cyclohexyl-2-aminoethanesulfonic acid (CHES), sodium dihydrogen phosphate, disodium hydrogen phosphate, was bought from Carl Roth GmbH (Karlruhe, Germany) Hexadecyltrimethylammonium chloride (CTAC), 3-(N-morpholino)propanesulfonic acid (MOPS) and Ammonium chloride were purchased from Fluka Chemie GmbH (Buchs, Switzerland). Teflon AF 1600 was purchased from DuPont Fluoroproducts (Wilmington, DE, United States). Macrolex Fluorescent Yellow 10 GN (MFY) and Macrolex Fluorescent Red G (MFR) were purchased from Simon & Werner GmbH (Flörsheim am Main, Germany). Platinum(II) and palladium(II) 5,10,15,20-meso-tetrakis-(2,3,4,5,6-pentafluorphenyl)-porphyrin (PtTFPP and PdTFPP) were obtained by Frontier Scientific (www.frontiersci.com). Ir(Cs)2(acac) and $HPTS(DHA)_3$ were synthesized in-house. Nitrogen and carbon dioxide was purchased from AIR LIQUIDE

AUSTRIA GmbH (Graz, Austria). 5% carbon dioxide in nitrogen and 1% oxygen in nitrogen gas mixtures were purchased from LINDE GAS GmbH (Stadl-Paura, Austria).

Preparation of indicator ion-pairs

The three indicator ion-pairs HPTS tetraocytlammonium (HPTS-TOA), HPTS cetyltrimethylammonium (HPTS-CTA), and m-Cresol purple tetraocytlammonium (mCP-TOA) were prepared analogical as reported before[18,19].

For HPTS-TOA a solution of 1450 mg TOA^+Cl in 50 ml water was added dropwise to a solution of 500 mg HPTS-Na in 100 ml. 50 ml $CHCl_3$ was added, the solution was vigorously shaken, the organic phase was collected with a separating funnel, washed with $CHCl_3$ three times, and the obtained organic phase was dried with sodium sulfate and evaporated. The gained brown oily substance was recollected in 4 ml of $CHCl_3$.

For HPTS-CTA a solution of 155 mg CTAC in 50 ml toluene was added dropwise to a solution of 87.5 mg HPTS-Na in 50 ml water. The solution was vigorously shaken, the organic phase was collected with a separating funnel, washed with toluene three times, and the obtained organic phase was dried with sodium sulfate and evaporated. The gained brown oily substance was recollected in 4 ml of toluene/ethanol 8+2.

For mCP-TOA a solution of 500 ml TOA^+OH (20% in methanol) was added to a solution of 51 mg mCP in 50 ml water. 50 ml toluene was added, the solution was vigorously shaken, the organic phase was collected with a separating funnel and washed three times with toluene, and the obtained organic phase was dried with sodium sulfate and evaporated. The gained blue, oily substance was recollected in 4 ml of toluene/ethanol 8+2.

Layer preparation

The layers were prepared by dissolving polymers, indicators, and luminophores in an organic solvent in 4.5 ml vials. The gained “cocktails” were coated onto glass slides with drawdown bar film applicator (wet film thickness 25.4 µm) purchased from BYK-Gardner GmbH (Geretsried, Germany) or printed onto the integrated sensor chip using self-designed (see Electronic Supplementary Material 1) printing screens manufactured by Siebdruck Welle (Oberkirch, Germany).

Table 1: Composition of used sensing and waveguiding layers (Percentages of added components refer to polymer mass as 100%, mmol/kg of added components refers to kg polymer mass. Percentage in solution column refers to percentage of polymer and added components in the used solvent).

Layer	Polymer	Added components	Solution
A	PS	$Ir(C_s)_2(acac)$ 1%	Anisole 25% (w/w)
B	PS	MFY 2%	Anisole 25% (w/w)
		PtTFPP 1%	
C	PS	C545T 2%	Anisole 25% (w/w)
		PdTFPP 1%	
D	EC	HPTS-TOA 20 mmol/kg	Anisole/ethanol 8+2
		TOA^+OH 400 mmol/kg	25% (w/w)
E	EC	HPTS-CTA 40 mmol/kg	Anisole/ethanol 8+2
		P_1-t-Oct 400 mmol/kg	25% (w/w)
F	PS	C545T 2%	Anisole 25% (w/w)
		MFR 0.3%	
G	PS	-	Anisole 25% (w/w)
H	EC	mCP-TOA 1 mmol/kg	Anisole/ethanol 8+2
		TOA^+OH^- 200mmol/kg	25% (w/w)
I	D7	$HPTS(DEA)_3$ 2 mmol/kg	1,4-Dioxane 20%(w/w)

Instrumentation and measurement procedure

Absorbance spectra were recorded with a Varian Cary 50 spectrophotometer. Luminescence spectra were recorded using a Hitachi F-7000 fluorescence spectrophotometer. Measurements with the integrated sensor chip were carried out in a custom-made readout instrument consisting of excitation LED, OPD signal acquisition and amplification, mount for the integrated sensor and two flow-through cells for gas and liquid phase measurements made by mb-Technologies (Grosswilfersdorf, Austria). Gas mixtures were provided using a gas blender consisting of mass flow controllers from MKS Instruments Deutschland GmbH (Munich, Germany). An EK-H5 evaluation set with a SHT2x humidity sensor from Sensirion AG (Staefa, Switzerland) was used to determine humidity levels. pH measurements were carried out using a peristaltic pump from Gilson (Middleton, WI, United States) and 50 mM MES (pH 5.2, pH 6.2 and pH 6.7) MOPS (pH 7.3, pH 7.7 and pH 8.2) and CHES (pH 8.7, pH 9.2, pH 9.5) buffer solutions and 150 mM ion strength.

Results and discussion

Sensor geometry and setup

The functional principles of the sensor array with integrated organic photodiodes were reported earlier[20,21]. Figure 1a shows the geometry of the proposed luminescence based sensor chip. The substrate of such sensor could be a glass slide of common, transparent polymer foils. The OPDs are processed on the lower side of the substrate; an analyte sensitive layer is printed onto the upper side. The chip is then placed in a mount of the read-out unit, which contains inorganic LEDs (450 nm, purchased by Roithner Lasertechnik GmbH, Vienna, Austria) as excitation source, amplifier and microcontroller as well as a connection to a computer.

No optical filters are needed to differentiate between excitation and luminescence light. The geometry itself prefers the guiding of luminescent light directly to the detection unit. The LEDs illuminate exclusively the area of the sensing layer due to an aperture-like hole in the mount of the read-out unit beneath the chip. Luminescence is induced in the sensing layer and emitted isotropically. Because of the substrate's high refractive index a predominant part of the emitted light is coupled in and subsequently guided in the substrate. The light spreads radially till it is absorbed by the ring-shaped OPD, giving a rise in the photo current. Non-absorbed excitation light passes through the sensing layer and is subsequently absorbed in the matte black finish of the flow-through cell. A small part of the excitation light is coupled in due to scattering defects and polymer roughness, but this part was found to be insignificant.

Figure 1b depicts the design of the absorbance sensor chip. It consists of 5 different layers which are consecutively screen-printed and spin-coated, respectively, onto the identical substrate as mentioned in Figure 1a. The first layer is the absorber, composed of conventional black screen-printing paint. The second layer is the spin-coated cladding, consisting of Teflon AF, which was chosen due to its outstanding low refractive index (n = 1.33). It is followed by layer three, the screen-printed incoupling spot positioned right above the excitation source, which contains stable fluorophores with high quantum yields and suitable spectral properties. Layer four is the spin-coated waveguide layer, which consist of a polymer and an indicator dye depending on the targeted analyte. The fifth layer is the scatterer, based on commercially available white screen-printing ink, carefully aligned right above the ring-shaped OPD.

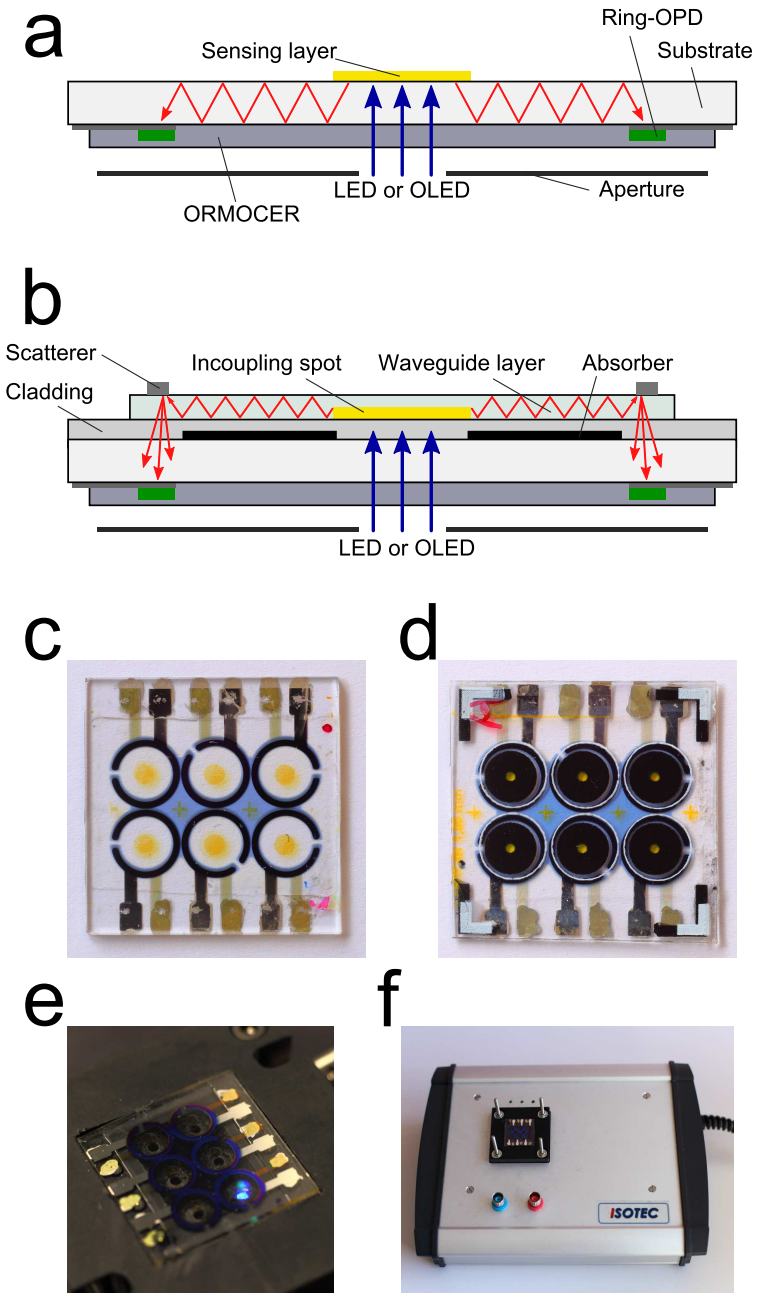

Figure 28: Schematic side view for the luminescence based (a) and absorption based (b) sensor chip (sizes are not to scale). Photos of the luminescence based (c) and absorption based (d) sensor chip, the sensor mount (e) of the readout-unit (f).

The sensor chip works as follows: The fluorophores in the incoupling spot are excited by the LEDs of the read-out unit and partly emit their fluorescence into the waveguide layer. The waveguided incoupled fluorescence is partially absorbed by the indicator dye immobilized in the waveguide layer and afterwards deflected toward the OPDs at the scatterer, and transformed into an electric signal. Meanwhile light from the excitation source or incoupling spot which is potentially coupled in the substrate is absorbed by the absorber. In analogy to the luminescence sensor chip no filters are needed for the absorption sensor chip.

Choice of materials

The OPDs, which were used for this project, resembled the Tang-type[22] pn-heterojunction device containg a p-type Conductor (CuPc) and n-type charge generating layer (PTCBI). The OPDs were encapsulated in ORMOCER® for protection against moisture, oxygen and mechanical damage. Advantages of these OPDs are their stability of its diode characteristic at non-inert conditions and their high on/off ratio of photocurrent during illumination to dark-current (3 to 5 magnitudes). Furthermore this OPD type exhibits almost no degradation at 0 V cell voltage, thus it was operated at short circuit conditions. Figure 2a illustrates the spectral sensitivity of the OPD, which shows a minimum at 450 nm and a maximum between 600 and 750 nm. All sensing systems were chosen matching these spectral parameters.

Oxygen sensing was performed using PtTFPP, PdTFPP and $Ir(C_S)_2(acac)$. Platinum and Palladium porphyrins as indicator dyes immobilized in polystyrene have been proven to be universally applicable oxygen sensing materials[23,24]. The brightness of PtTFPP and PdTFPP sensor foil was enhanced by using a Light Harvesting[25] system, immobilizing them together with the antenna dyes MFY and C545T. They feature high molar absorption coefficient, high quantum yield, absorption spectra matching the excitation wavelength and emission spectra overlapping to the absorption of PtTFPP and PdTFPP respectively. $Ir(C_S)_2(acac)$ is also a phosphorescent complex used for oxygen sensing featuring an outstanding molar absorption coefficient and quantum yield[26].

The carbon dioxide sensitive sensor layer is based on a dry chemistry approach by Mills[27]. The fluorescent indicator HPTS-TOA embedded in ethylcellulose as host polymer has been known as suitable for carbon dioxide sensing[28]. Their sensitivity can be tuned by varying the counter cation of the indicator dye HPTS, the ethyloxy content of EC and an organic base, which has to be immobilized together with HPTS in EC to form a buffer system stabilizing the carbon dioxide inside the matrix[27]. Excess TOA^+OH^- was added to improve the stability of the sensing layer.

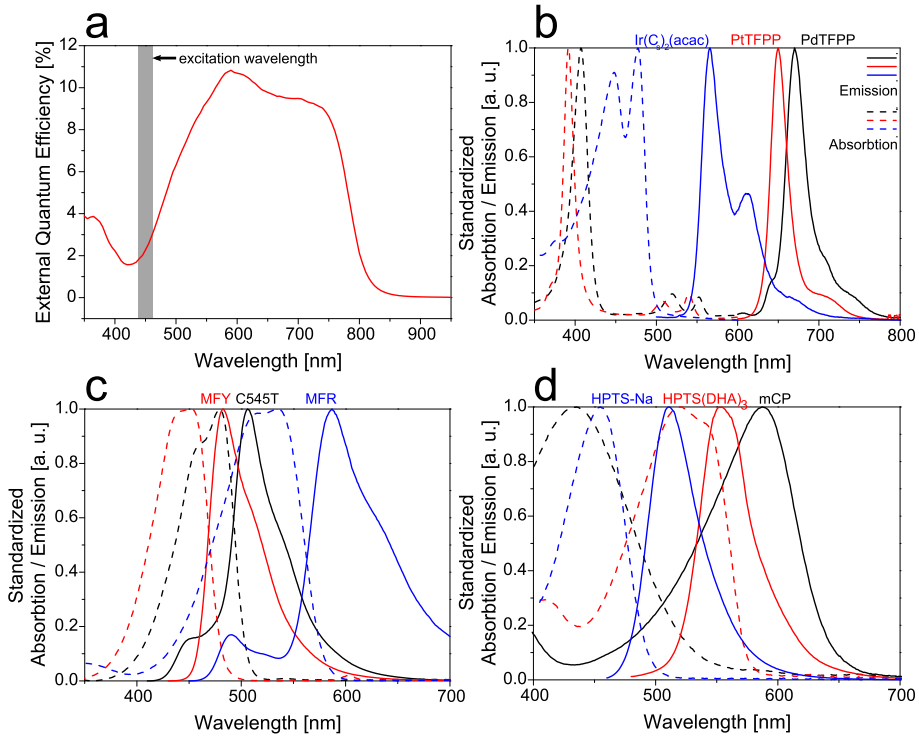

Figure 29: Spectra of used materials. (a) External quantum efficiency of the organic photodiodes. (b) Absorption (dashed) and emission (solid) spectra of PdTFPP (black), PtTFPP (red) and Ir(C_s)$_2$(acac). (c) Absorption (dashed) and emission (solid) spectra of C545T (black) MFY (red) and MFR (blue). Absorption (dashed) and emission (solid) spectra of HPTS-Na (blue) and HPTS(DHA)$_3$ (red), and absorption spectra of single protonated (solid) and twice protonated (dashed) forms of mCP (black). The grey bar highlights the emission wavelength of the excitation source.

The sensing layer for relative humidity is derived from the functional principle of a carbon dioxide sensor. It was adapted by exchanging the counter cation of the indicator dye HPTS to form a less sensitive carbon dioxide indicator and replacing the quaternary ammonium base TOA^+OH^- with and neutral phosphazene compound. This neutral compound forms together with water a quaternary ammonium base, which consecutively deprotonates the indicator dye [19].

HPTS(DHA)$_3$ - a liphophilized derivative of HPTS - immobilized in D7 – a hydrogel - was used for pH sensing[29]. D7 offers a high proton permeability but is nonpolar enough to sustain a suitable matrix for the highly lipophilic HPTS(DHA)$_3$. This property ensures that

the indicator does not leach into the aqueous test buffer, which is the case with pH-sensors based on non-covalently bonded hydrophilic indicators.

The incoupling spot of the absorption sensor chip consists of two different fluorophores – C545T and MFR in particular - entrapped in PS. Both feature a high molar absorption and a high quantum yield, furthermore they form a Förster resonance energy transfer[30] (FRET) pair due to their overlap of the donor's (C545T) emission and acceptor's (MFR) absorption spectra. This pair offers a high brightness and a high stokes shift necessary for the difference of excitation wavelength (450 nm) and emission wavelength (600 nm).

The mCP-TOA ion pair was used as carbon dioxide sensitive absorption dye[31], immobilized in EC with excess TOA^+OH^- in analogy to the HPTS-TOA carbon dioxide sensor.

Determination of detected excitation light

The amount of background illumination, most likely originating from the excitation source was determined. A glass slide was knife-coated with diluted cocktail of layer B. The luminescence of this layer was recorded depending of different oxygen concentration, as seen in Figure 3a. The peak area between 450 and 625 nm represents the fluorescence of the antenna dye MFY, the peak between 625 and 775 nm displays the phosphorescence of PtTFPP. Since dynamic oxygen quenching by oxygen occurs with phosphorescent molecules, the intensity of PtTFPP decreases while the intensity of MFY is constant.

Figure 3b shows the Stern-Volmer plot for dynamic phosphorescence quenching based on the data of Figure 3a. The black graph indicates the ratio of unquenched to quenched (I_0/I) area intensity of PtTFPP, calculated by generating the integral of the corrected spectra between 625 and 775 nm.

Since the integrated sensor chip lacks any kind of optical filter, the whole emitted spectrum of the sensing layer is detected by the OPD. The spectra were corrected by external quantum efficiency of the OPDs, the integrals were formed and visualized in the Stern-Volmer-Plot (Fig. 3b, red graph). This simulates a Stern-Volmer plot based on a measurement carried out on the integrated sensor chip with no background light.

The blue graph of Figure 3b represents a Stern-Volmer calibration of an oxygen sensor based on layer B, measured with the luminescence sensor chip. Both graphs are virtually congruent, the calculated value of I_0/I at 200 hPa partial oxygen pressure is 2.65

compared to the measured value 2.60. This infers that there is virtually no excitiation light detected.

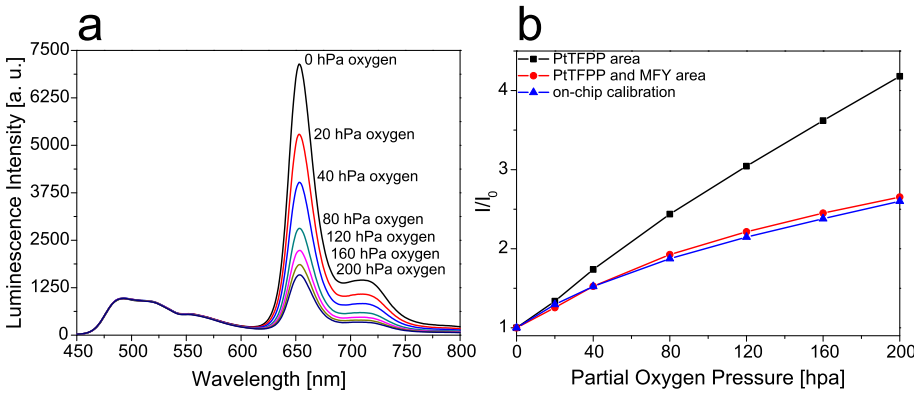

Figure 30: Emission spectra (a) of sensing layer B at different partial oxygen pressures. Stern-Volmer plot (b) based on area intensities of PtTFPP between 625 and 775 nm corrected by external quantum efficiency of the OPDs (black graph), on the whole spectral area corrected by external quantum efficiency of the OPDs (red graph) and on measurement on the luminescence sensor chip (blue graph).

Efficiency of the scattering ring

In order to determine the efficiency and the required dimensions of the scattering ring for the integrated absorption sensor a scattering test foil was prepared. It consisted of a scattering layer made of white screen-printing ink with holes of different diameters (4, 5, 6, and 7 mm) and 3 mm spots of layer F (incoupling spot) inside these latter mentioned holes. Both layers were screen-printed onto a 125µm thick Melinex (boPET) foil.

The highest intensity of scattered light occurs right at the edge of the scattering ring and drops below 3% of its initial intensity within 1 mm distance from the center following a sharp exponential decay. Therefore the ring thickness of the scattering ring and the ring thickness of the OPD-rings for the integrated absorption sensor does not need to exceed 1 mm. The alignment of the scattering ring perpendicular to the OPDs turned out to be a crucial part since the intensity drops within a fraction of a millimeter of the scatterer.

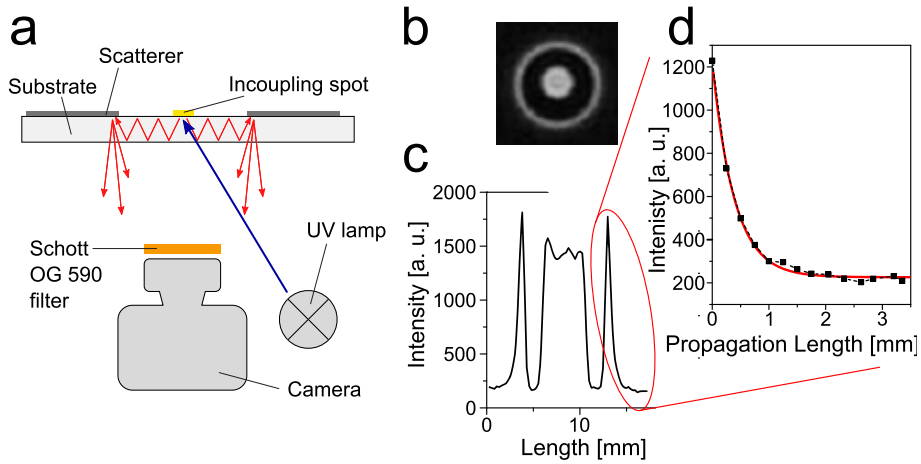

Figure 31: (a) Measurement setup to determine the out-coupling efficiency of the scattering ring (sizes are not to scale). (b) Recorded image of the scattering spots on the test foil, darker areas resemble less scattered light. (c) Intensity plot of a cross-section of the recorded image. (d) Intensity plot of the scatter ring depending on the distance from the edge (black dots) with an exponential decay fit (red graph).

Gas phase measurement with luminescence based sensor

The feasibility of carrying out single- and multi-analyte measurement with the luminescence sensor chip in gaseous media was shown with following analytes: oxygen, carbon dioxide and humidity.

Figure 5 shows the different response curves and calibration plots. An oxygen sensor array was tested, containing 3 different sensing layers (A, B and C). Each layer was printed twice on the sensor array containing 6 OPDs. The sensor response is shown in Figure 5a. The response time t_{90} is below 6 seconds for all 3 sensing layers. Figure 5b depicts the Stern-Volmer plots gained from the previous sensor response. The I_0/I values and deviations were averaged out of four measurements, obtained by two cycles of two spots per each layer. Layer A shows an I_0/I value of about 2.0 at 200 hPa partial oxygen pressure, which is consistent with reported values[24]. Layer B shows an I_0/I value of about 2.6, consistent with the measurement discussed in chapter 3.3. Layer C show a high sensitivity toward partial oxygen pressure below 20 hPa. By combining array elements with sensor spots comprising of layer A or B and C, oxygen concentration ranging from trace level to ambient condition can be covered on one sensor chip.

The sensor response and calibration of the HPTS-based carbon dioxide sensor (layer D) showed results as to be compared to reported values from the literature, as well

as the sensor response and calibration of the HPTS-based relative humidity sensor (layer E) as shown in Electronic Supplementary Material 2. Both sensors show a cross sensitivity, the carbon dioxide sensor toward relative humidity and vice versa. This performance is typical for gas-phase carbon dioxide sensing mechanisms based on pH indicators [19] To overcome this drawback, both parameters have to be monitored to measure reliably.

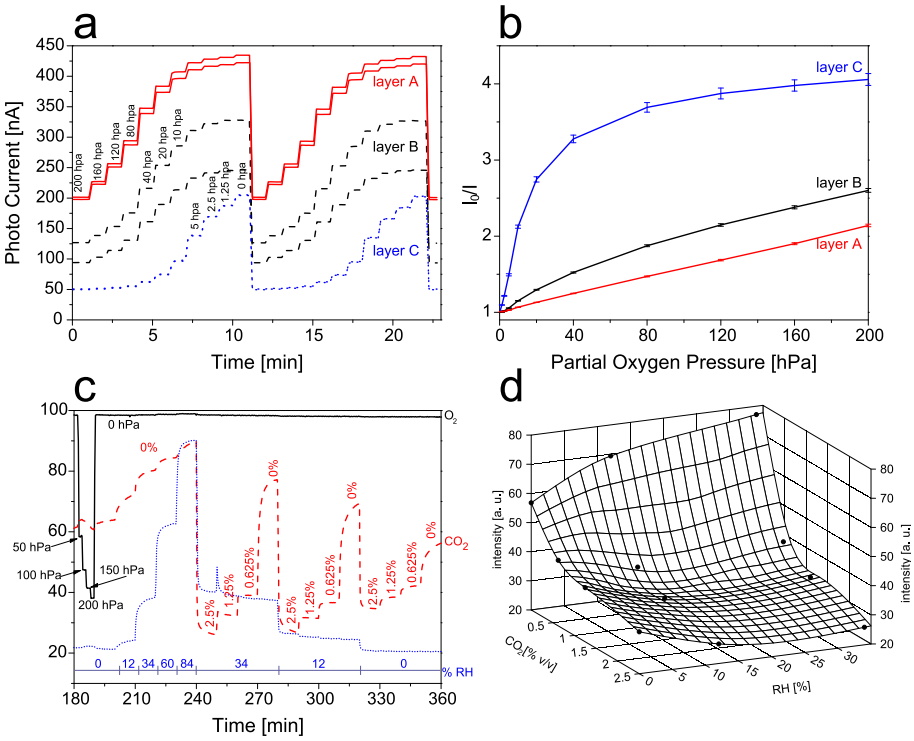

Figure 32: Gas phase measurements with luminescence sensor chip: Sensor response (a) and Stern-Volmer plot (b) of oxygen sensitive layers A, B and C. Sensor response (c) of multi-analyte sensor chip for the determination of oxygen (layer A, black solid line), carbon dioxide (layer D, red dashed line) and relative humidity (layer E, blue dotted line). Surface plot (d) to determine cross-sensitivity of carbon dioxide and humidity sensors toward each other based on the data shown in Fig 5c.

This is shown in Figure 5c, which depicts the sensor response of a multi-analyte sensor array, based on the three previously mentioned analytes. The sensor consisted of 6 spots of layer B, D and E, 2 of each screen-printed onto the sensor array. The oxygen sensor does not show any cross sensitivity toward humidity or carbon dioxide, because it is based on dynamic luminescence quenching unlike the sensing schemes for the latter

two analytes. The carbon dioxide sensor shows an increased sensitivity toward carbon dioxide at higher humidity. This is illustrated in Figure 5d. Hereby it is demonstrated, that the sensor chip can be used to compensate cross-sensitivity between different analytes.

Gas phase absorption based sensor waveguide

Two different sensors have been tested on the absorption based sensor waveguide. The first one consisted of (see Fig. 1b) layer F as incoupling spot and layer H as waveguide layer. Layer F consisting of analyte-insensitive fluorophores embedded in a PS matrix serves as incoupling part of the waveguide while layer H generates the analytical information by decreasing the light intensity of the guided light by absorption depending on the carbon dioxide concentration. The sensor shows a fairly quick t_{90} response time of 30 to 45 seconds and a high sensitivity between 1 and 100% carbon dioxide.

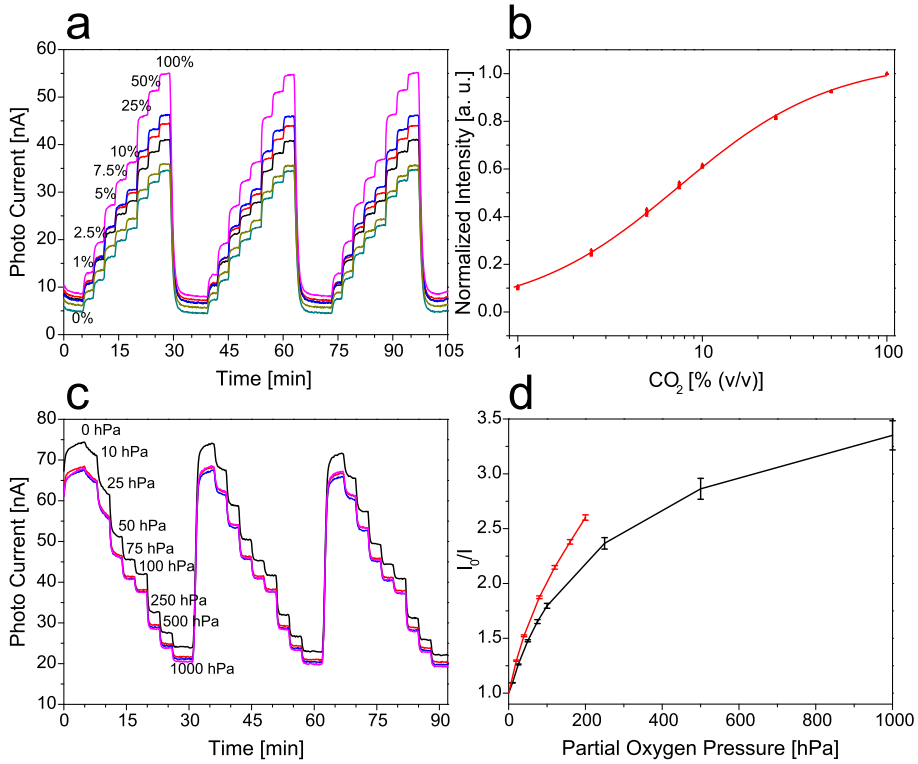

Figure 33: Gas phase measurements with absorption sensor chip: carbon dioxide sensor response (a) and calibration (b) based on layer H, oxygen sensor response (c) and Stern-Volmer plot based on layer B (d) of the absorption sensor chip (black graph) compared to the luminescence sensor chip (red graph).

Yet another absorption sensor chip has been tested, enabling to employ sensing schemes from the luminescence based onto the absorption sensor chip. The analytical information is gathered in the waveguide layer by absorption at latter mentioned sensor chip, while the analytical information of the oxygen sensitive layers (A, B and C) is gathered from change in luminescence of the central spot. To gain this information layer B was used as incoupling spot and a pured polymer layer (G) as waveguide layer. The analytical information is now gathered in the incoupling spot and the emitted luminescence is guided in the waveguide layer without any further sensitivity toward the analyte.

Figure 6c shows the sensor response between 0 and 1000 hPa oxygen indicating a response time t_{90} between 10 and 60 seconds. Figure 6d visualizes the Stern-Volmer plot of the sensor response shown in Figure 6c. The I_0/I value (2.20) at 200 hPa partial oxygen pressure of the absorption sensor chip is lower compared to the value of the same layer measure with the luminescence sensor chip (2.60). This indicates that while using this platform more excitation light is detected than using the luminescence sensor chip. Despite that the detected photocurrent is still sufficiently high to guarantee a reliable measurement with luminescence based sensor layers on the absorption sensor chip.

Liquid phase measurements

The proposed sensing platform is also suitable for measurements in aqueous media.

Figure 7a shows the response of an oxygen sensor based on layer A. An average drop of the photocurrent of 44% at 200 hPa and 51% at 0 hPa was observed compared to gas phase measurements. This is partially owed to the fact, that the self-made gasket for the liquid media cell covers a part of the OPD and the refractive index of the analyte media rises by the use of aqueous instead of gaseous media (n_{air} = 1 to n_{water}= 1.33), thus rising the critical angle for total reflection, which is a key characteristic of any waveguiding material. This leads to decreased amounts of guided light whereas the amount of background light is assumed to stay constant, leading in a decreased sensing efficiency. Further a response time t_{90} of about 30 seconds was observed at highest flow rate, increasing up to 3 minutes at a twentieth of the maximum flow rate. This suggests that the mass transport is a limiting factor in measuring liquid phase media in this setup.

Figure 7c shows the response curve of an optical pH sensor. The average response time t_{90} is 5 minutes. Figure 7d depicts the calibration gained by the response curves of Figure 7c. All sensor responses have been normalized to [0;1] resulting in an sigmoidal calibration characteristic. All four sensor responses show the same inflection point (pK_a) at 8.36 and the same slope (0.46) when normalized to [0;1].

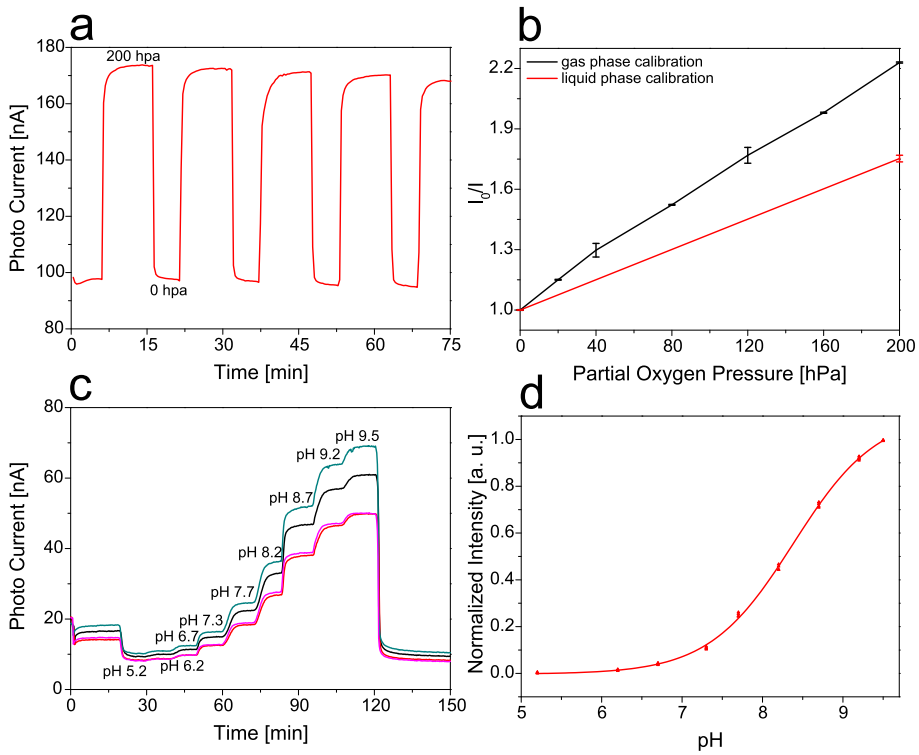

Figure 34: Liquid phase measurements with luminescence based platform: oxygen sensor response (a) and Stern-Volmer plot (b) comparing gas phase (black graph) and liquid phase (red graph) measurements based on layer A; pH sensor response (c) and sigmoid calibration (d) based on layer I.

Reproducibility of calibration values between different chips

All presented sensors are based on intensity measurement and, as shown in Figure 5a even identical layers on the same platform can differ in its intensity. This can be related to misaligned spots while screen-printing, deviations in the luminosity of the excitation source, or variations in the OPD qualities.

Three different luminescence sensor chips have been coated with layer B and calibrated to proof that calibration characteristics do not change from one chip to another. I_0/I values of these three sensor chips were determined to be 2.61±0.03 for the first, 2.63±0.01 for the second and 2.63±0.01 for the third sensor chip. The average I_0/I value for all three chips is 2.62±0.03. This shows evidently no change in the sensor layer characteristics over different sensor chips.

Conclusion and outlook

An optical sensor chip is presented which features monolithically integrated organic photodiodes on different substrates such as glass or polymeric foil and an absence of optical filters due to a geometrically based separation between background light from the excitation source and analytically relevant fluorescence. The background signal was determined to be insignificant. Sensing schemes for four different analytes (oxygen, carbon dioxide, relative humidity, and pH) in aqueous and gaseous media based on luminescence and absorption sensing mechanisms have been applied. Both sensing mechanisms use the same organic photodiode design and substrate.

In current studies we are investigating different referencing systems within the sensor layer, based on lifetime to enable calibration-free or factory calibration. In addition we are also evaluating a simple integration method to combine this platform with microfluidics.

Acknowledgement

Financial support by the Austrian Research Promotion Agency (FFG) in the framework of the Austrian Nano Initiative (Research Cluster 0700 – ISOTEC) is gratefully acknowledged. We thank PhD Sergey Borisov and Klaus Koren for the synthesis of HPTS(DHA)$_3$ and Ir(C$_s$)$_2$(acac).

---

[1] Wolfbeis OS (2005) Materials for fluorescence-based optical chemical sensors. J Mater Chem 15: 2657–2669

[2] McDonagh C, Burke CS, MacCraith BD (2008) Optical Chemical Sensors. Chem Rev 108:400–422

[3] Schmidt O, Bassler M, Kiesel P, et al. (2007) Fluorescence spectrometer-on-a-fluidic-chip. Lab Chip 7:626–629

[4] Chediak JA, Luo Z, Seo J, et al. (2004) Heterogeneous integration of CdS filters with GaN LEDs for fluorescence detection microsystems. Sens Actuators A 111:1–7

[5] Daw R, Finkelstein J (2006) Lab on a chip. Nature 442:367–367

[6] Verpoorte E (2003) Focus. Lab Chip 3:42N–52N

[7] Mogensen KB, Klank H, Kutter JP (2004) Recent developments in detection for microfluidic systems. Electrophoresis 25:3498–3512

[8] Peumans P, Yakimov A, Forrest SR (2003) Small molecular weight organic thin-film photodetectors and solar cells. J Appl Phys 93:3693–3723

[9] Song QL, Li FY, Yang H, et al. (2005) Small-molecule organic solar cells with improved stability. Chem Phys Lett 416:42–46

[10] Lamprecht B, Thünauer R, Köstler S, et al. (2008) Spectrally selective organic photodiodes. Phys Status Solidi RRL 2:178–180

[11] Lamprecht B, Thünauer R, Ostermann M, et al. (2005) Organic photodiodes on newspaper. Phys Status Solidi A 202:R50–R52

[12] Savvate'ev V, Chen-Esterlit Z, Aylott JW, et al. (2002) Integrated organic light-emitting device/fluorescence-based chemical sensors. Appl Phys Lett 81:4652–4654

[13] Qiu Y, Yao B, Luo G, et al. (2005) A microfluidic device using a green organic light emitting diode as an integrated excitation source. Lab Chip 5:1041—1047

[14] Pais A, Banerjee A, Klotzkin D, Papautsky I (2008) High-sensitivity, disposable lab-on-a-chip with thin-film organic electronics for fluorescence detection. Lab Chip 8:794–800

[15] Ryu G, Huang J, Hofmann O, et al. (2011) Highly sensitive fluorescence detection system for microfluidic lab-on-a-chip. Lab Chip 11:1664–1670

[16] Novak L, Neuzil P, Pipper J, et al. (2007) An integrated fluorescence detection system for lab-on-a-chip applications. Lab Chip 7:27–29

[17] Shinar J, Shinar R (2008) Organic light-emitting devices (OLEDs) and OLED-based chemical and biological sensors: an overview. J Phys D 41:133001

[18] Borisov S, Krause C, Arain S, Wolfbeis OS (2006) Composite Material for Simultaneous and Contactless Luminescent Sensing and Imaging of Oxygen and Carbon Dioxide. Adv Mater 18:1511–1516

[19] Schröder CR, Klimant I (2005) The influence of the lipophilic base in solid state optical pCO2 sensors. Sens Actuators B 107:572–579

[20] Lamprecht B, Abel T, Kraker E, et al. (2010) Integrated fluorescence sensor based on ring-shaped organic photodiodes. Phys Status Solidi RRL 4:157–159

[21] Lamprecht B, Kraker E, Sagmeister M, et al. (2011) Integrated waveguide sensor utilizing organic photodiodes. Phys Status Solidi RRL 5:344–346

[22] Tang CW (1986) Two-layer organic photovoltaic cell. Appl Phys Lett 48:183–185

[23] Lee S-K, Okura I (1997) Photostable Optical Oxygen Sensing Material: Platinum Tetrakis(pentafluorophenyl)porphyrin Immobilized in Polystyrene. Anal Commun 34:185–188

[24] Douglas P, Eaton K (2002) Response characteristics of thin film oxygen sensors, Pt and Pd octaethylporphyrins in polymer films. Sens Actuators B 82:200–208

[25] Mayr T, Borisov SM, Abel T, et al. (2009) Light Harvesting as a Simple and Versatile Way to Enhance Brightness of Luminescent Sensors. Anal Chem 81:6541–6545

[26] Borisov SM, Klimant I (2007) Ultrabright Oxygen Optodes Based on Cyclometalated Iridium(III) Coumarin Complexes. Anal Chem 79:7501–7509

[27] Mills A, Eaton K (2000) Optical sensors for carbon dioxide: an overview of sensing strategies past and present. Quim Anal 19:75–86

[28] Neurauter G, Klimant I, Wolfbeis OS (2000) Fiber-optic microsensor for high resolution pCO2 sensing in marine environment. Fresenius J Anal Chem 366:481–487

[29] Borisov SM, Herrod DL, Klimant I (2009) Fluorescent poly(styrene-block-vinylpyrrolidone) nanobeads for optical sensing of pH. Sens Actuators B 139:52–58

[30] Förster T (1948) Zwischenmolekulare Energiewanderung und Fluoreszenz. Ann Phys 437:55–75

[31] Sipior J, Bambot S, Romauld M, et al. (1995) A Lifetime-Based Optical CO2 Gas Sensor with Blue or Red Excitation and Stokes or Anti-Stokes Detection. Anal Biochem 227:309–318

Fast responsive, optical trace level ammonia sensor for environmental monitoring

Tobias Abel[*], Birgit Ungerböck[*], Ingo Klimant* and Torsten Mayr[*,~]

*Institute of Analytical Chemistry and Food Chemistry, Graz University of Technology, Stremayrgasse 9, 8010 Graz, Austria

~ Corresponding author

Telephone: +43 (316) 873 – 32504

Fax: +43 (316) 873 - 1032504

E-Mail: torsten.mayr@tugraz.at

Published in: Chemistry Central Journal

Submitted: 7th of September, 2012

Abstract

Background

Ammonia is a ubiquitous chemical substance which is created in technical and biological processes and harmful to many different organisms. One specific problem is the toxicity of ammonia in fish at levels of 25 µg/l - a very common issue in today's aqua culture. In this study we report a development of a fast responsive, optical ammonia sensor for trace concentrations.

Results

Different hydrogels have been investigated as host polymers for a pH based sensing mechanism based on fluorescent dyes. A porous hydrophobic fluoropolymer membrane was used as an ion barrier cover layer to achieve a good ammonia permeability. The sensor's sensitivity towards ammonia as well as crosssensitivity towards pH-value and salinity, and the temperature dependency have been determined. Two different methods to reference fluorescence signals have been employed to eliminate intensity-based measurement drawbacks.

Conclusion

The presented sensor features high sensitivity and a fast response even at concentrations near 1 ppb. No cross sensitivity towards pH and salinity could be observed and temperature dependency was determined as compensateable. Both referencing approaches prove themselves to be able to provide a simple use of the sensor for in-field applications

Keywords

Optical sensor, ammonia sensor, fluorescence sensor, fish farming, aqua culture, dual lifetime referencing, two wavelength ratiometric referencing,

Background

Ammonia is a very widespread chemical in our world. It is not only present in substances like refrigerants, household cleaners, and (most abundantly) industrial fertilizers, but is also produced in nature by all animal cells[1] resulting from degradation of amino acids[2], food putrefaction[3], excretion, and decomposition of waste and sewage. Due to this broad use and existence of ammonia it can be found in the atmosphere[4], the soil[5], as well as in river-[6] and seawater[7]. Furthermore ammonia is toxic to any kind of animals, from microorganisms[8] to more differentiated life forms[9]. These circumstances lead to an increasing demand for robust, cheap and continuous means of measuring ammonia in environmental monitoring, food processing and medical applications[10]. This study approaches the problem of ammonia monitoring in the aquatic habitat. The developed sensor is suitable for the application in fish farming[11], which itself is a try to lessen global overfishing while providing fish for global demands.

Many different methods have been employed for analytical detection of ammonia, such as flow spectrometrics[12], potentiometric electrodes[13], IR absorption[14], amperometric[6] and conductive[15] measurements, or spectrophotometric approaches based on the Berthelot reaction[16] or on Nessler's method[12]. However, these methods consume chemicals, need batch separation from the analytical sample, or require sample pretreatment and/ or expensive instrumentation, which prevent these approaches being applied for continuous and simple monitoring tasks. Optical ammonia sensors[17,18,19] based on pH-indicators can fulfill these conditions, since they can be manufactured low-cost in high quantities and used with simple instrumentation without sample pretreatment.

In this study we present an optical ammonia sensor based on commercially available materials, simple in both manufacturing and operation, designed to fulfill ammonia monitoring functions as demanded in modern fish farms. The ammonia sensitive layer consists of a hydrogel in which two non-sensitive, fluorescent dyes and a non-fluorescent pH-indicator are entrapped. The two fluorescent dyes and the indicator form a Förster resonance energy transfer[20] (FRET) cascade due to their overlapping emission and absorption spectra of the FRET donor and acceptor respectively. The pH-indicator is protonated in absence and deprotonated in presence of ammonia, changing its absorption spectra and quenching the FRET emission in the presence of ammonia. The analytical information is gained by measuring the cascade's fluorescence intensity. To overcome problems of varying fluorescence intensities derived from differing layer thicknesses and power attenuation by the instrumentation we employed two different reference methods, one of which even allows ratiometric imaging techniques using the color channels of a CCD camera[21].

Results and discussion

The general build-up of an optical ammonia sensor is based on a hydrophilic polymer, in which the sensing chemistry is immobilized, entrapped sandwich-like between a supporting material and a proton barrier, which permits a permeation of ammonia but prohibits a penetration of protons into the host material.

Choice of indicators and dyes

The main characteristic which defines the dynamic range of an ammonia sensor based on pH indicators is the pK_a of said indicator. Ammonia, which migrates into the host material, deprotonates the indicator and forms an ammonium salt with the indicator as counter ion, as described by equation 9. Though there are some ammonia sensors based on fluorescent indicators[22,23,24], the majority rely on absorbance-based pH indicators [17,25,26,27,28], since there are more indicators in a broader pK_a range available.

$$NH_3 + IndH \rightleftharpoons NH_4^+ + Ind^- \quad (9)$$

The used indicator was bromophenol blue (BPB) with a pK_a of 4.1[17]. The indicator shows different absorbance spectra within the visible field. The deprotonated form shows an absorbance maximum at 600 nm while the protonated form shows an absorbance maximum at 425 nm (see Figure 1 for normalized spectra). Thus, absorbance carries the analytical information. However, absorbance cannot be as easily measured (e.g. by reflection in thin polymer films) as fluorescence. For this reason two more dyes were introduced, which form a FRET cascade: a donor (Coumarin 545T or “C545T”), an acceptor (Macrolex Fluorescent Red G or “MFR”) and a quencher (BPB). The donor is excited and transfers its energy to the acceptor dye, emitting subsequently light at 600 nm. This is prevented, if in presence of ammonia the indicator’s deprotonated form is within the membrane, because the energy will then be passed from MFR onto the indicator and the emission diminishes. This approach offers additional advantages: Due to the excitation by energy transfer, photo bleaching of the pH indicator can be minimized. Furthermore, high intensities can be obtained by an increased donor concentration, increasing the absorbance of excitation light[29].

The indicator and dyes necessary for the different referencing techniques are discussed within the specific subchapters.

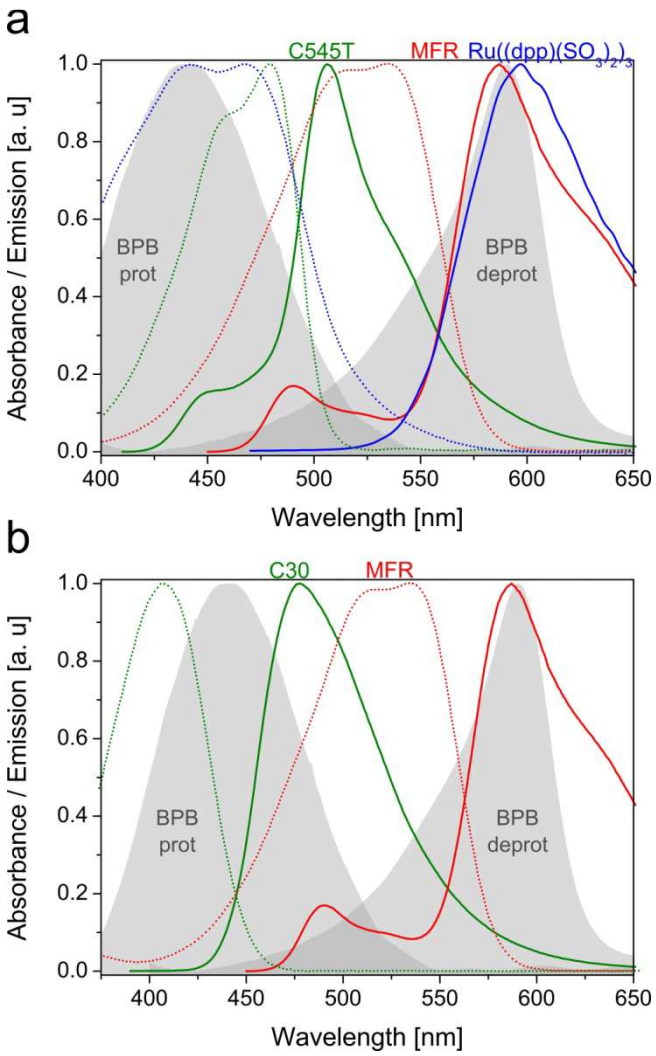

Figure 1: Absorbance and emission spectra of used sensor compositions. Figure 1a shows the DLR system: absorbance (dotted line) and emission (solid line) spectra of Coumarin 545T (green), Macrolex Fluorsecent Red (red) and the Ruthenium complex (blue) as well as the absorbance spectra for the protonated and deprotonated forms of bromophenol blue (grey areas). Figure 1b shows the TWR system: absorbance (dotted line) and emission (solid line) spectra of Coumarin 30 (green), Macrolex Fluorsecent Red (red) as well as the absorbance spectra for the protonated and deprotonated forms of bromophenol blue (grey areas).

Choice of polymers

There are some important properties a polymer has to fulfill to be considered as host material for an ammonia sensor: The host polymer has to stabilize both the hydrophilic ammonium and the hydrophobic protonated indicator, which means that the polymer's hydrophilicity is a key factor for sensitivity and stability of the sensor. Furthermore the polymer must not have alkaline properties, so that the protonated form of the pH indicator is stable inside the membrane.

Cellulose esters have been used as host polymers[23,24], since they fulfill these requirements. Hydrogels even surpass these characteristics. Their water absorption (70, 50 and 30% for HydroMed D1, D4 and D7 respectively[30] and their strong adhesion properties make them a very suitable choice. As seen in Figure 2a these hydrogels outperform cellulose acetate (CA) in terms of detectable concentration ranges. This is a very crucial requirement, since ammonia displays toxicity towards aquatic and amphibic organisms at concentrations of even 25 µg/l. CA shows 50% of the maximum intensity decrease at about 90 µg/l ammonia, the hydrogels D7, D4 and D1 undermatch this at concentrations of 13, 1 and 2 µg/l respectively. This shows that the sensitivity of the same sensing chemistry is higher in hydrogels than in CA.

Choice of proton barrier

Ammonia sensors based on a pH sensitive layer require a proton barrier for liquid samples to prohibit a response to the pH of the tested sample. Different materials have been used; silicon being the probably most widespread reported one[23,24,26,] The proton barrier has to feature two properties: impermeability for protons and permeability for ammonia. Facing minimal concentrations during trace measurements, reassuring a high permeability is of the utmost importance to keep the sensors' response time within reasonable limits.

In the study presented a PTFE-based membrane filter (Millipore Fluoropore™ Membrane Filter) has been used, displaying not only the strong hydrophobic properties of technical fluoropolymers, but also an extraordinary permeability for ammonia[31,32] due to its highly porous structure[33]. Moreover the white, reflective filter surface offers the possibility to keep the analyte sensitive layer thickness below two micro meter whilst maintaining a sufficiently high signal level and minimizing response times. Moreover fluoropolymers offer a high resistivity against biofouling and thus the establishment of biofilms on the sensor's surface[34], which can be deteriorating the sensor performance.

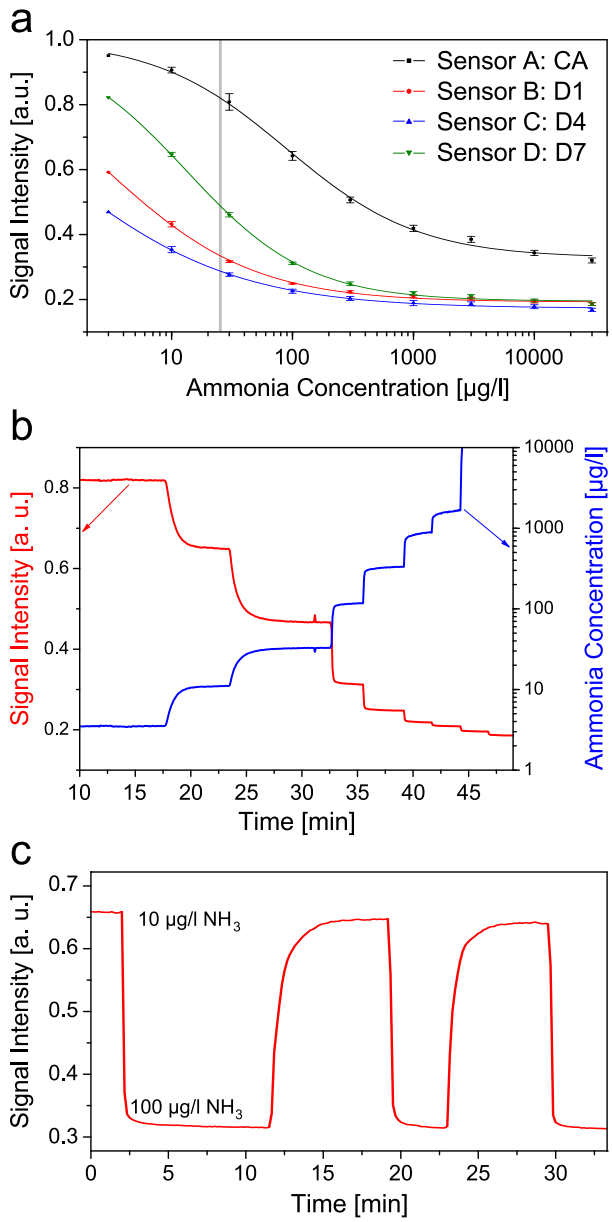

Figure 2: Sensitivity and response of the ammonia sensor. (a) Calibration plots for ammonia sensors A, B, C, and D in a concentration range between 3 and 30,000 µg/l with a view to the ammonia toxicity level in fish of 25 µg/l (grey line) (mean values from 6 sensor layers); (b) time resolved signal response (red graph) and calculated concentrations (blue graph) based on sensor B; (c) response and recovery response of sensor B between 10 and 100 µg/l ammonia in 100 mM phosphate buffer at pH 7.2.

Sensor response times

Due to the used filter membranes and the thin polymer layer it was possible to achieve very short response times. The response time t_{90} for a change between 3 µg/l and 10 µg/l is about 120 seconds (see Figure 2b). The t_{90} response time and the recovery response time between 10 µg/l and 100 µg/l were determined to be 60 and 50 seconds respectively (see Figure 2c), decreasing with higher concentrations down to 20 seconds. This sensor clearly outperforms silicon as proton barrier, of which t_{90} response times of 30[26], 40[23], even 70[35] minutes have been reported.

The sensors employing hydrogels (sensor B, C and D) displayed slightly shorter response times between 10 µg/l and 100 µg/l (60, 60 and 50 seconds respectively) than the same setup using cellulose acetate (sensor A, 90 seconds), which demonstrates that the ammonia permeability is in hydrogels higher than in cellulose acetate.

Cross sensitivity and dependencies

Different tests were carried out to assess the sensors' cross sensitivity. The impermeability towards protons is demonstrated as seen in Figure 3a. No change of signal intensity could be registered, even with pH buffers far beyond the pK_a value of the used indicator.

Also the sensor's cross sensitivity towards varying salinities was evaluated (see Figure 3b). Taking into account that the ammonia-ammonium equilibrium changes with salinity (which can be mathematically compensated[36]), the sensor shows virtually no divergence in its calibration in ammonia solutions containing 3.5 %(w/w) sodium chloride compared to sodium chloride free solution.

There is a specific dependency in terms of temperature. Figure 3c show three different calibrations, all carried out with the identical sensor and buffers. The ammonia concentration was corrected for the shifted ammonia-ammonium equilibrium (see experimental section, equation 11). Still, a slight dependency towards temperature was measured within the relevant concentrations. This can be attributed to the universal characteristic of increased fluorescence at lower temperatures and a temperature dependency of the indicator's pKa.

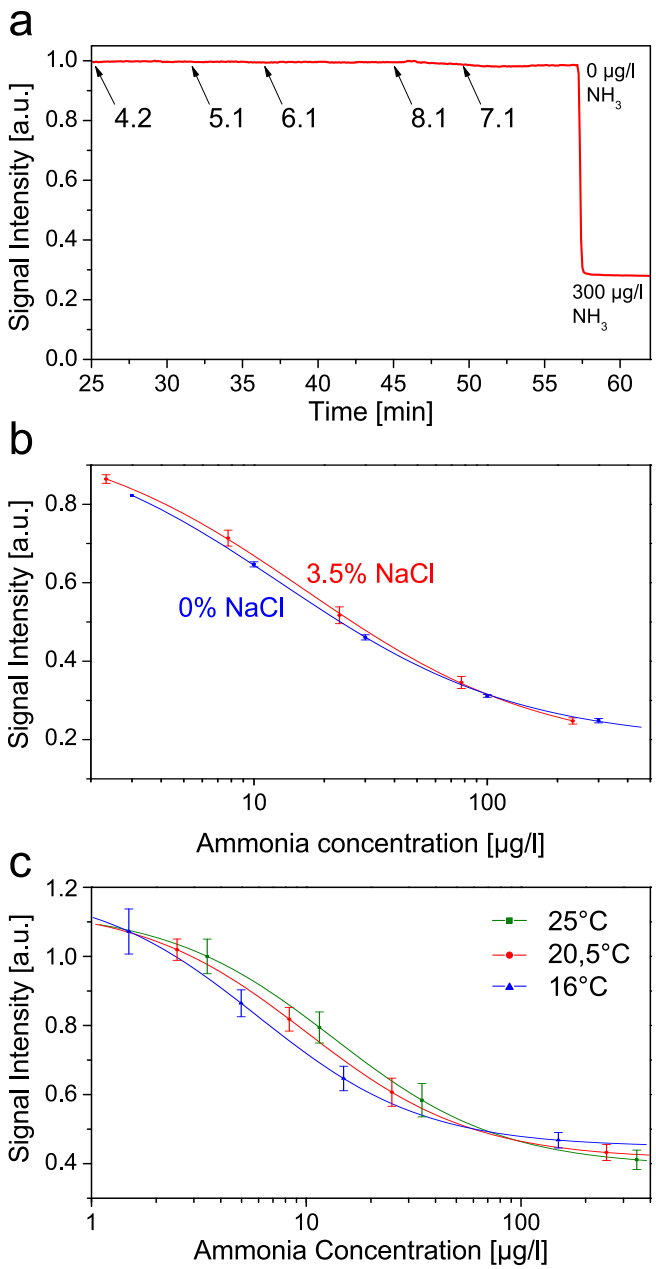

Figure 3: Cross sensitivity and temperature dependency. Cross sensitivity and temperature dependency of sensor B towards pH (a) and salinity (b, mean value of 4 sensor foils), and temperature dependency (c, mean value of 4 sensor foils).

Dual-Lifetime Referencing (DLR)

All measurements so far discussed are intensity based; those measurements are error-prone in real-world applications. These errors can result from manufacturing inhomogenities, different alignments, or varying performances of read-out units. Therefore, we investigated the application of two different signal referencing methods to overcome the limitations of intensity measurements to obtain a universal and user friendly system suitable for field measurements.

The first reference method employed is Dual Lifetime Referencing[22,37,] (DLR). This method requires a phosphorescent reference dye featuring a long decay time, equal excitation and emission wavelengths as the sensing chemistry and no sensitivity towards the analyte or other substances. Silica particles were chosen as host material due to their simple synthesis, their insolubility in organic solvents, and their low oxygen permeability. These particles contained a phosphorescent Ruthenium complex, which would be an oxygen-sensitive probe unless incorporated inside the gas-impermeable spheres. These spheres are evenly dispersed in the sensor cocktail during the manufacturing process and homogenously distributed in the host polymer. Furthermore, it was necessary to decrease the sensors brightness (compared to intensity measurements) by reducing the FRET-pair donor's concentration to match the luminescence intensities of the sensing chemistry and the reference.

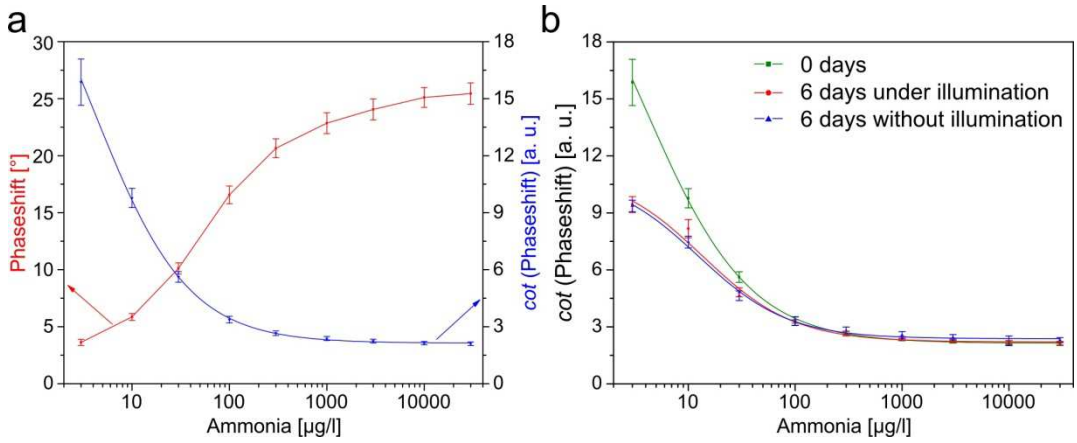

Figure 4: DLR calibration and longtime stability of sensor E. (a) Calibration of sensor E based on phaseshift measurements (red graph mean value of 2 sensor foils) and calculated correlating cotangent values (blue graph); (b) longtime stability comparing illuminated sensors (red graph, mean value of 4 sensor foils) and non-illuminated sensors (blue graph, mean value of 6 sensor foils)

The measurement is carried out with a sinusoidally modulated light source, which excites the indicator and the reference particles. The detected signal exhibits a high or low phase shift, depending on the ratio of the intensities of the reference and the indicator. Figure 4a depicts the calibration curve of the presented DLR-referenced sensor. The red graph shows the measured phase shifts. The blue graph shows the calculated cotangent values, which is directly proportional to the indicators intensity. It has to be remarked, that the high deviation at 3 µg/l is not originated by measurement problems, but is derived from the steepness of the cotangent functions at values next to zero.

Figure 4b shows a longtime stability test carried out for 6 days in two different methods: Both sensor batches were characterized on the first and sixth day and stored in between in a buffer containing 100 µg/l ammonia. One batch was stored in complete darkness while the other batch was illuminated (6 samples per minutes over the period of 6 days equals 8600 measurement points) to investigate if the drop in signal was caused by photo bleaching. Both tested sensor batches show a drop of the cotangent-values at low ammonia concentrations after 6 days while maintaining the signal values at higher concentration. Since both sensor calibrations drop the same amount it is assumed, that the sensor itself is not prone to photo bleaching but may suffer from leaching or migration problems due to incomplete encapsulation of the indicator and reference dyes. Despite this change in sensor characteristics a recalibration and further use of the tested sensors is still possible.

Two Wavelength Ratiometric (TWR)

A second referencing method was employed; based on ratiometric measurement of two different emission intensities recorded at two different bands of wavelength. The sensing chemistry was modified to gain two different emission peaks with sufficient difference in wavelength and comparable ranges of emission intensity over the whole range of tested ammonia concentrations. The previously used FRET donor, Coumarin 545T, was exchanged for Coumarin 30 (C30), a dye similar in absorbance and quantum yield but featuring shorter absorption and emission wavelengths, which was crucial to obtain two distinctly separated emission peaks. The reduced overlap of the C30 emission and the acceptors absorption spectra (MFR) leads to a decreased FRET efficiency and in noticeable emission of the donor in the region of 470 nm (see Figure 5a).

This FRET cascade is combined with the BPB indicator forming the ammonia sensing system. BPB shows two different absorbance bands, its protonated form overlaps the donor’s (C30) emission and the deprotonated form overlaps the acceptor’s (MFR) emission. This leads to an opposing change in intensities with ascending ammonia concentrations, namely an increasing emission of the donor and a decreasing emission of

the acceptor (see Figure 5a). The signal can be referenced by dividing the intensity of the 625 nm peak by the intensity of the 470 nm peak, either mathematically from a spectrum (see Figure 5a), by a measurement with two different band pass filters or by imaging techniques with a color camera (see Figure 5b).

For the “two filters approach” a lock-in amplifier was used, connected with a 405 nm LED, a trifurcated fiber bundle and two PMT tubes with two different band pass filters for each emission peak. The emission intensity of both peaks was measured and referenced by dividing the red by the blue channel. Figure 5c depicts a longtime measurement in analogy to Figure 4b. Again a drop in fluorescence intensity can be observed independent from the factor of illumination. Despite this drop the sensor itself is still functional and can be used by further recalibration.

This ratiometric referencing approach also offers the possibility to use imaging methods[38]. Figure 6 depicts different images of the sensor’s surface recorded with a commercially available color camera. The different color channels (red and blue) were separated, analyzed digitally and divided by each other. Both measurement approaches show the same sensor characteristics but differentiate in terms of signal resolution and sensitivity due to different spectral sensitivities of the channels or filters. This shows that this sensor not only can be used for batch measurements but also for imaging and spatial resolution applications, as it has been proven to be useful in marine research by mapping oxygen concentration and pH distributions via imaging techniques[21].

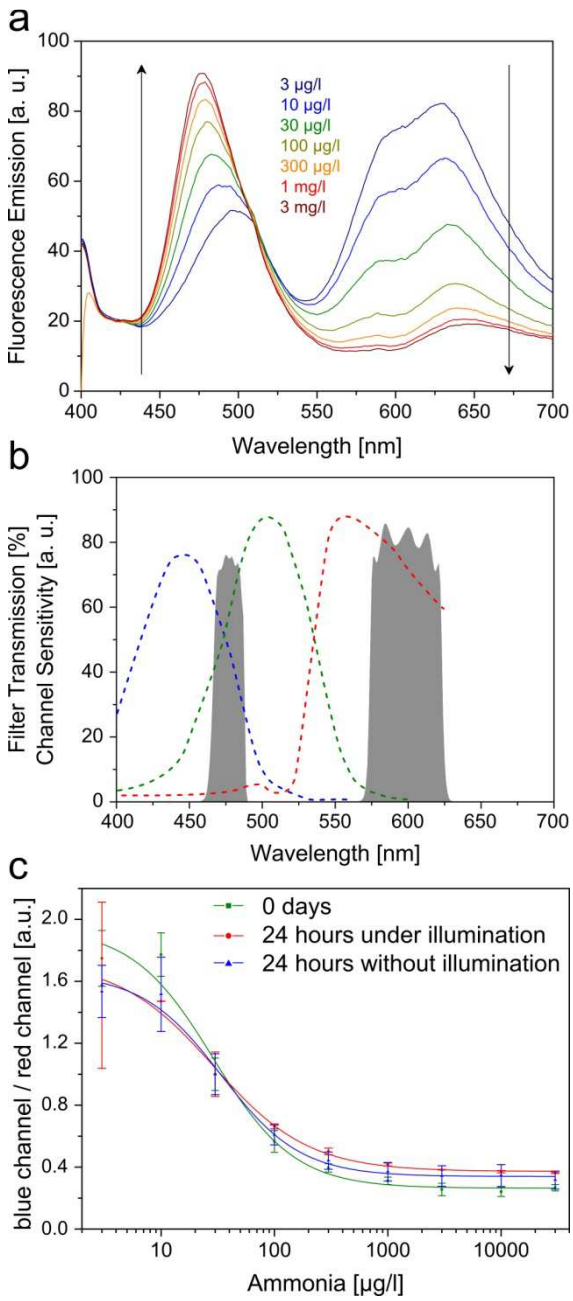

Figure 5: Sensor and instrumentation characteristics of two-wavelength ratiometric referenced sensor.
(a) Fluorescence emission spectra of sensor F at different ammonia concentrations; (b) spectral sensitivity for blue, green and red of the color camera's RGB sensor (dotted lines) and used bandpass filters (grey areas); (c) over the period of 24 hours comparing illuminated sensors (red graph mean value of 2 sensor foils) and non-illuminated sensors (blue graph mean value of 4 sensor foils)

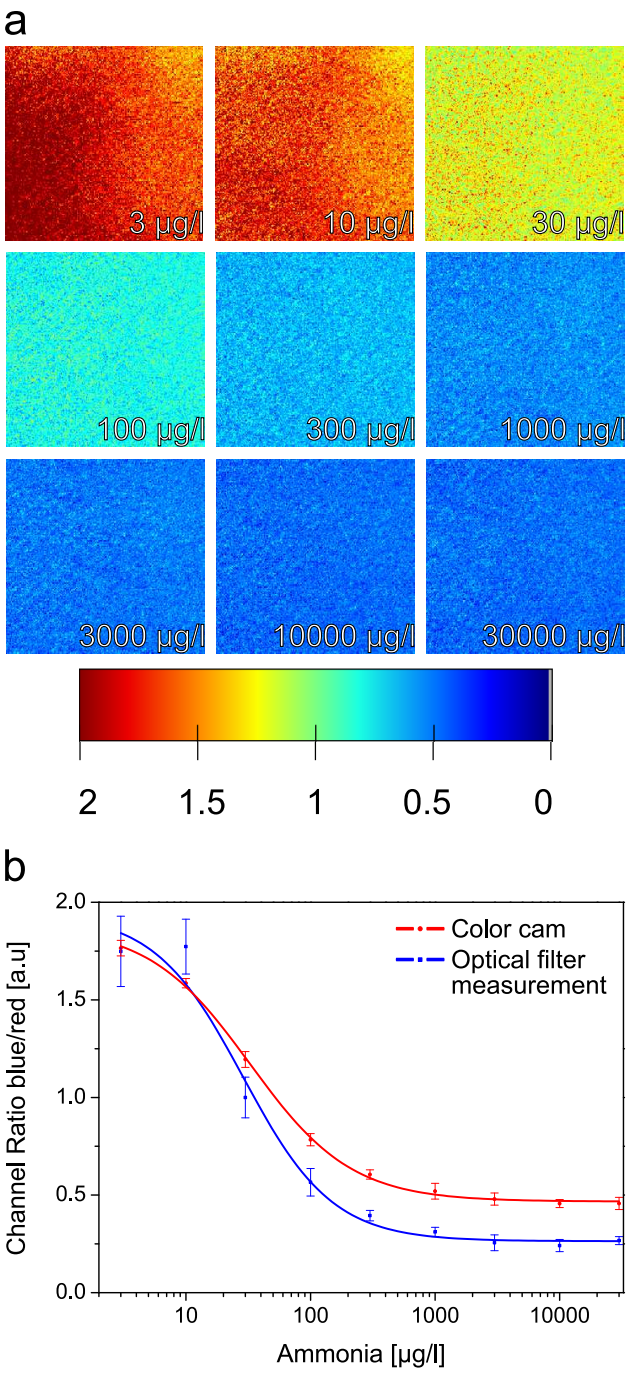

Figure 6: False color imaging pictures and comparison to optical filter measurement. False color imaging pictures (a) taken with a color camera and processed with MathWorks MATLAB (calculation of blue/red channel ratio) and comparison of the mean values of the channel ratio with a calibration carried out with the optical filter measurement approach.

Experimental

Materials

1H,5H,11H-[l]benzopyrano[6,7,8,ij]quinolizin-11-one (Coumarin 545T or C545T) and 3-(2-N-Methylbenzimidazolyl)-7-N,N-diethylaminocoumarin (Coumarin 30 or C30) were purchased from Sigma Aldrich Chemie GmbH (Steinheim, Germany). 3-(benzothiazol-2-yl)-7-(diethylamino)-2-oxo-2H-1-benzopyran-4-carbonitrile (Macrolex Fluorescent Red G or MFR) was purchased from Simon & Werner GmbH (Flörsheim am Main, Germany). Bromophenole blue (BPB), Tetraethoxysilane (TEOS) and celluloseacetate (CA) were obtained from Acros Organics (Geel, Belgium). Tetrahydrofuran (THF), N-Cyclohexyl-2-aminoethanesulfonic acid (CHES), acetic acid, sodium dihydrogen phosphate, disodium hydrogen phosphate and sodium chloride were bought from Carl Roth GmbH (Karlruhe, Germany). Hydrogel D1, D4 and D7 were obtained from CardioTech International Inc. (Wilmington, MA, United States). Millipore FHUP Fluoropore™ Membrane Filter was bought from EMD Millipore Corporation (Billerica, MA, United States). ($Ru[dpp(SO_3Na)_2]_3)Cl_2$) was synthesized in lab following to published results[39].

Synthesis of reference particles

The reference particles were prepared analogically as reported before[40]. 3.86 g of TEOS was poured into a solution of 4 ml acetic acid, 1.25 ml and 0,02 mg $Ru(dpp(SO_3)_2)$. The mixture was stirred vigorously right away for 5 minutes and after waiting 30 minutes it was filtered with a Macherey-Nagel MN 619 cellulose filter. The obtained particles were washed two times each with deionized water, ethanol, and acetone. In the end the particle were dried for 24 hours at 80°C in a drying oven.

Sensor preparation

The sensor layers were prepared by coating sensor cocktails onto a Melinex boPET foil (DuPont Teijin Films, Middlesbourgh, UK). Cocktails consisted of the two fluorescent dyes, the indicator, the polymer, and (in case of cocktails for DLR-referenced foils) the particles, dissolved in THF (see Table 1 for sensor cocktail composition). The cocktails were spread onto the foil using a drawdown bar film applicator (wet film thickness 25.4 µm) purchased from BYK-Gardner GmbH (Geretsried, Germany). Immediately after the spreading step, a FHUP Fluoropore™ membrane filter was laid onto the still wet sensor and pressed down with a brush. The THF evaporates through the filter,

leaving a thin hydrogel layer between the membrane filter and the boPET foil (see Figure 7f for sensor cross section).

Table 2: Composition of different sensor cocktails (5%), all dissolved in THF (95%) (RP: reference particles)

Sensor	Host material	FRET-System [% (v/v)]	Indicator [mmol/kg polymer]
A	CA	C545T & MFR [2 / 0.25]	BPB [6]
B	D7	C545T & MFR [2 / 0.25]	BPB [6]
C	D4	C545T & MFR [2 / 0.25]	BPB [6]
D	D1	C545T & MFR [2 / 0.25]	BPB [6]
E	D7 & RP [80:20]	C545T & MFR [0.4 / 0.2]	BPB [6]
F	D7	C30 & MFR [2 / 0.2]	BPB [20]

Buffer preparation

100 mM phosphate buffers (pH 7.2) containing different ammonia concentrations were prepared by dissolving sodium dihydrogen phosphate and disodium hydrogen phosphate in water[41]. An equivalent amount of ammonium chloride was dissolved in each buffer, resulting in a free ammonia (pK_a 9.25) concentration calculated by the Henderson-Hasselbach equation (see equation 10).

$$pH = pK_a + \log_{10}\frac{c[\mathrm{NH_3}]}{c[\mathrm{NH_4^+}]} \quad (10)$$

The temperature dependency of the ammonia-ammonium equilibrium was calculated by the Gibbs free energy (see equation 11)

$$\Delta G = R \cdot T \cdot \ln K \quad (11)$$

The mathematical compensation of pK_a of ammonia towards salinity was based on a recently published study by Bell et. al.[36].

Instrumentation and measurement

Absorbance spectra were recorded with a Varian Cary 50 UV-VIS spectrophotometer. Luminescence spectra were recorded using a Hitachi F-7000 fluorescence spectrometer. Intensity based and DLR-referenced sensor measurements were carried out with a pH-1 mini (PreSens, Germany). Two wavelength ratiometric measurements were carried out on a SR830 lock-in amplifier from Stanford Research Systems, Inc. (Sunnyvale, CA, United States), a 405 nm LED from Roithner Lasertechnik (Vienna, Austria) combined with two Hamamatsu photomultiplier tubes and two band pass filters (Carl Zeiss 575-625 (575 nm to 625 nm) and Horiba Scientific XF 1072 (460 nm to 490 nm)). Fluorescence imaging was carried out with an F-201C camera from Allied Vision Technologies (Stadtroda, Deutschland). A homemade flow-through cell was used at all intensity based response and calibration measurements. A series of plastic heads (to be plugged on the optical fibers of each readout system) with glued on sensor spots were used for longtime batch measurements. Figure 7 gives an overview over all sensor and instrumentation setups.

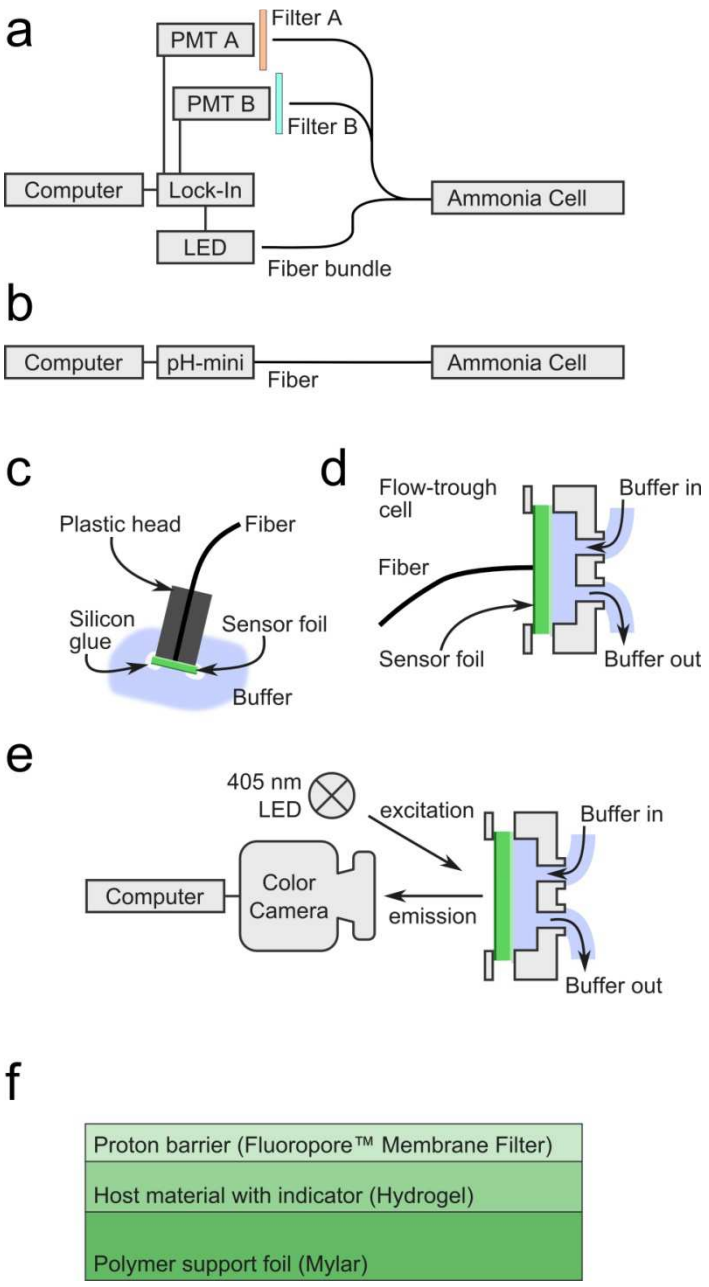

Figure 7: Schemes of measurement setups, instrumentation setups and sensor cross section.
Homemade two filter read-out approach (a) for ratiometric measurements and pH-mini setup (b) for intensity based measurements. Plastic head sensor setup (c) for longtime measurements of multiple sensor spots, homemade flow-through cell (d) for all intensity based measurements and imaging setup (e) for chemical imaging. Schematic cross-section of the sensor foil (f). Sizes are not to scale.

Conclusion

An optical ammonia sensor was developed from commercially available products with simple means of manufacturing. The sensor exhibits a high sensitivity down to almost 1 µg/l ammonia, a response quicker than 120 seconds and virtually no cross sensitivity towards pH, temperature and salinity. Two different referencing methods have been presented to demonstrate a simple usability and possible application to imaging technologies.

Abbreviations

BPB: Bromophenol blue; C30: Coumarin 30; C545T: Coumarin 545T; CA: cellulose acetate; DLR: dual lifetime referencing; FRET: Förster resonance energy transfer; MFR: Macrolex Fluorescent Red G; TWR: two wavelength ratiometric

Competing interests

The authors declare that they have no competing interests

Authors' contribution

TA planned and carried out the sensor manufacturing, measurements and data evaluation. BU assisted during imaging measurements and data evaluation of said measurements. IK provided scientific advices. TM headed the scientific planning and evaluation of the project. All authors have read and approved the final version.

Authors' information

All authors are working at the Institute of Analytical Chemistry and Food Chemistry, Graz University of Technology, Stremayrgasse 9, 8010 Graz, Austria.

Acknowledgement

Financial support by the Austrian Research Promotion Agency (FFG) in the framework of the Austrian Nano Initiative (Research Cluster 0700–ISOTEC) is gratefully acknowledged. We acknowledge Jan Fischer for drawing attention to the publication of Bell et al.

[1] Mathews CK, Holde KEV: *Biochemistry*. 2 Sub. Benjamin-Cummings Pub Co; 1995.

[2] Strömberg N, Hakonen A: **Plasmophore sensitized imaging of ammonia release from biological tissues using optodes**. *Analytica Chimica Acta* 2011, **704**:139–145.

[3] Crowley K, Pacquit A, Hayes J, Lau KT, Diamond D: **A gas-phase colorimetric sensor for the detection of amine spoilage products in packaged fish**. In *2005 IEEE Sensors*. 2005:4 pp.

[4] Lee DS, Atkins DHF: **Atmospheric ammonia emissions from agricultural waste combustion**. *Geophys. Res. Lett.* 1994, **21**:281–284.

[5] N[otilde]mmik H, Nilsson K-O: **Nitrification and Movement of Anhydrous Ammonia in Soil**. *Acta Agriculturae Scandinavica* 1963, **13**:205–219.

[6] Ling Ling T, Ahmad M, Yook Heng L: **An amperometric biosensor based on alanine dehydrogenase for the determination of low level of ammonium ion in water**. *Journal of Sensors* 2011, **2011**.

[7] Li QP, Zhang J-Z, Millero FJ, Hansell DA: **Continuous colorimetric determination of trace ammonium in seawater with a long-path liquid waveguide capillary cell**. *Marine Chemistry* 2005, **96**:73–85.

[8] Müller T, Walter B, Wirtz A, Burkovski A: **Ammonium Toxicity in Bacteria**. *Current Microbiology* 2006, **52**:400–406.

[9] Felipo V, Butterworth RF: **Neurobiology of ammonia**. *Progress in Neurobiology* 2002, **67**:259–279.

[10] Timmer B, Olthuis W, Berg A van den: **Ammonia sensors and their applications--a review**. *Sensors and Actuators B: Chemical* 2005, **107**:666–677.

[11] Randall D., Tsui TK.: **Ammonia toxicity in fish**. *Marine Pollution Bulletin* 2002, **45**:17–23.

[12] Krug FJ, Růžička J, Hansen EH: **Determination of ammonia in low concentrations with Nessler's reagent by flow injection analysis**. *The Analyst* 1979, **104**:47.

[13] Meyerhoff ME, Fraticelli YM, Greenberg JA: **Polymer-membrane electrode-based potentiometric sensing of ammonia and carbon dioxide in physiological fluids**. *Clinical Chemistry* 1982, **28**:1973–1978.

[14] Claps R, Englich FV, Leleux DP, Richter D, Tittel FK, Curl RF: **Ammonia Detection by use of Near-Infrared Diode-Laser-Based Overtone Spectroscopy**. *Appl. Opt.* 2001, **40**:4387–4394.

[15] Crowley K, Morrin A, Hernandez A, O'Malley E, Whitten PG, Wallace GG, Smyth MR, Killard AJ: **Fabrication of an ammonia gas sensor using inkjet-printed polyaniline nanoparticles**. *Talanta* 2008, **77**:710–717.

[16] Daridon A, Sequeira M, Pennarun-Thomas G, Dirac H, Krog JP, Gravesen P, Lichtenberg J, Diamond D, Verpoorte E, de Rooij NF: **Chemical sensing using an integrated microfluidic system based on the Berthelot reaction**. *Sensors and Actuators B: Chemical* 2001, **76**:235–243.

[17] Courbat J, Briand D, Wöllenstein J, de Rooij NF: **Polymeric foil optical waveguide with inkjet printed gas sensitive film for colorimetric sensing**. *Sensors and Actuators B: Chemical* 2011, **160**:910–915.

[18] Mills A, Wild L, Chang Q: **Plastic colorimetric film sensors for gaseous ammonia**. *Mikrochimica Acta* 1995, **121**:225–236.

[19] Preininger C, Mohr GJ, Klimant I, Wolfbeis OS: **Ammonia fluorosensors based on reversible lactonization of polymer-entrapped rhodamine dyes, and the effects of plasticizers**. *Analytica Chimica Acta* 1996, **334**:113–123.

[20] Förster T: **Zwischenmolekulare Energiewanderung und Fluoreszenz**. *Annalen der Physik* 1948, **437**:55–75.

[21] Larsen M, Borisov SM, Grunwald B, Klimant I, Glud RN: **A simple and inexpensive high resolution color ratiometric planar optode imaging approach: application to oxygen and pH sensing**. *Limnology and Oceanography: Methods* 2011, **9**:348–360.

[22] Waich K, Borisov S, Mayr T, Klimant I: **Dual lifetime referenced trace ammonia sensors**. *Sensors and Actuators B: Chemical* 2009, **139**:132–138.

[23] Waich K, Mayr T, Klimant I: **Fluorescence sensors for trace monitoring of dissolved ammonia**. *Talanta* 2008, **77**:66–72.

[24] Waich K, Mayr T, Klimant I: **Microsensors for detection of ammonia at ppb-concentration levels**. *Measurement Science and Technology* 2007, **18**:3195–3201.

[25] Malins C, Butler TM, MacCraith BD: **Influence of the surface polarity of dye-doped sol-gel glass films on optical ammonia sensor response**. *Thin Solid Films* 2000, **368**:105–110.

[26] Trinkel M, Trettnak W, Reininger F, Benes R, O'Leary P, Wolfbeis OS: **Study of the performance of an optochemical sensor for ammonia**. *Analytica Chimica Acta* 1996, **320**:235–243.

[27] Chang Q, Sipior J, Lakowicz JR, Rao G: **A Lifetime-Based Fluorescence Resonance Energy Transfer Sensor for Ammonia**. *Analytical Biochemistry* 1995, **232**:92–97.

[28] Klein R, Voges E: **Integrated-optic ammonia sensor**. *Sensors and Actuators B: Chemical* 1993, **11**:221–225.

[29] Mayr T, Borisov SM, Abel T, Enko B, Waich K, Mistlberger G, Klimant I: **Light Harvesting as a Simple and Versatile Way to Enhance Brightness of Luminescent Sensors**. *Analytical Chemistry* 2009, **81**:6541–6545.

[30] www.advbiomaterials.com/products/hydrophilic/HydroMed.pdf

[31] Preininger C, Mohr GJ: **Fluorosensors for ammonia using rhodamines immobilized in plasticized poly(vinyl chloride) and in sol-gel; a comparative study**. *Analytica Chimica Acta* 1997, **342**:207–213.

[32] Arnold MA, Ostler TJ: **Fiber optic ammonia gas sensing probe**. *Anal. Chem.* 1986, **58**:1137–1140.

[33] http://www.millipore.com/catalogue/item/fhup04700

[34] Whelan A, Regan F: **Antifouling strategies for marine and riverine sensors**. *Journal of Environmental Monitoring* 2006, **8**:880.

[35] Waich K, Sandholzer M, Mayr T, Slugovc C, Klimant I: **A highly flexible polymerization technique to prepare fluorescent nanospheres for trace ammonia detection**. *Journal of Nanoparticle Research* 2010, **12**:1095–1100.

[36] Bell TG, Johnson MT, Jickells TD, Liss PS: **Ammonia/ammonium dissociation coefficient in seawater: A significant numerical correction**. *Environ. Chem.* 2007, **4**:183–186.

[37] Klimant I, Huber C, Liebsch G, Wolfbeis OS: **Dual Lifetime Referencing (DLR) - A New Scheme for Converting Fluorescence Intensity into a Frequency-Domain or Time-Domain Information**. In *New Trends in Fluorescence Spectroscopy: Applications to Chemical and Life Sciences*. 1st edition. Springer; 2001:257–274.

[38] Schäferling M: **The Art of Fluorescence Imaging with Chemical Sensors**. *Angewandte Chemie International Edition* 2012, **51**:3532–3554.

[39] Castellano FN, Lakowicz JR: **A Water-Soluble Luminescence Oxygen Sensor**. *Photochemistry and Photobiology* 1998, **67**:179–183.

[40] Karmakar B, De G, Ganguli D: **Dense silica microspheres from organic and inorganic acid hydrolysis of TEOS**. *Journal of Non-Crystalline Solids* 2000, **272**:119–126.

[41] Beynon PR, Easterby J: *Buffer Solutions*. Taylor & Francis; 1996.

DLR-referenced ammonia sensor for cell metabolism monitoring in bioreactors

Introduction

Ammonia is formed in nature by a variety of processes; the main source is the degradation of proteins[1]. Due to the inherent toxicity towards organisms[2], the ammonia concentration in the environment is very important. In biotechnology, the monitoring of ammonia in bioreactors can't be neglected. Thus, reliable, cheap and user friendly means for that are desired. Optical sensors for ammonia have been successfully employed in many different scientific and industrial branches for monitoring and measurement applications[3] and are a promising tool in the search for ammonia monitoring devices.

A company requested in 2009 an optical ammonia sensor for the monitoring of Chinese hamster ovary cells (CHO cells) in bioreactors[4]. Ammonia is toxic towards CHO cells[5,6,7] but the production of ammonia can be controlled by modifying their growth medium[8]. The requirements of the sensor were as follows

- **Concentration range:** The desired concentration rage was 0.3 to 30 mM total ammonia concenctration (TAC). TAC is the sum of dissolved ammonia and ammonium within the growth medium.
- **Temperature range:** The first description of the temperature range was 20 to 40°C. Afterwards the temperature range was narrowed down to 35 to 39 °C.
- **Operating pH range:** Since the ammonia-ammonium equilibrium is pH dependent, the exact knowledge of the pH value is very important during the measurement. The desired operating pH range was between 6 and 8, with normal use at pH of about 7.
- **Spectral properties:** The sensor should be used with a pH-mini 1 unit built by PreSens. The excitation wavelength is bound by its LED to 470 nm and the emission wavelength is determined by it long pass filter to 550 nm or more.
- **Referencing:** The sensor should be referenced, preferably by DLR referencing because the pH-mini for that.
- **Sterilization:** The sensor must be gamma sterilizable, due to its planned packaging and product application.

- **Response time:** The response time t_{90} should be 10 minutes. Faster response times are not necessary, since the metabolism of Chinese hamster ovary cells is the time limiting factor of changes in ammonia concentration.

The basis for this development is founded on the work by Waich et al.[9,10,11,12]. The main tasks, which have to be dealt with during the development, were the evaluation of a suitable proton barrier and manufacturing process to gain an adequate response time and sensor lifetime. This chapter deals with the efforts and the results regarding these two tasks.

Experimental

Materials

Tetraethoxysilane (TEOS) and celluloseacetate (CA) were obtained from Acros Organics (Geel, Belgium). Tetrahydrofuran (THF), sodium dihydrogen phosphate and disodium hydrogen phosphate were bought from Carl Roth GmbH (Karlruhe, Germany). Hydrogel D7 was obtained from CardioTech International Inc. (Wilmington, MA, United States). Millipore FHUP Fluoropore™ Membrane Filters were bought from EMD Millipore Corporation (Billerica, MA, United States). ($Ru[dpp(SO_3Na)_2]_3)Cl_2$), Oregon Green 488 (2',7'-difluoro-3',6'-dihydroxy-Spiro[isobenzofuran-1(3H),9'-[9H]xanthen]-3-one) and lipophilized Oregon Green 488 (1-[[(2',7'-difluoro-3',6'-dihydroxy-3-oxospiro[isobenzofuran-1(3H),9'-[9H]xanthen]-5-yl)carbonyl]amino]-stearin) was synthesized in lab following to published results[13]. The experimental Superphobic PES 0.2µ and Superphobic UHP 0.2µ membranes were a project contribution EMD Millipore Corporation (Billerica, MA, United States) from and not commercially available during their use in the project. The two-component silicone (Gelest RG™ 01 2-part Reprographic Silicone Elastomer PP2-RG01), all parts of the four-component silicone ((25-35% Methylhydrosiloxane)-dimethylsiloxane copolymer, Polydimethylsiloxane (vinyldimethylsiloxy terminated), Platinum(0)-1,3-divinyl-1,1,3,3-tetramethyldisiloxane, and 1,3,5,7-Tetravinyl-1,3,5,7-tetramethylcyclotetrasiloxane) and FC-75 (2,2,3,3,4,4,5-heptafluoro-5-(1,1,2,2,3,3,4,4,4-nonafluorobutyl)tetrahydrofuran) were ordered from ABCR (ABCR Dr. Braunagel GmbH & Co. KG, Karlsruhe, Germany). Teflon AF (Polytetrafluoroethylene-co-2,2-bis(trifluoromethyl)-4,5-difluoro-1,3-dioxole) was purchased from DuPont. ELASTOSIL® E4 silicone rubber was purchased from WACKER (Wacker Chemie AG, Stuttgart, Germany). The polymer reference particles provided by PreSens (*Referenzpartikel für DLR; sauerstoffinsensitiv, Ruthenium basiert;* Art. Nr. 200001159).

Synthesis of reference particles

The reference particles were prepared analogically as reported before[14]. The synthesis is described in detail in the experimental section of the chapter ”*Fast responsive, optical trace level ammonia sensor for environmental monitoring*“(see page 81).

Sensor manufacturing

The sensor layer was manufactured by spreading a sensor cocktail onto a boPET foil with a knife-coating apparatus. Depending on the type of proton barrier, the manufacture process was either a subsequent, identical knife-coating step (for silicone or Teflon AF based barriers) or a manual attachment of a piece of membrane onto the wet cocktail. Detailed instructions can be found in the chapter "*Fast responsive, optical trace level ammonia sensor for environmental monitoring*"(see page 81).

Results and discussion

Sensor design and setup

The sensor consists of a polymer containing a pH indicator and a referencing dye, enclosed between a support, and an ammonia permeable, proton impermeable membrane. The setup and the sensing mechanism have been described in the previous chapter "*Fast responsive, optical trace level ammonia sensor for environmental monitoring*" (see page 70 for setup and sensing mechanism, see page 76 for DLR referencing) in detail.

Manufacturing process

The manufacturing process of the sensor was not altered during the whole project. The procedure was based knife-coating the dried host polymer of the indicator onto a sensor support. The subsequent step of manufacturing the proton barrier differed in dependency of the used barrier materials: In case of silicone another knife-coating step on top of the dried host polymer was carried out, in case of membranes the membrane foil were put or laid onto the wet sensor cocktail.

An attempt was made to spray-coat the sensor cocktail onto used barrier membranes (FHUP and PES). No composition of the sensor cocktails could be found, which would produce a homogeneous layer on top of the membrane (varying cocktail concentrations and solvents volatileness (THF or 1,4-dioxane)).

Indicator dye

Two different pH indicators have been used. In earlier stages of the project, 2'-7'-difluoro-fluorescein (Oregon Green 488 or OG488) was used as an indicator. OG488 has a pK_a of 4.7[15], which covers ideally the ammonia concentration which should be monitored. Due to the not inconsiderable solubility in water, a lipophilized derivate of OG488 was used in later stages of the project, OG488StA. This lipophilization was carried out by an addition of a stearyl amide to the phenyl part of OG488. Structures can be found in Figure 35. The lipophilized indicator showed the same sensitivity towards ammonia, but a significantly lower solubility in water.

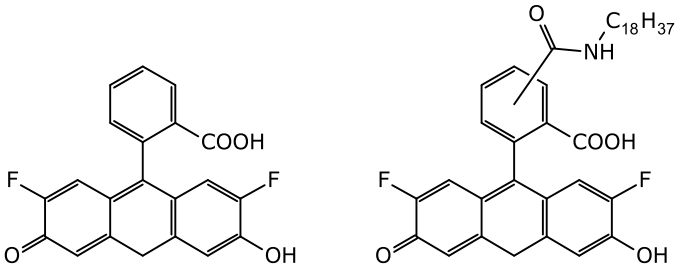

Figure 35: Molecular structure of OG488 (left) and OG488StA (right)

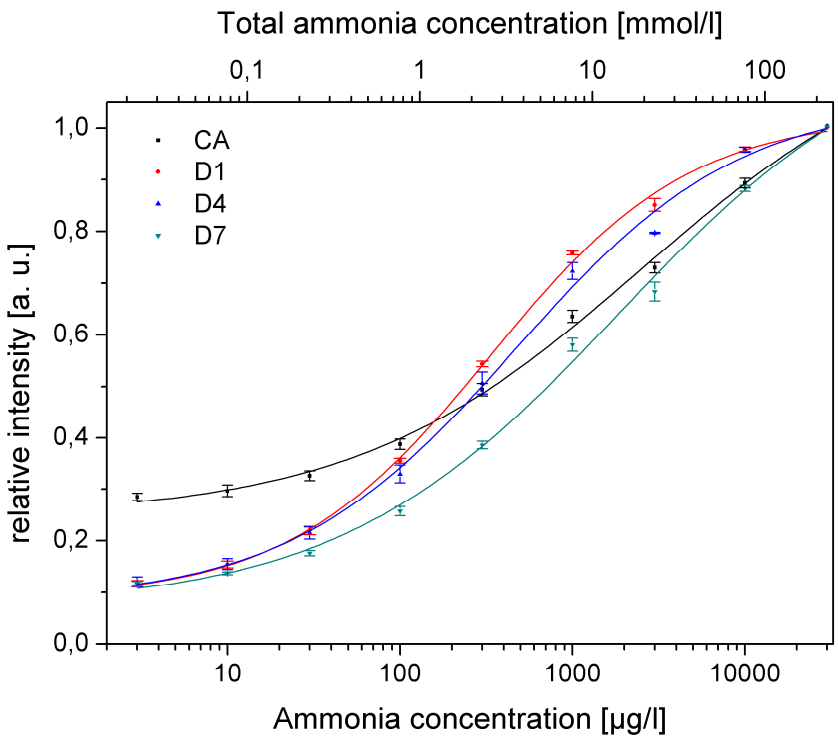

Figure 36: Comparison of measurement range between ammonia sensors made of different polymers (Sensing layer: 5% polymer with 10 mmol OG488StA per kilogram polymer in THF; Proton Barrier: FHUP Teflon filter; measurement setup: flow-through cell; pH: 7.2; temperature: 23°C; buffer: 100 mM phosphate buffer).

Proton barrier

Different materials for the use as proton barriers have been evaluated. While almost all of them did work, each material had specific drawbacks.

The drawback all silicon based proton barrier materials and TAF had in common was their translucent or clear look. Unlike white, light scattering membranes, only a fraction of the luminescence from the host polymer was scattered back and coupled into the read-out unit's fiber. This issue was be circumvented by adding TiO_2 particles into the hexane-silicone solution to increase the amount of backscattered light. In all cases Kemira 660 particles were used. Different amounts of particles were tested, indicating that an particle-silicone ratio of 20+80 or 40+60 (for 50% or 35% solutions in THF respectively, with a wet coating thickness of 25.4 µm) results in measured amplitudes almost comparable to sensor foils employing membranes.

Table 3: Used proton barrier materials and manufacturing steps

Name	Type	Manifacturing
PP2-RG 01	2-component silicone	knife coating of 10+1 mixture in 75 to 90% hexane
4C Silicon	4-component silicone	knife coating of 50/50/1/1 mixture in 75 to 90% hexane
TAF	DuPont Teflon AF	knife coating of 5 or 10% in FC75 (perfluorated solvent)
FHUP	Millipore Fluoropore™ Membrane	deposition on top of wet sensor cocktail
Superphobic PES 0.2µ	Experimental PES membrane	deposition on top of wet sensor cocktail
Superphobic UHP 0.2µ	Experimental membrane	deposition on top of wet sensor cocktail
E4	1-component silicone	knife coating of 20 to 50% silicone in hexane

Although the Millipore Fluoropore™ FHUP membrane filters showed extraordinary t_{90} response times (faster than 10 seconds), their application in the final sensor was foreclosed due to the fact, that FHUP filters become brittle and leaky during gamma sterilization.[16] Millipore provided two alternative solutions to the idea using membranes as

a proton barrier: two experimental and at this moment not commercially available membranes, called Superphobic PES 0.2µ and Superphobic UHP 0.2µ. Former membrane proved itself to be a good alternative to FHUP, while latter membrane did not show any ammonia permeability at all.

Referencing dye and particle

A Ruthenium (II)-complex (Tris(4,4-diphenyl-2,2-bipyridine)ruthenium(II)) was used as reference dye. This dye is also employed in the commercially available products designed for the pH-mini. Since this complex is oxygen-sensitive, it was entrapped in gas-impermeable particles. Two different types of particles have been used. The polymer particles (PPar), used in the early stage of the project, were provided by PreSens (*Referenzpartikel für DLR; sauerstoffinsensitiv, Ruthenium basiert;* Art. Nr. 200001159). The second type, which was used, was based on silica and a water soluble derivative of said Ruthenium complex (SPar). Both particle types showed the same phase shift, the former one displayed slightly lower brightness. Still, the second type of particles was favorably used, since the silica particles are insoluble in any organic solvent used and the specific polymer of the first type was not known.

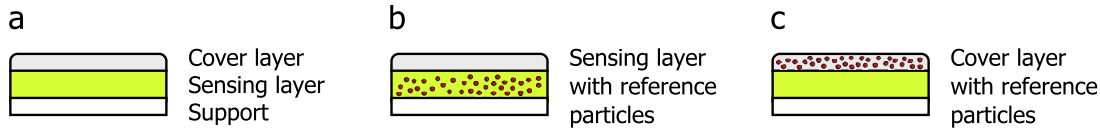

Figure 37: Basic sensor setups. Non-referenced sensor (a) and referenced sensor with sensor dye entrapped in either sensing layer (b) or cover layer (c). (Sizes are not to scale)

Three different basic sensor setups have been employed. To evaluate the sensitivity of a specific sensor composition a non-referenced sensor setup was used (see Figure 37a). Two referenced sensor setups were designed (see Figure 37b and c). The predominantly applied sensor design had reference particles in the host polymer or sensing layer. The design employing reference particles in the cover layer had been used in early stages of the project, since migration processes of the indicator dye into the then used polymer based reference particles were not known and could be avoided with this design. The drawbacks of this design was a higher deviation in phase shift calibration due to the fact, that not only the dye and particle contents but also the thickness of both sensing and cover layer were decisive factors of the calibration values.

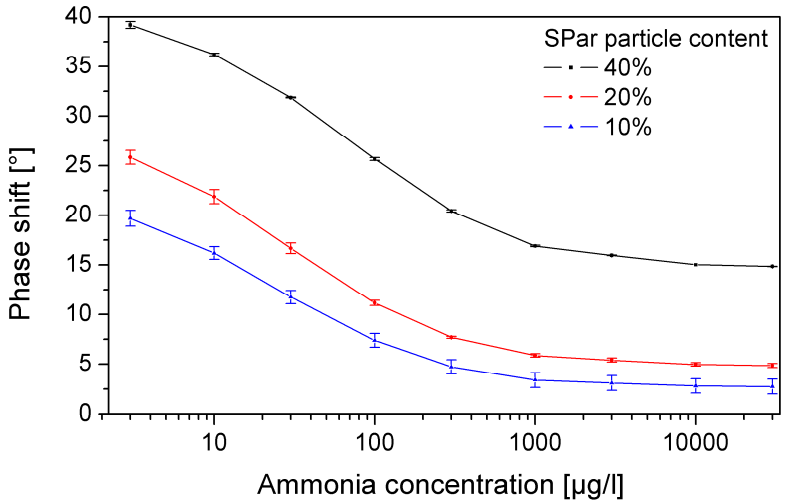

Figure 38: Phase shift calibration of different ammonia sensors (Sensing layer: 5% D1+SPar in deviating ratios with 10 mmol OG488StA per kilogram polymer in THF; Proton Barrier: FHUP Teflon filter; measurement setup: flow-through cell; pH: 7.2; temperature: 23°C; buffer: 100 mM phosphate buffer).

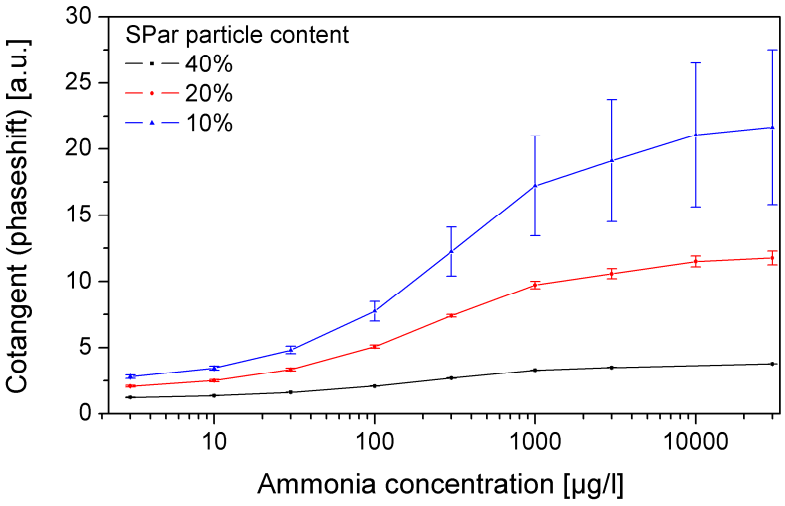

Figure 39: Cotangent values of the phase shift calibration (Sensing layer: 5% D1+SPar in deviating ratios with 10 mmol OG488StA per kilogram polymer in THF; Proton Barrier: FHUP Teflon filter; measurement setup: flow-through cell; pH: 7.2; temperature: 23°C; buffer: 100 mM phosphate buffer).

Measurement setup and sensor response

Over the course of the whole sensor development three main measurement setups have been used (see Figure 40). The first measurement setup was based on a home-made plastic head consisting of two parts. A cut out part of the sensor foil was fixed inside the head by screwing both parts together and sealed by a silicone rubber gasket (see Figure 40a). The main problem, which occurred with this sensor setup, was buffer mixing. Since the opening in the outer part of the plastic head was only 1.5 mm in diameter and about 3 to 4 mm deep, the mixing of buffer solutions in this area was diffusion-controlled which resulted in very long response times in the range of hours (see Figure 41). The problem was identified by comparing the response times of the sensor towards dissolved ammonia in a buffer and towards ammonia in a headspace. The t_{90} time of response towards ammonia in air was considerably faster (20 to 30 minutes, 4-component silicon proton barrier) than towards ammonia dissolved in buffer (3.5 hours and more, 4-component silicon proton barrier). Additionally, the response time t_{90} of the identical sensor layer in flow-through cells (see Figure 40) was in the area of 10 to 30 minutes, depending on the thickness of the 4-component silicon proton barrier.

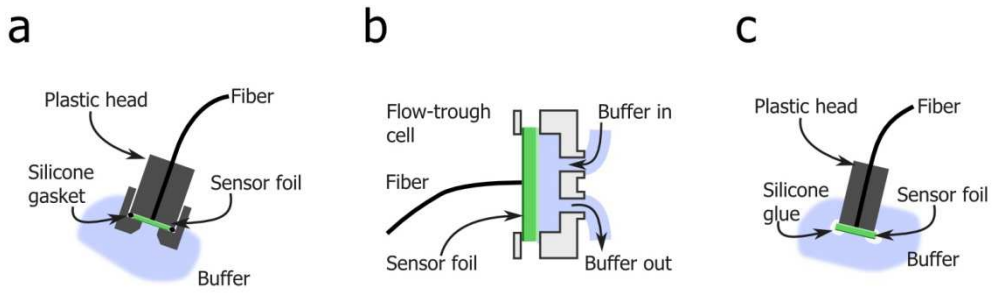

Figure 40: Measurement setup used for the ammonia sensor development: Plastic two-part sensor head with gasket and sensor inlay (a), flow-through cell (b) and basic one-part plastic sensor head with silicone sealing and glued on sensor patch (c). (Sizes are not to scale)

The sensor setup employing a flow-through cell ensured no temperature stability. As seen in Figure 45, the sensor fails at 34°C. The source of the problem was determined to be creeping of the sensing layer's polymer (D7) at elevated temperatures, which was facilitated by the pulsation of the peristaltic pump used together with the flow-through cell.

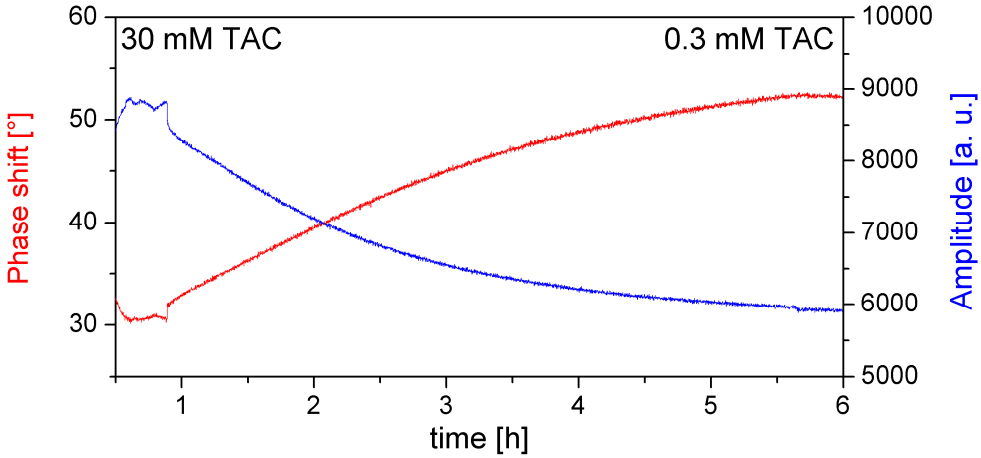

Figure 41: Phase shift (red) and amplitude (blue) values of a sensor patch mounted in the plastic two-part head sensor setup (Sensing layer: 5% D7+PPar (70+30) with 10 mmol OG488 per kilogram polymer in THF; Proton Barrier: 33% of 4-component silicone in hexane; measurement setup: two-part plastic head; pH: 7; temperature: 23°C; buffer: 100 mM phosphate buffer).

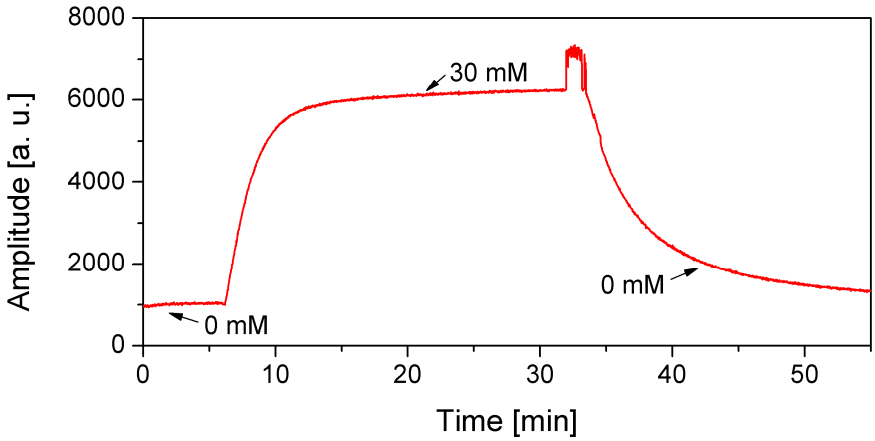

Figure 42: Sensor response of an ammonia sensor with a silicone proton barrier between two pH 7 phosphate buffers with 0 or 30 mmol/l TAC in a flow-through cell (Sensing layer: 5% D7 with 10 mmol OG488 per kilogram polymer in THF; Proton Barrier: 25% of 4-component silicone in hexane; measurement setup: flow-through cell; pH: 7; temperature: 23°C; buffer: 100 mM phosphate buffer).

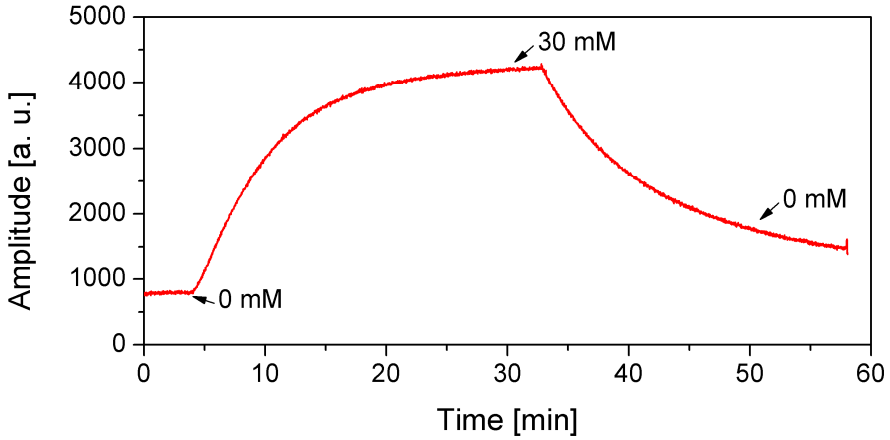

Figure 43: Sensor response of an ammonia sensor with a Teflon AF barrier between two pH 7 phosphate buffers with 0 or 30 mmol/l TAC in a flow-through cell (Sensing layer: 5% D7 with 10 mmol OG488 per kilogram polymer in THF; Proton Barrier: 5% Teflon AF in FC75; measurement setup: flow-through cell; pH: 7.2; temperature: 23°C; buffer: 100 mM phosphate buffer).

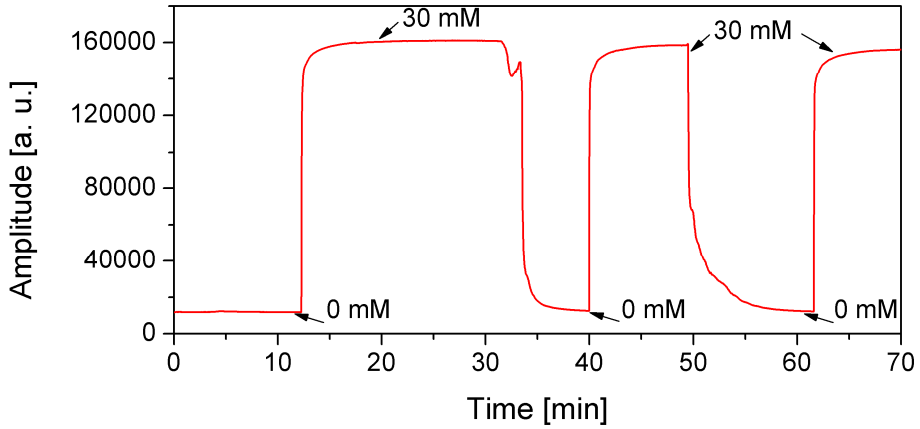

Figure 44: Sensor response of an ammonia sensor with a FHUP membrane proton barrier between two pH 7 phosphate buffers with 0 or 30 mmol/l TAC in a flow-through cell (Sensing layer: 5% D7 with 10 mmol OG488 per kilogram polymer; Proton Barrier: Millipore Fluoropore FHUP membrane filter; measurement setup: flow-through cell; pH: 7.2; temperature: 23°C; buffer: 100 mM phosphate buffer).

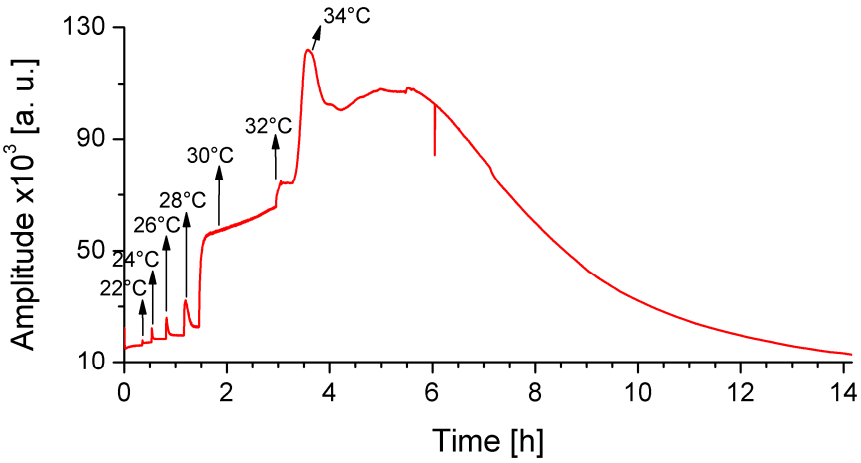

Figure 45: Temperature stability issues of an ammonia sensor measured in a flow-through cell with a peristaltic pump (Sensing layer: 5% D7 with 10 mmol OG488 per kilogram polymer in THF; Proton Barrier: Millipore Fluoropore FHUP membrane filter; measurement setup: flow-through cell; pH: 7; buffer: 100 mM phosphate buffer).

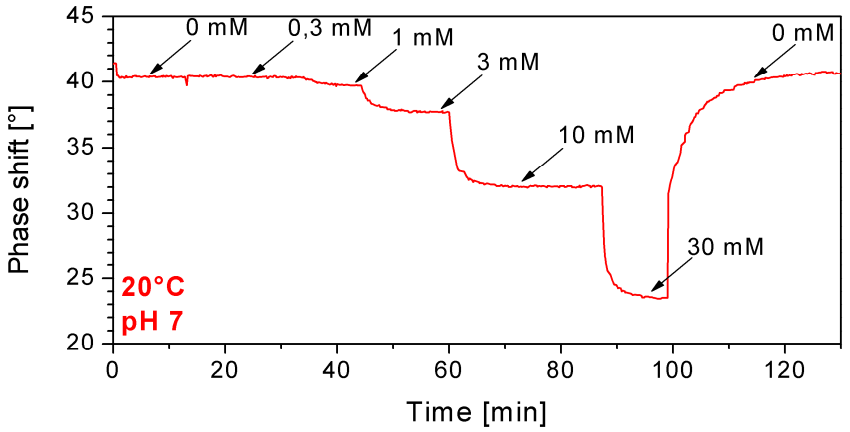

Figure 46: Sensor response of an ammonia sensor at 20°C employing a PES membrane as proton barrier to phosphate buffer with total ammonia concentrations between 0 and 30 mM. (Sensing layer: 2.5% D7+PPar (75+25) with 10 mmol OG488 per kilogram polymer in 1,4-dioxane; Proton Barrier: PES membrane; measurement setup: one-part plastic head; pH: 7; temperature: 20°C; buffer: 100 mM phosphate buffer).

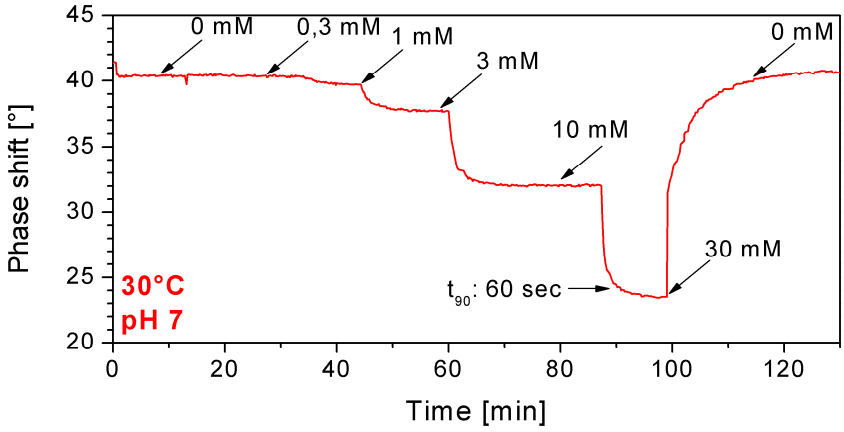

Figure 47: Sensor response of an ammonia sensor at 30°C employing a PES membrane as proton barrier to phosphate buffer with total ammonia concentrations between 0 and 30 mM (Sensing layer: 2.5% D7+PPar (75+25) with 10 mmol OG488 per kilogram polymer in 1,4-dioxane; Proton Barrier: PES membrane; measurement setup: one-part plastic head; pH: 7; temperature: 30°C; buffer: 100 mM phosphate buffer).

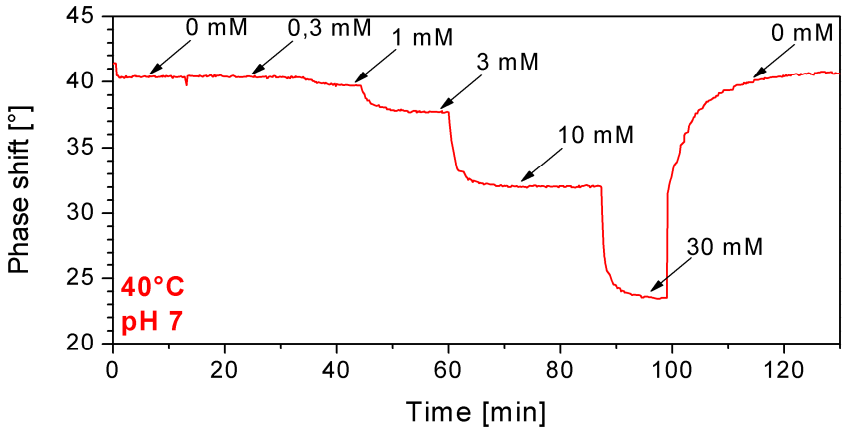

Figure 48: Sensor response of an ammonia sensor at 40°C employing a PES membrane as proton barrier to phosphate buffer with total ammonia concentrations between 0 and 30 mM. (Sensing layer: 2.5% D7+PPar (75+25) with 10 mmol OG488 per kilogram polymer in 1,4-dioxane; Proton Barrier: PES membrane; ; measurement setup: one-part plastic head; pH: 7; temperature: 40°C; buffer: 100 mM phosphate buffer).

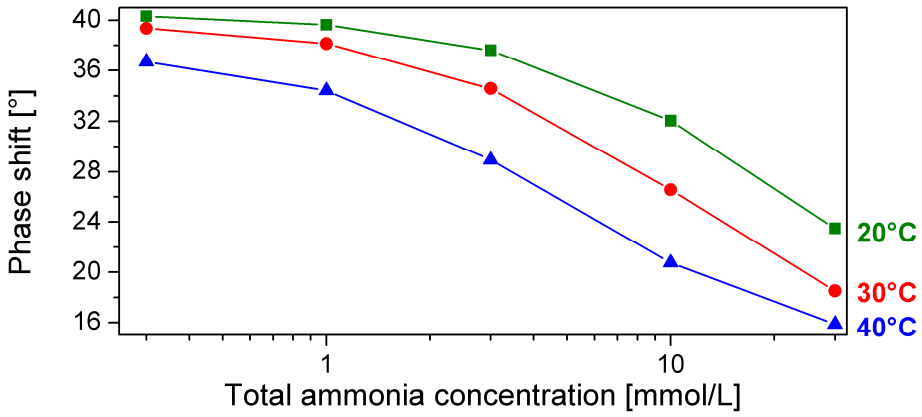

Figure 49: Calibration at different temperatures of an ammonia sensor employing a PES membrane as proton barrier (see Figure 46 to Figure 48).

The sensor response of an ammonia sensor at different temperatures is shown in Figure 46, Figure 47 and Figure 48. The problem of creeping was circumvented by using the third measurement design, a simple and basic, plastic cylinder onto which sensor patches were glued with and sealed by silicone rubber. Figure 49 displays the calibration data and shows that the sensor's sensitivity depends on the temperature. A deeper view into the dependency of the sensor's sensitivity and the ammonia-ammonium equilibrium towards temperature can be found on page 82).

Sensor stability

The sensor stability is a very important issue. Figure 50 depicts a response graph of a referenced ammonia sensor based on SPar reference particles and FHUP membranes. The sensor's stability is obvious over a time period of more than 180 minutes. In the red screen of Figure 50, a response characteristic is shown in detail. According to the sampling frequency of 1 measurement point per second, the t_{90} response time can be calculated to be less than 10 seconds.

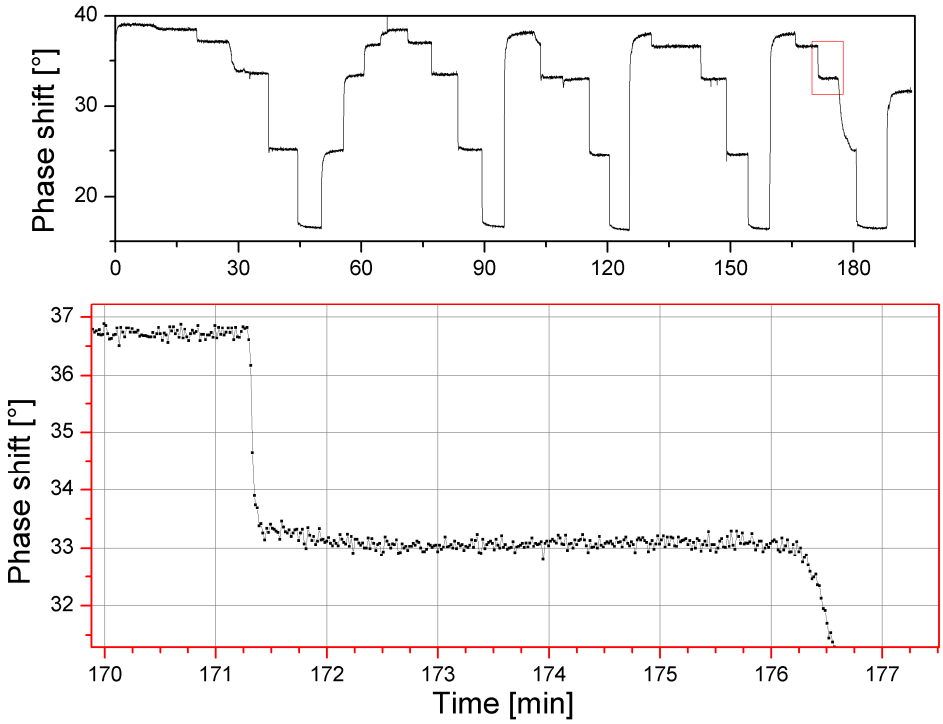

Figure 50: Short-time reversibility of an ammonia sensor, tested in pH 7 phosphate buffer with 0.3, 1, 3, 10 and 30 mM TAC (Sensing layer: 5% D7+SPar (65+35) with 10 mmol OG488 per kilogram polymer; Proton Barrier: FHUP membrane; measurement setup: one-part plastic head; pH: 7; temperature: 23°C; buffer: 100 mM phosphate buffer).

While a stable sensor response over the period of 48 hours or more could not be realized by employing FHUP membrane filters, Figure 51 shows, that over the period of 6 days (144 hours) no changes in sensor calibration were apparent at a buffer temperature of 30°C. Unfortunately, these results couldn't be repeated consistently at 37.2°C although even a specifically lipophilized derivative of Difluorofluorescein was used. From a test with 14 sensor spots, 43% failed within the first 96 hours (no response and measured phase shift at minimum) and 15% showed decreased dynamics in their response. But 43% of the tested sensor spots maintained their characteristic sensor response without critical changes or drifts over the period of 336 hours (14 days). This conspicuously divergence in sensor stability suggests, that the source of the stability problem is not derived from the used materials, the sensor's composition or the measurement setup. It is very likely to be linked to the different coefficients of thermal expansion of membrane and host polymer as well as to the manual manufacturing of the sensor foils, which is error-prone due to is

sequential procedure of coating and putting the membrane on top of the wet, spread cocktail.

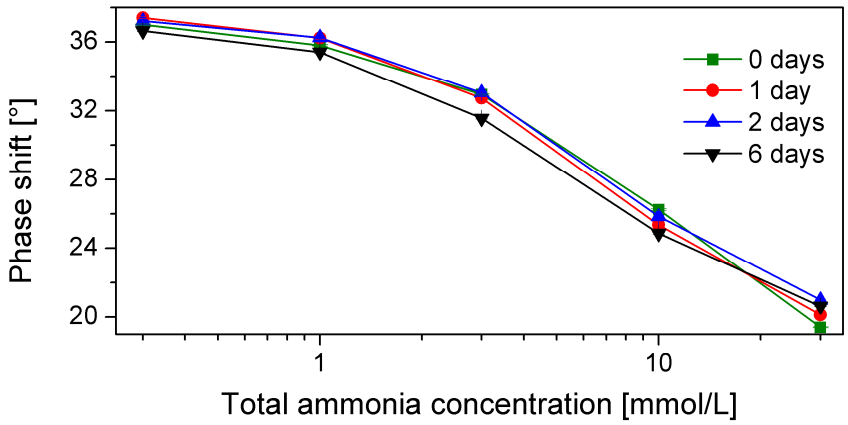

Figure 51: Long-time stability of an ammonia sensor at 30°C and pH 7 (Sensing layer: 2.5% D7+PPar (75+25) with 10 mmol OG488 per kilogram polymer in 1,4-dioxane; Proton Barrier: PES membrane; measurement setup: one-part plastic head).

An almost similar stability was realized with a different sensor composition. A sensing layer consisting of a 90+10 E4/D7 mixture with 10 mmol ES-002L indicator per kg D7 and 20 % (w/w) silica particles dissolved in three parts THF. E4 separates D7 into small domains, which prevents the leakage or migration of the indicator since the indicator is rather soluble in D7 than in E4. The proton barrier was a 50% (w/w) solution of an 80+20 mixture of E4 and Kemira 660 TiO_2 particles. The intensity of the detected luminescence was about 20 000 or 55 000 a.u. (PreSens instrumentation) at total ammonia concentrations of 0.3 or 30 mmol/l respectively. This is a sufficiently high signal. Even though a decrease of phase shift difference between 0.3 and 30 mmol/l can be observed, the sensor maintained still useable after even 19 days in 37.2°C warm phosphate buffer (pH 7.2).

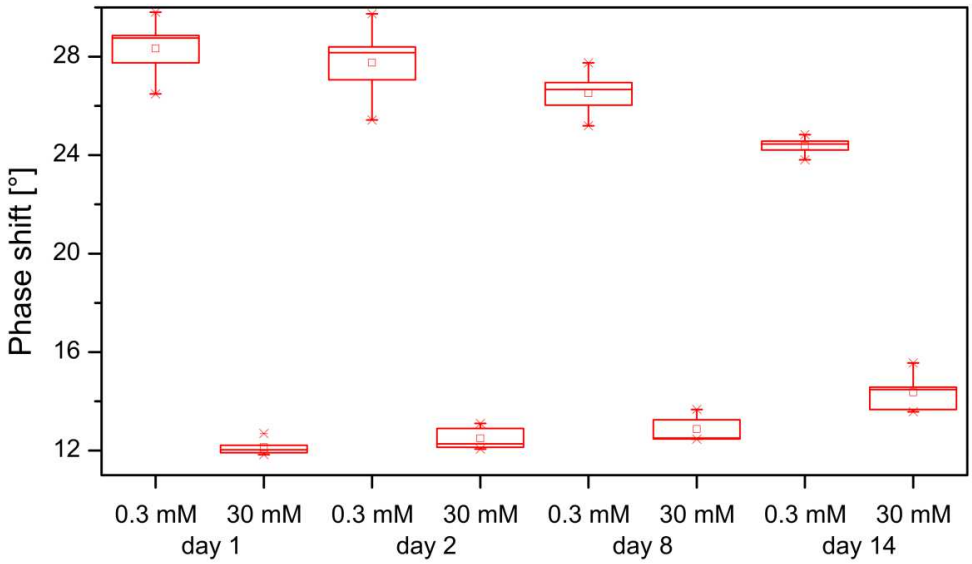

Figure 52: Box plot of the phase shift values of 8 sensor patches at 0.3 and 30 mmol/l TAC being stored in pH 7.2 phosphate buffers at 37.2°C over the period of 14 days (Sensing layer: 25% E4+D7 (9+1) with 10 mmol OG488StA per kilogram D7 and 20% (w/w per D7) SPar in THF; Proton Barrier: 50% solution of E4+Kemira 660 Particles (80+20) in THF; measurement setup: one-part plastic head; pH: 7.2; temperature: 23°C; buffer: 100 mM phosphate buffer).

Conclusion and outlook

Unfortunately it was not possible to develop an ammonia sensor which would meet all criteria. Despite that, many progresses and new insights into the development of such sensors have been made.

It has been found that hydrogels are very sensitive towards ammonia, most likely due to their high water uptake. This makes them most desirable for trace monitoring applications of ammonia.

Difluorofluorescein and a lipophilized derivate were used as indicator and displayed no specific signs of photo bleaching. Still, till the end of the project leaching phenomena could not be excluded definitely from the list of reasons of sensor failure.

Even though silicone based proton barriers have been proven themselves as useful, membranes and membrane filters display an extraordinary fast response characteristic. In case of the Superphobic PES and the FHUP, the hydrophobicity is outstanding. The backside is, that these sensors are not stable over a long period of time, and they show mechanic weakness at elevated temperatures. It is suggested, that a low adhesion between membrane and host polymer is the reason for this behavior.

The last efforts for a long lasting ammonia sensor have been based on a different approach. The host polymer was a heterogenic mixture of E4 silicone (90%) and hydrogel (10%), to separate the hydrogel into individual domains and inhibit leaching of the indicator. The proton barrier was based on E4 silicone with about 25 to 40% of TiO_2 particles for signal enhancing. Tests with OG488StA have not shown the desired stability, but a migration of the lipophilized indicator into the silicone has been considered possible. Further investigations of this approach with OG488 as indicator should be considered in future.

---

[1] M. Schneider, I. W. Marison, U. von Stockar, *Journal of Biotechnology* **1996**, *46*, 161–185.

[2] T. Müller, B. Walter, A. Wirtz, A. Burkovski, *Current Microbiology* **2006**, *52*, 400–406.

[3] B. Timmer, W. Olthuis, A. van den Berg, *Sensors and Actuators B: Chemical* **2005**, *107*, 666–677.

[4] T. Omasa, M. Onitsuka, W.-D. Kim, *Current Pharmaceutical Biotechnology* **2010**, *11*, 233–240.

[5] M. Yang, M. Butler, *Biotechnology and Bioengineering* **2000**, *68*, 370–380.

[6] P. Chen, S. W. Harcum, *Journal of Biotechnology* **2005**, *117*, 277–286.

[7] R. P. Singh, M. Al.-Rubeai, C. D. Gregory, A. N. Emery, *Biotechnology and Bioengineering* **1994**, *44*, 720–726.

[8] W. M. Miller, H. W. Blanch, C. R. Wilke, *Biotechnology and Bioengineering* **1988**, *32*, 947–965.

[9] K. Waich, M. Sandholzer, T. Mayr, C. Slugovc, I. Klimant, *Journal of Nanoparticle Research* **2010**, *12*, 1095–1100.

[10] K. Waich, S. Borisov, T. Mayr, I. Klimant, *Sensors and Actuators B: Chemical* **2009**, *139*, 132–138.

[11] K. Waich, T. Mayr, I. Klimant, *Talanta* **2008**, *77*, 66–72.

[12] K. Waich, T. Mayr, I. Klimant, *Measurement Science and Technology* **2007**, *18*, 3195–3201.

[13] F. N. Castellano, J. R. Lakowicz, *Photochemistry and Photobiology* **1998**, *67*, 179–183.

[14] B. Karmakar, G. De, D. Ganguli, *Journal of Non-Crystalline Solids* **2000**, *272*, 119–126.

[15] https://products.invitrogen.com/ivgn/product/D6145?ICID=search-product (1st of October 2012)

[16] Oral information from Rick Baggio (Millipore, Inc.)

Instrumental control with LabVIEW

LabVIEW (short for „*Lab*oratory *V*irtual *I*nstrumentation *E*ngineering *W*orkbench“) is a proprietary, combined development environment for a visual programming language. National Instruments describes LabVIEW as follows:

> “LabVIEW is powerful system design software built specifically for tasks performed by engineers and scientists. Read the technical papers and case studies in this series to learn why LabVIEW is well positioned to drive the next generation of software development and how a variety of companies have transformed their work by adopting it.”[1].

LabVIEW is a visual programming language, which means that the creation of commands, data analysis or algorithms is designed with graphical elements on an electronic drafting board. Furthermore, LabVIEW is designed as a dataflow orientated programming language, in contrast to event-, aspect-, or component-driven programming languages. The programming paradigm of dataflow orientated programming language focuses on how data is handled, processed and transferred between different programs, subprograms or iterations of themselves.[2]

Programming in LabVIEW happens mainly in two levels: the front panel and block diagram. The front panel displays the graphical user interface (GUI) of the program, and almost exclusively consists of elements used for control or read-out of the program or processed data. The block diagram can be related to the source code of text-based programming languages. It resembles a graphical flowchart, in which the sequence of data handling is marked with wires and different boxes depict different operations.

Figure 53 depicts a simple, self-explaining program, carrying out an addition. The two boxes on the left side are control (input) elements. They display two summands, which can be chosen by the user. The two light grey boxes on the right side illustrate two indicator (output) elements, which – as their name says – indicate values or information processed by the program. The right window is the block diagram. All indicator and control elements from the front panel can be also found in the block diagram. Control elements are normally resembled by an outgoing triangle on their right side, while indicator elements are marked with an ingoing triangle on their left side.

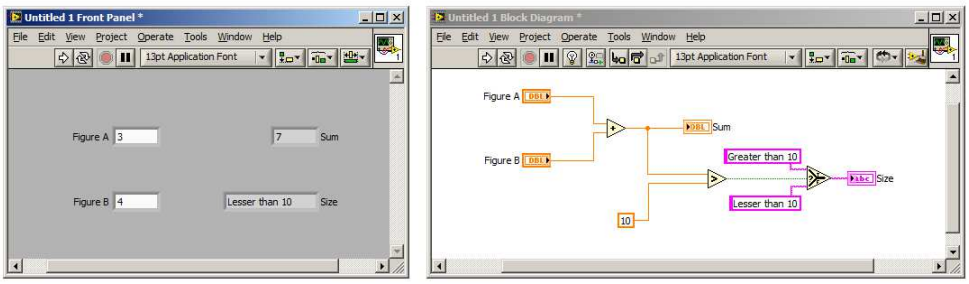

Figure 53: A simple example of a LabVIEW program with front panel (left) and block diagram (right).

Furthermore, additional elements can be found: *Functions*, which process data and *Constants.* The block diagram sums *Figure A* and *Figure B* up and displays it in the indicator *Sum*. Additionally, it compares the sum if the constant is greater than a specific constant, in this case 10. The *Greater as* function passes then a Boolean value (TRUE or FALSE) to a so-called *Select* function, and displays in the *Size* indicator "Greater than 10" or "Lesser than 10" in case of an TRUE or FALSE state of the Boolean value respectively.

LabVIEW is created as a tool for continuous or iterative data handling, acquisition, processing, handling and control[2]. Thus, it is a very appropriate choice for the tasks of creating simple and user friendly programs to access and control measurement instruments, as well as readout, process and save measurement values. LabVIEW was used to access, synchronize or readout the SR830 lock-in amplifier, mass flow controllers from mks or voegtlin and a ThermoHaake thermostat.

---

[1] http://www.ni.com/labview/ (27th of September, 2012)

[2] E. Metin, W. Georgi, *Einführung in LabVIEW*, Carl Hanser Verlag GmbH & CO. KG, **2012**.

SOKRATES – Experimental parameter control, measurement value logging and synchronization within one program

Introduction

The control of the instrumentation and experimental parameters during a sensor characterization test is an essential requirement to gain reliable and reproducible data. Hence, not only the control of each instrument (temperature control, sample unit, measurement device) is important, but also the synchronization of each instrument to plan and carry out the measurement.

A measurement setup consisting of an array of massflow controllers, a lock-in amplifier and a thermostat was built and a program controlling and synchronizing the in- and output of each instrument was installed. The program is capable of storing and loading experimental parameters. Key features are a real-time display of the measurement values and a logging feature saving every parameter of the measurement.

Materials and programs

Mass flow controller

Three digital mass flow controllers (MFC) type 1179B have been purchased (MKS Instruments Deutschland GmbH, Munich, Germany). They each feature a maximum flow rate of 500, 200 and 100 sccm respectively. The MFCs offer a quarter inch Swagelok® fitting, an analog 15-pin type D-Subminiature (DE-15) connector port and a Vitron® or Kalrez® seal materials (Vitron for the 500 and 100 sccm MFCs, and Kalrez for the 200 sccm MFC)[1]. The computer I/O for the MFCs was realized with a National Instruments NI PCI-6703 static analog voltage output PCI card and a shielded National Instruments NI SCB-68 I/O connector block for DAQ devices connected with a National Instruments SH68-68-D1 cable. The PCI card's driver (NI-DAQmx driver, version 8.6.1) was downloaded from the National Instruments homepage. All MFC I/O components have been purchased directly from National Instruments (National Instruments Österreich GmbH, Salzburg-Bergheim, Austria). All used tubes, tee connectors, and valves are made

of stainless steel and are based on one-eighth inch or quarter inch Gyrolok® tubing systems (Burde Co Präzisionsarmaturen GesmbH, Vienna, Austria).

Thermostat

A Thermo Haake DC 50 heating unit with a Thermo Haake K10 cooling bath has been purchased (Thermo Haake GmbH, Karlsruhe, Germany). The computer I/O for the MFCs was realized with a standard analog 9-pin type D-Subminiature (DE-9) cable and a USB-to-RS-232 adapter (Prolific Technology Inc., Taipei, Taiwan).

Lock-In amplifier

A Stanford Research Systems SR830 100 kHz lock-in amplifier was purchased. The computer I/O for the lock-in amplifier was realized with a standard analog 9-pin type D-Subminiature (DE-9) cable.

The lock-in amplifier was connected to a home-made box, consisting of an LED as excitation source and a PMT as detector to use it as a measurement setup for optical sensors. These parts will not be discussed, since they are not controlled by the program.

Programming

The programming was carried out on a PC with Windows 7 Enterprise (6.1.7600) with LabVIEW 2009. The whole system is used on a PC with Windows XP Service Pack 3.

Assembling of instruments

The MFCs have been mounted on a wooden plate and connected with each other using stainless steel tubes. A valve was mounted right after the outlet of each MFC to close non-used controllers during measurement sequences. All MFCs have been wired to a connector block, which then again was connected to the control PCI card in a PC. The lock-in amplifier and the thermostat were connected to the PC with a DE-9 cable via a built-in serial port of the controlling PC, or via an USB-to-DE9 adapter respectively. The adapters of the gas inlets were based on quarter inch Gyrolok® tube systems.

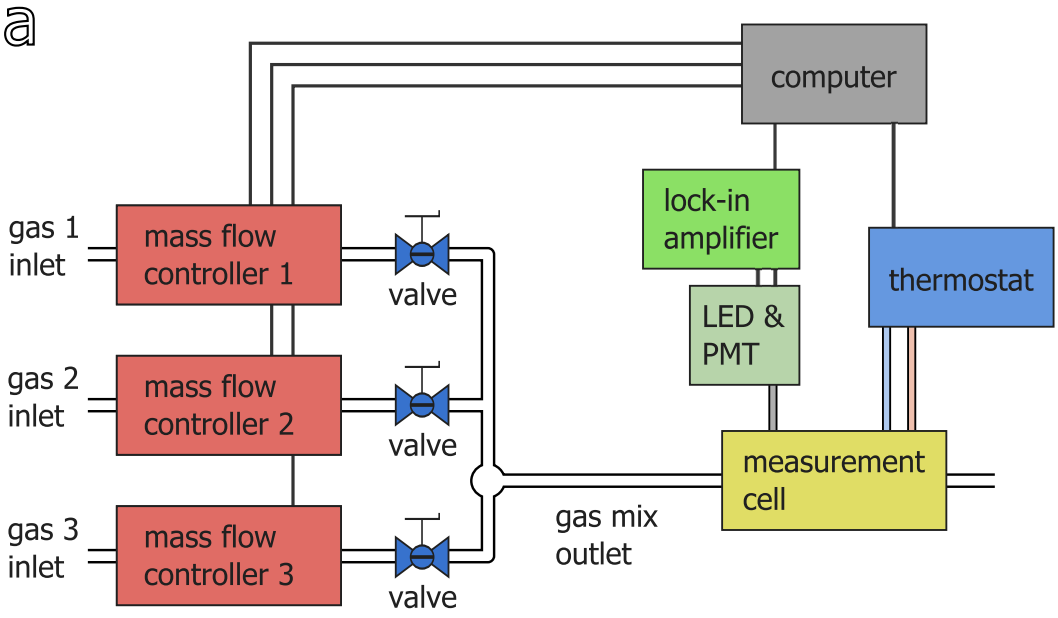

Figure 54: Scheme of the assembled measurement setup.

Front Panel and User Interface

The program interface is based on one window, which is divided into five different tabs. The contents of each tab are the settings for the lock-in amplifier, the settings of the MFCs, the settings of the thermostat, general logging and I/O settings, and display of measurement values.

The first tab (see Figure 55) contains input control elements for the time schedule and instrumental control of the lock-in-amplifier.

The second tab (see Figure 56) is responsible for the control of the mass flow controller. It consists of the main checkbox for the activation or deactivation of the mass flow controller, an input control element for the number of cycles of all gas mixing steps and four arrays, controlling the time schedule and mass flows for an infinite number of gas mixing steps.

The third tab (see Figure 57) contains elements for the control of the thermostat. It consists of the main checkbox the activation or deactivation of the thermostat, four different indicator elements for the display of actual temperatures, processes (heating, cooling or holding temperature) and two arrays for the duration and temperatures for different temperature-control steps.

The fourth tab (see Figure 58) contains elements for the control of the logging function and the communication ports for the lock-in amplifier and the thermostat. It consists of a button to activate the routine to load measurement parameters from other logfiles, an indicator element of the current file path of the logfile, the drop-down lists for the communication ports of lock-in amplifier and thermostat, and three input controls for main information which is saved in the logfile.

The fifth and last tab (see Figure 59) contains indictor elements for parameters during the measurement and a graphical chart display for measured values. It also features an input control element for additional information during the measurement, which is saved to single measurement points is also located on this tab.

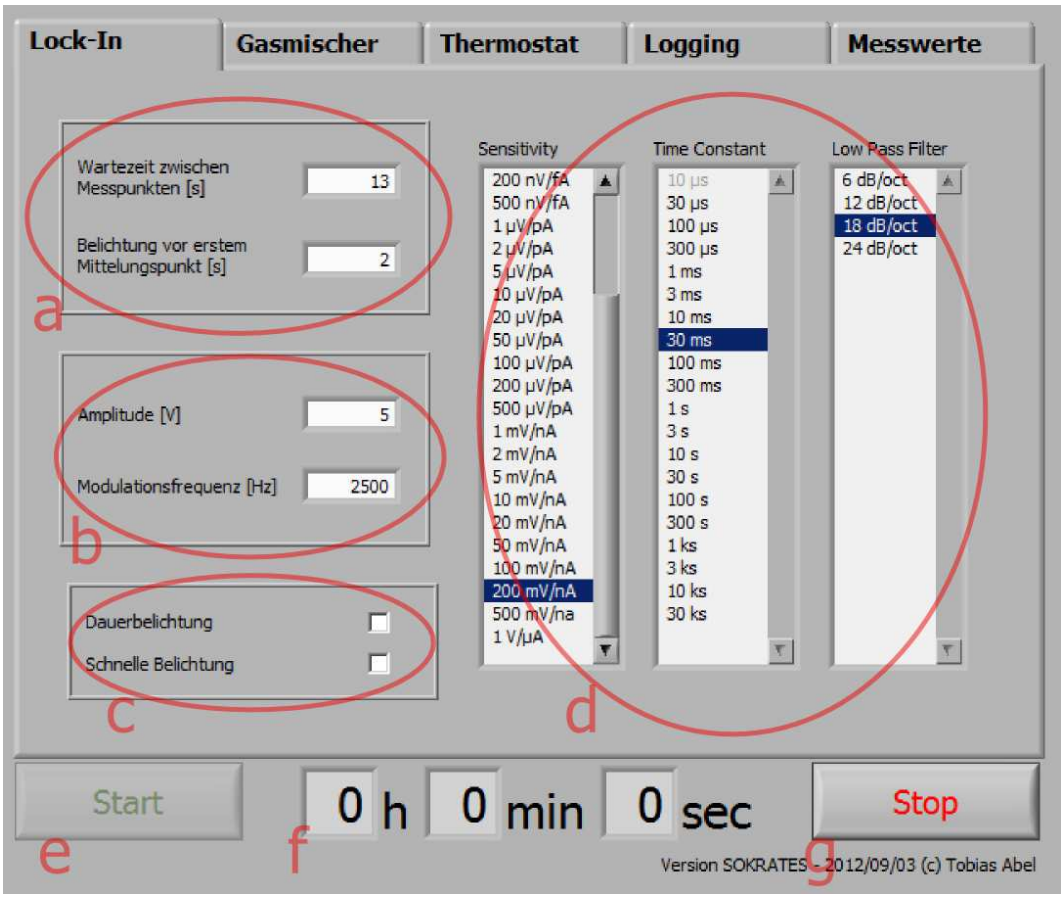

Figure 55: First tab of the program's front panel for the control of the lock-in amplifier: Input of measurement timing parameters (a), lock-in parameters for illumination (b), main measurement parameters (c) and listboxes for sensitivity, time constant and low pass filter of the lock-in amplifier (d). The main buttons for starting (e) and stopping (g) the program as well as a display of the elapsed measurement time (f) is located below the tabbed window.

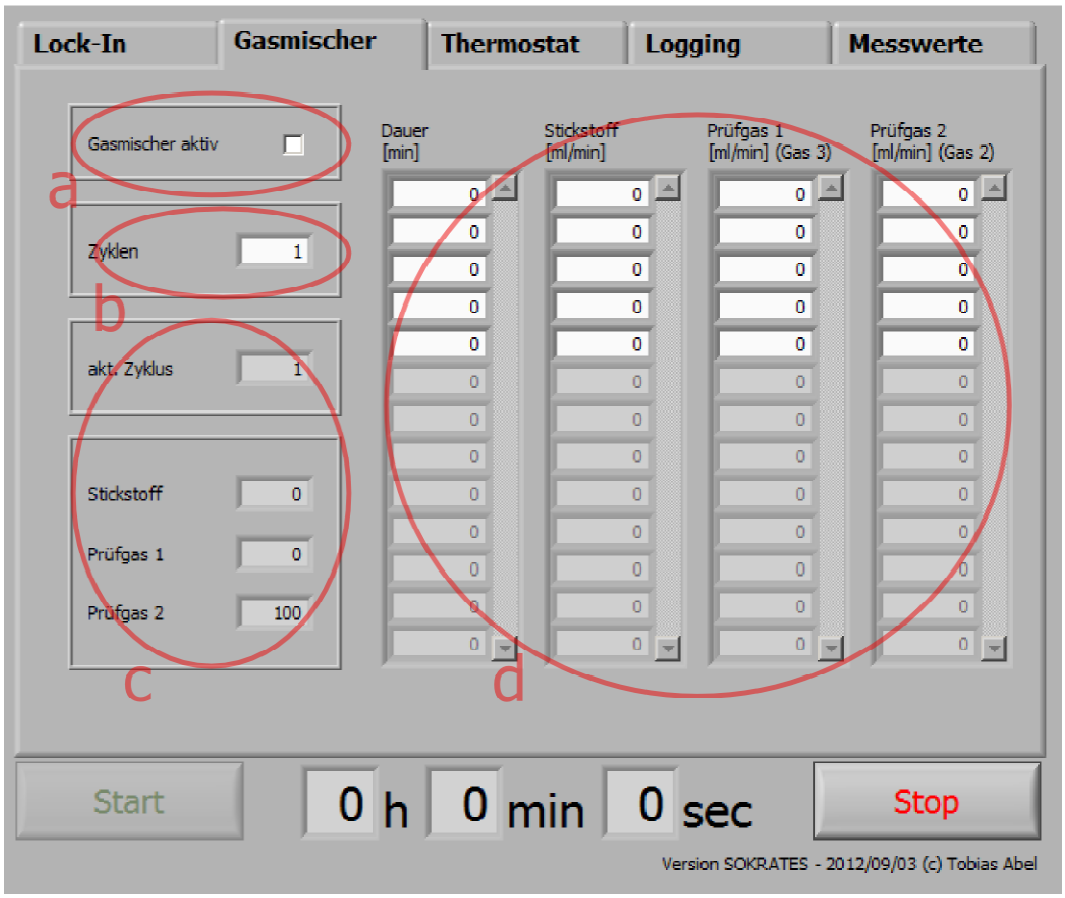

Figure 56: Second tab of the program's front panel for the control of the mass flow controllers: Checkbox for the activation or deactivation of the mass flow controller (a), input of number of cycles (b) and different gas mixing steps (d), and display of currently active mass flows (c).

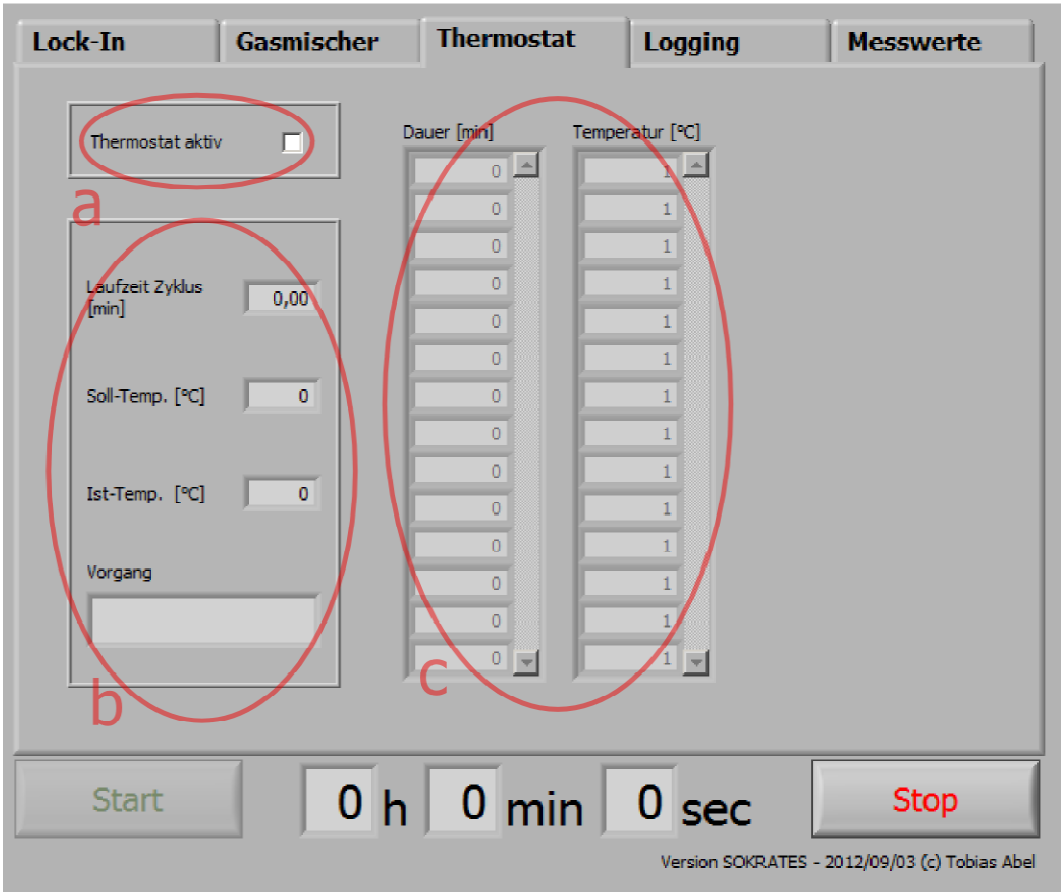

Figure 57: Third tab of the program's front panel for the control of the thermostat: Checkbox for the activation or deactivation of thermostat (a), input of duration and temperatures of different thermostat step (c) and display of currently active or measured thermostat values (c).

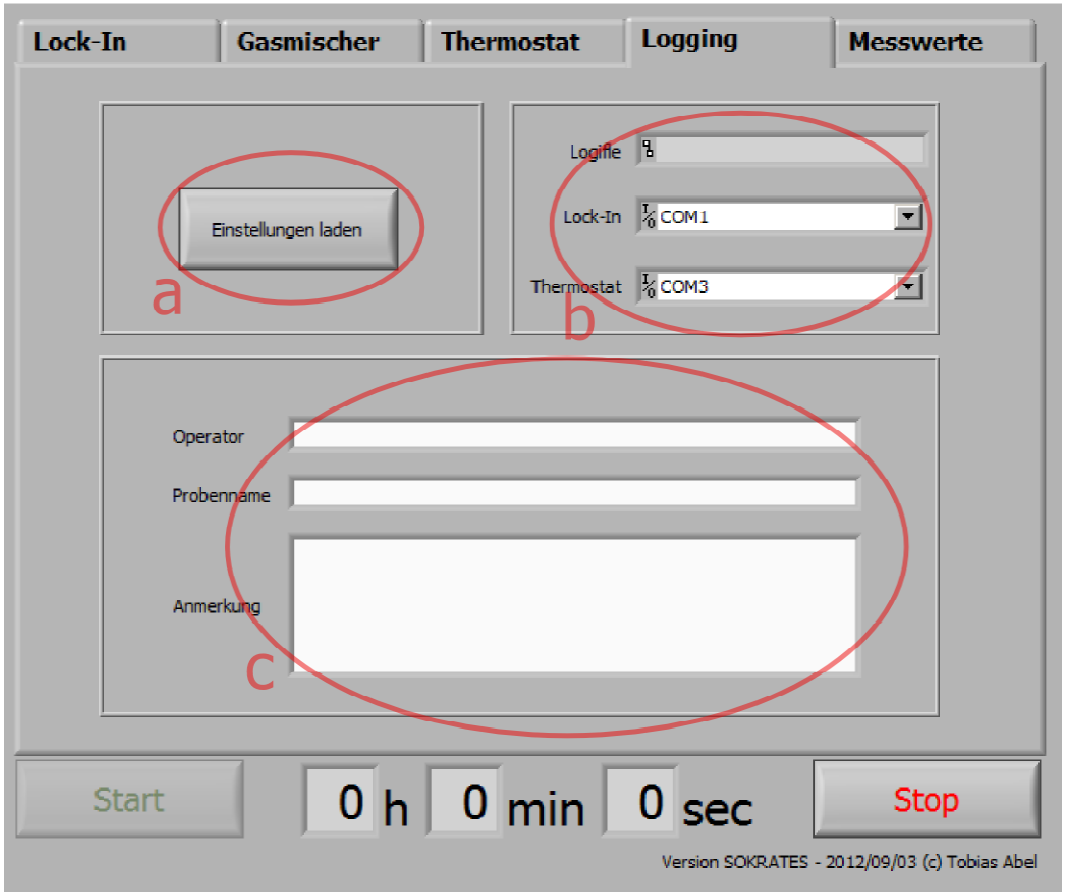

Figure 58: Fourth tab of the program's front panel for the main control of logging and instrument I/O: Button for loading of measurement parameter (a), file path for logfile and communication ports for the lock-in amplifier and thermostat (b) and input for measurement information saved in the header.

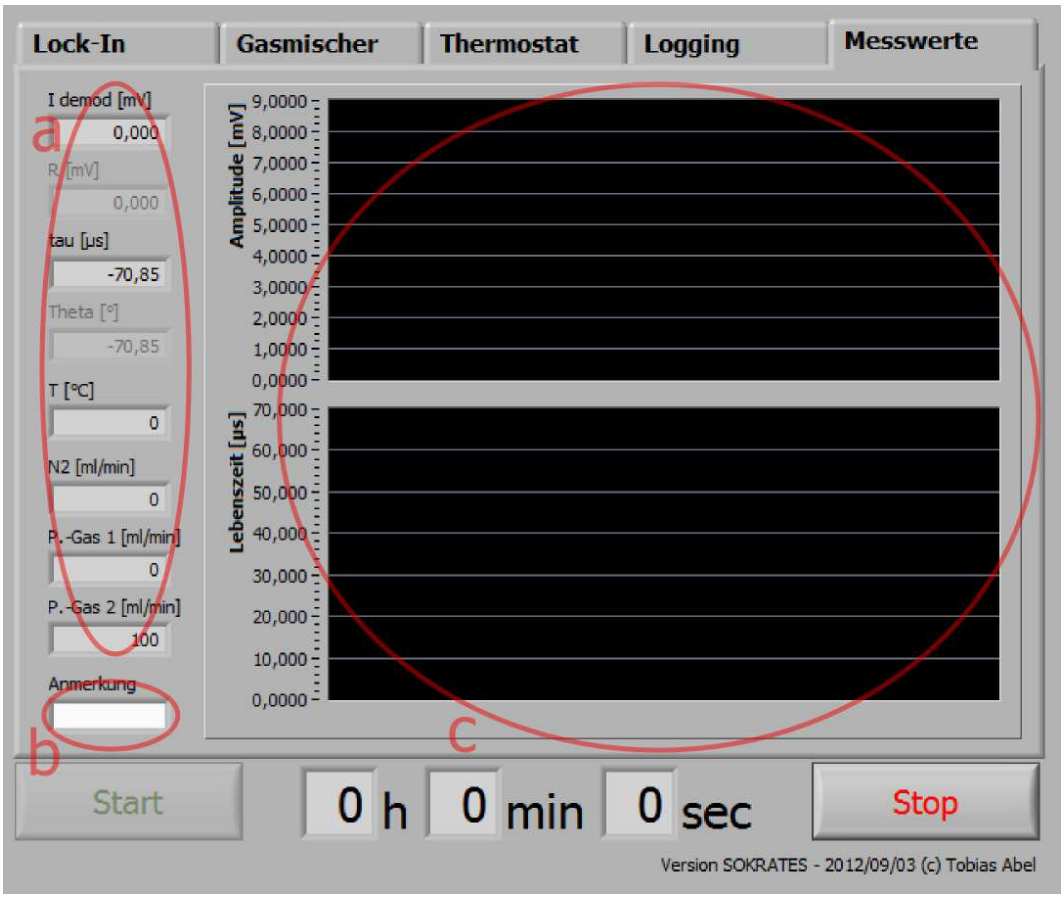

Figure 59: Fifth tab of the program's front panel for display of current measurement values: Currently measured values or active values of lock-in amplifier, mass flow controller and thermostat (a), input of notes for single measurement files saved in the log file (b) and display of current measurement values of the lock-in amplifiers (c).

Main Program

State machine design

The main design of the block diagram is based on a state machine with 7 different states. The state machine is timed by a 50 millisecond cycle and can

be stopped by the stop button during the measurement state. They states are as follows:Figure 60 shows an overview of the used states and their sequence.

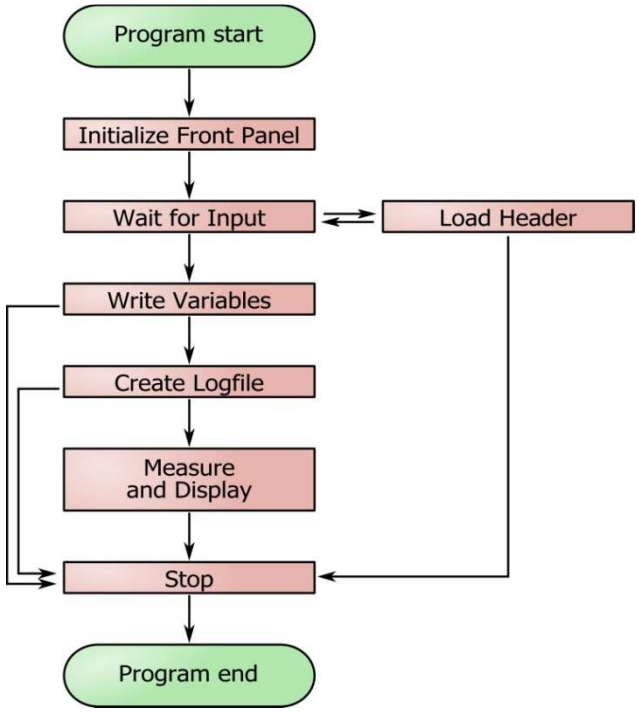

Figure 60: Sequence of states used in SOKRATES

Following every state will be described together with its block diagram. SubVIs within these states are discussed afterwards.

The first state, *Initialize Front Panel* (see Figure 61), has the task to prepare the front panel for the user. It consists of three property nodes: The first one assigned a cluster containing two constants of single values (0) to the wavechart indicator element, thus clearing its display from a previous measurement. The other two property notes control

the enabled state and the value of the main control buttons: START and STOP to increase usability. This state is executed one time and is succeeded by the state *Wait for Input*.

The second state, *Wait for Input* (see Figure 62), is repeated infinitely and holds the program active during any input action carried out by the user the user , which assigns input measurement values, gas flow rates and times and communication port numbers, and more. This state can be left by entering the *Write Variables* state (pressing START button) or by entering the *Load Header* state (pressing “Einstellungen laden” button).

The third state, *Load Header* (see Figure 63), is only executed once and can be entered by the user’s action of clicking on the “Einstellungen laden” button on the front panel. It consists of a SubVI, which loads a logfile of a previous measurement, reading all saved measurement and instrumentation parameters, and loading it into the control elements of the main program via local variables. After this, the program returns to the state *Wait for Input*. This state is executed once.

The fourth state, *Write Variables* (see Figure 64) is only executed once and is automatically entered after the state *Load Header*. Within this state the stop button is enabled and the start button is disabled Furthermore, all measurement and instrumentation parameters are bundled into clusters and saved into three different global variables, each containing clustered parameters for one instrument (lock-in amplifier, thermostat and mass flow controller)

The fifth state, *Create Logfile* (see Figure 65), is only executed once and is automatically entered after the state *Write Variables*. In this state the user is asked by a dialog box if she or he wants to save the measurement data to a logfile or not. If so, a logfile is created afterwards including the header with important measurement, instrumentation and time schedule parameter. The state is succeeded by *Measure and Display*.

The sixth state, *Measure and Display* (see Figure 66) is only executed once and is automatically entered after the state *Load Header*. It is the main state for the process of instrument input and output as well as for the display of current measurement values. It consists of a While Loop responsible for the display of all measured values, a While Loop responsible for the interface towards the lock-in amplifier and the logging function and a combination of a For Loop and a Sequence, which addresses the interface of the MFCs and the Thermostat. This state can be left manually by the user’s action of toggling the STOP button or will be left automatically after the last control step.

The seventh state (*Stop*) is the last state, which is executed in this program. It closes the mass flow controller and resets the global variable *GlobMeasStop*. Afterwards the whole LabVIEW program is stopped.

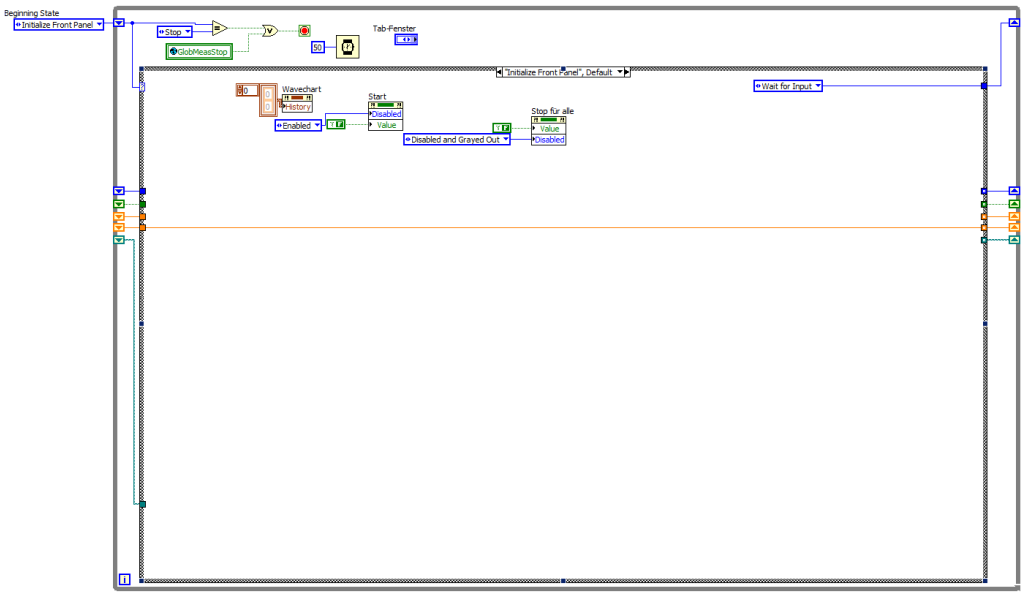

Figure 61: Block diagram of the first state *Initialize Front Panel*.

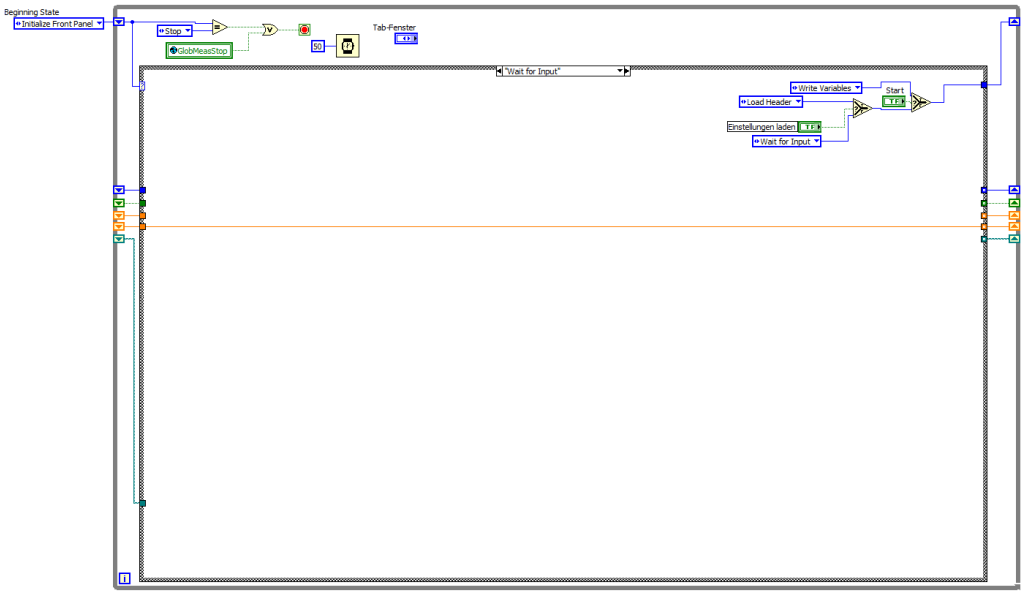

Figure 62: Block diagram of the second state *Wait for Input*.

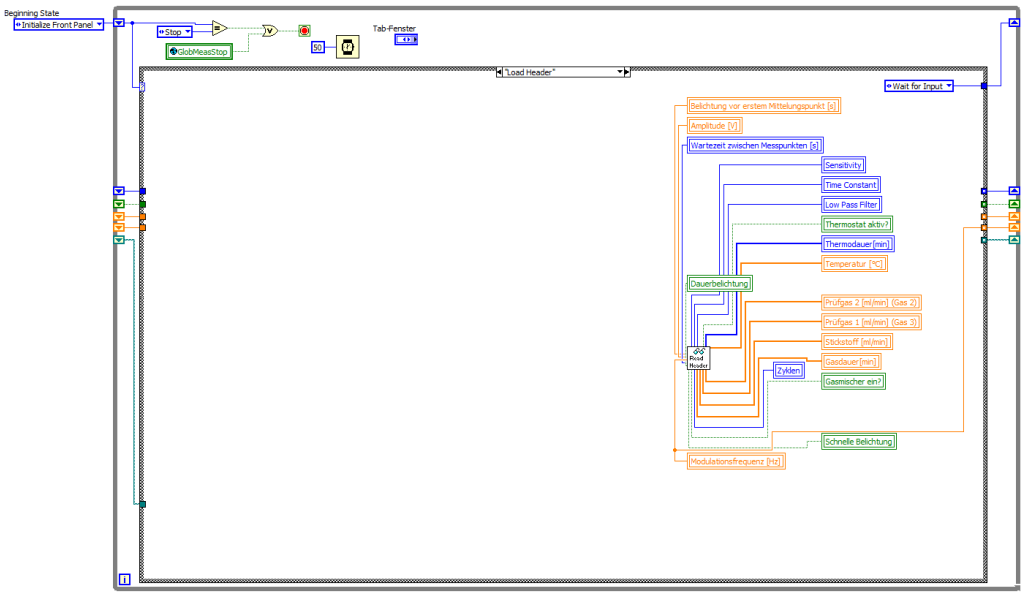

Figure 63: Block diagram of the third state *Load Header*.

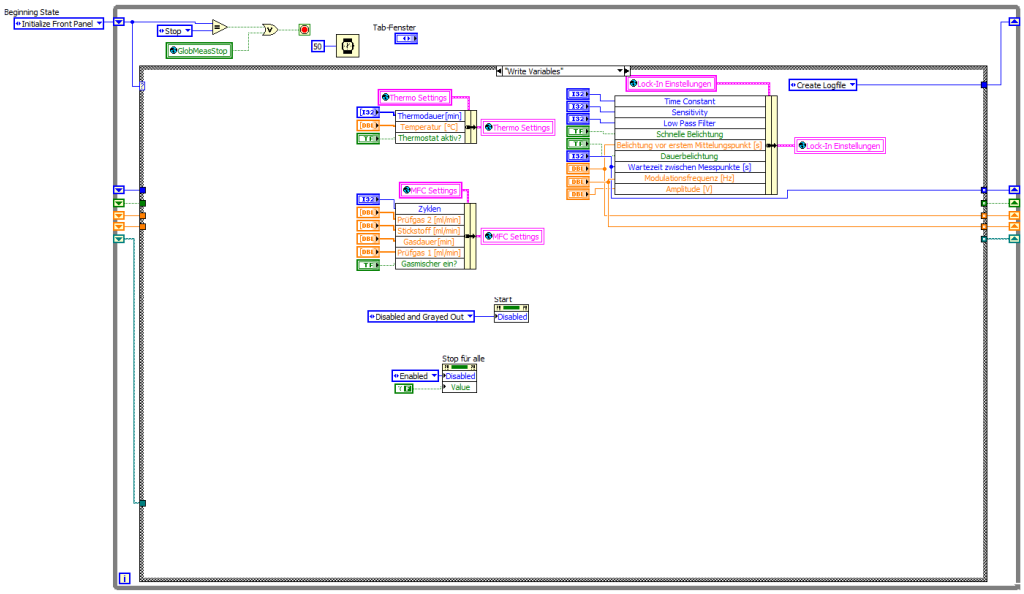

Figure 64: Block diagram of the fourth state *Write Variables*.

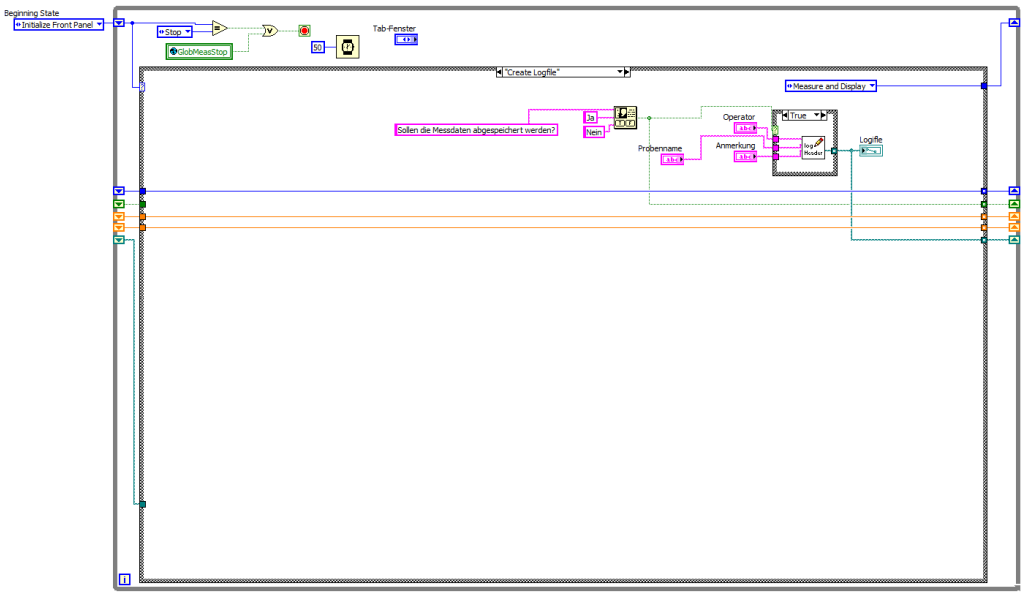

Figure 65: Block diagram of the fifth state *Create Logfile*.

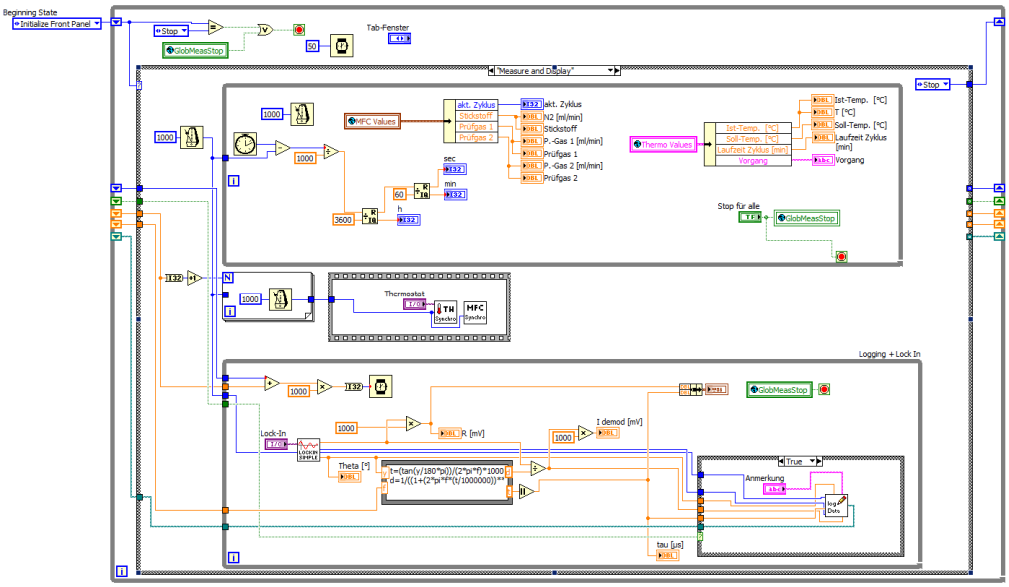

Figure 66: Block diagram of the sixth state *Measure and Display*.

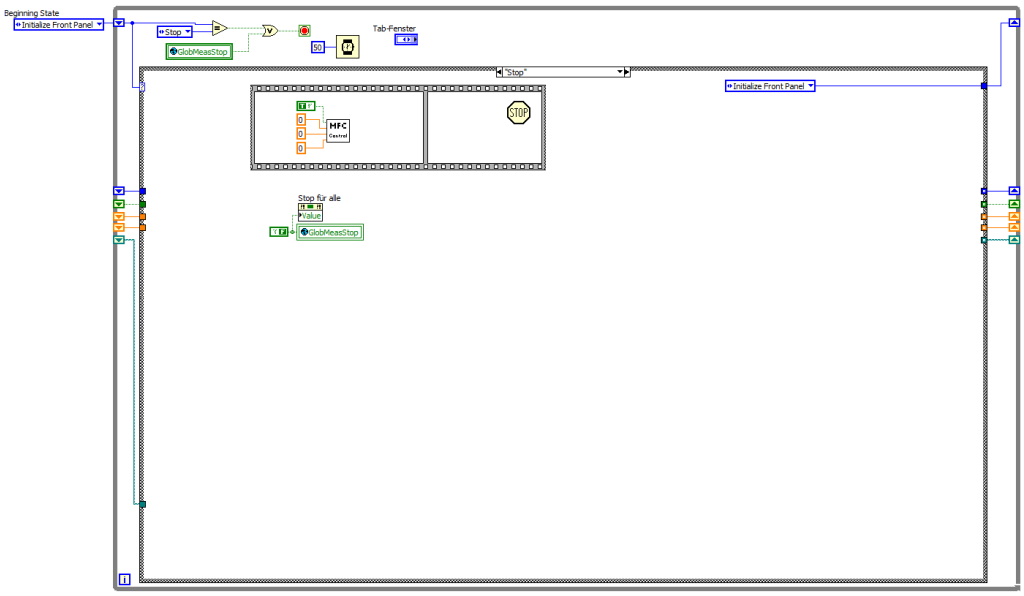

Figure 67: Block diagram of the seventh state *Stop*.

Global Variables

In early versions of SOKRATES all measurement parameters, data and values were accessed and passed in the block diagram via data wires. This is possible, but constrains the programming due to the sheer amount of necessary data wires. Thus, all main parameters and values are stored within Global Variables[2]. The benefit of this approach is that data can be read and written simultaneously by different VIs and SubVIs of different levels within the program's whole hierarchy. But it is important to pay attention during the programming that accessing, writing, and reading of different VIs has to be scheduled correctly.

Global Variables consist solely of a block diagrams, which contains control fields and data, accessed from each SubVI. All variables within this program consists of clusters, one cluster for parameters necessary to control and schedule the instrument and one containing measured values (except the variable for the lock-in amplifier). The block diagram of these variables can be seen in Figure 68, Figure 69 and Figure 70.

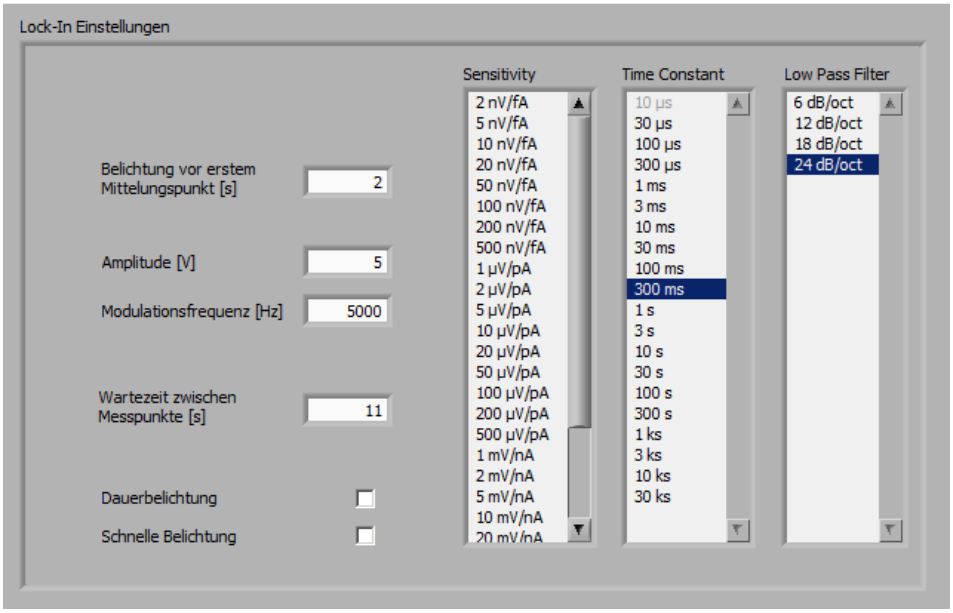

Figure 68: *Lock-In Variablen*, the global variable for the control of the lock-in amplifier

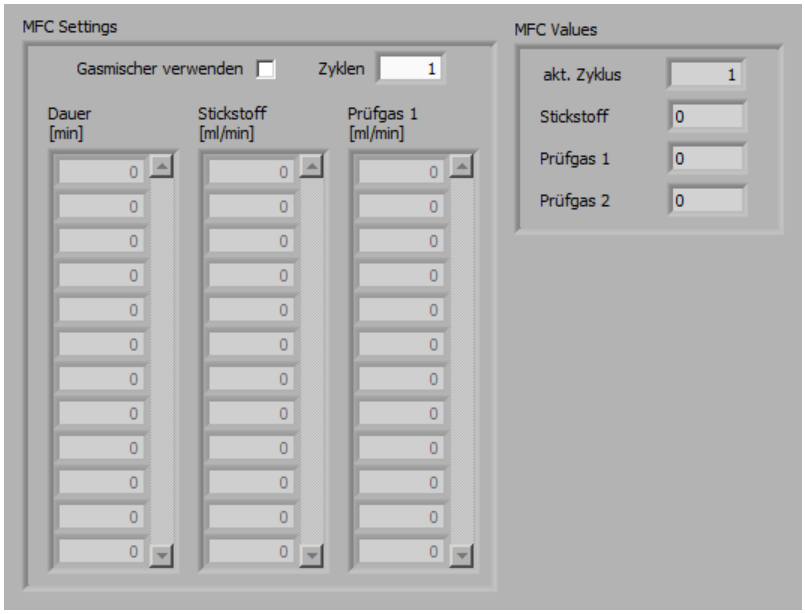

Figure 69: *Massflow Variablen*, the global variable for the control of the MFCs.

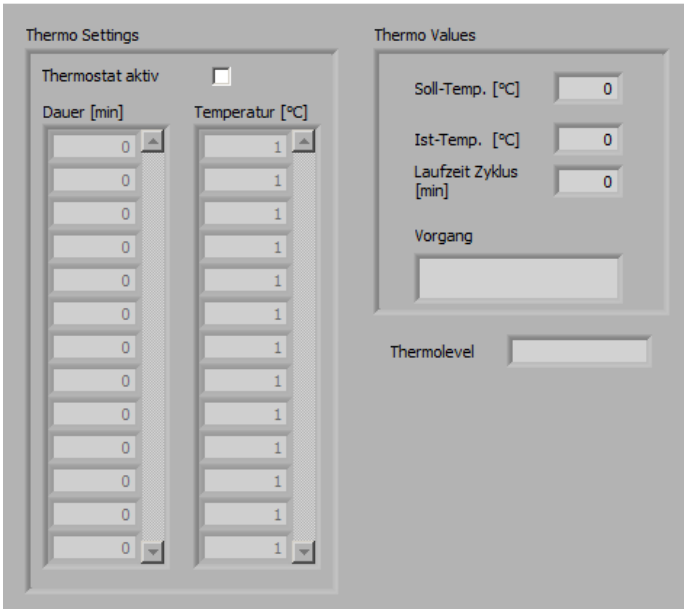

Figure 70: *Thermo Variablen*, the global variable for the control of the thermostat.

Logfile header control

Structure of the logfile's header

The measurement values can be saved in a logfile. This logfile contains a header, which carries important information about measurement and instrumentation parameters. The following paragraph depicts a complete header from a measurement, in which mass flow controller and thermostat was used.

```
Messprotokoll

Operator     tobi
Probenname   PtTPP 1% mit C545T 2% in 5% PS aus THF vom 8.3
Anmerkung    450nm mit BG12 und RG630 bei 350V
Datum  10.März 2011
Zeit   12:53

EINSTELLUNGEN Lock-In:
Modulationsfrequenz [Hz]  5000
Amplitude [V]5,000
Schnelle Belichtung Aus
Dauerbelichtung     Aus
Belichtungsdauer vor erstem Messpunkt [s]     1,000
Wartezeit zwischen den Messpunkten [s] 29
Time Constant30 ms
Sensitivity  500 mV/na
Low Pass Filter     18 dB/oct
EINSTELLUNGEN Lock-In - ENDE

EINSTELLUNGEN Gasmischer:
Gasmischer   An
Zyklen 5
Dauer [min]  Stickstoff [ml/min] Prüfgas 1 [ml/min]  Prüfgas 2 [ml/min]
10     100    0      0
2      75     0      25
2      50     0      50
2      25     0      75
2      0      0      100
EINSTELLUNGEN Gasmischer - ENDE

EINSTELLUNGEN Thermostat:
Thermostat   An
Dauer [min]  Temperatur [°C]
18     10
18     15
18     20
18     25
18     30
EINSTELLUNGEN Thermostat – ENDE

Uhrzeit      Zeit   Amplitude    Theta  Abklingzeit  Trägergas    Pruefgas
1      Pruefgas 2   Temperatur   Anmerkung
hh:mm:ss     s      V      °deg   µs     ml/min ml/min ml/min °C
```

The first paragraph contains general information about the measurement: The operator's name (*Operator*), the name of the experiment (*Probenname*), additional notes (*Anmerkung*), as well as the date (*Datum*) and the time (*Zeit*) of the measurement. The information of the first three lines is provided by the user and is not generated automatically, while the date and the time of the measurement are saved automatically by the program during the creation of the logfile.

The second paragraph contains measurement settings and parameters of the lock-in amplifier. The meaning of these parameters is explained in the chapter concerning the SubVI which controls the lock-in amplifier (see page 138). The third and the fourth paragraph contain the experimental settings of the mass flow controller and the thermostat respectively. This information is simply the number of cycles (mass flow controller only) and a scheduled list of gas flow or temperature steps.

All parameters are separated by tabulators. All lines are separated by an *End Of Line* Constant[3]. This constant is a combination of the two ASCII characters *Carriage Return* (0x0D, \r) and *Line Feed* (0x0A, \n). The *End Of Line* Constant is used in most non-Unix operating systems (e.g. Windows, Symbian OS, Android).

Creating the Header

The header of the log file is created within the state *Create Logfile*, if the user decided to do so (see Figure 65). This is carried out by a two-button dialogue box, triggering a Case Structure equal to the users' response. If the user wants to create a logfile, the true case and the SubVI *WriteHeadControl* is entered. Only the user-provided measurement information is transferred per data wires into the SubVI, the output information of the SubVI *WriteHeadControl* is the path of the logfile.

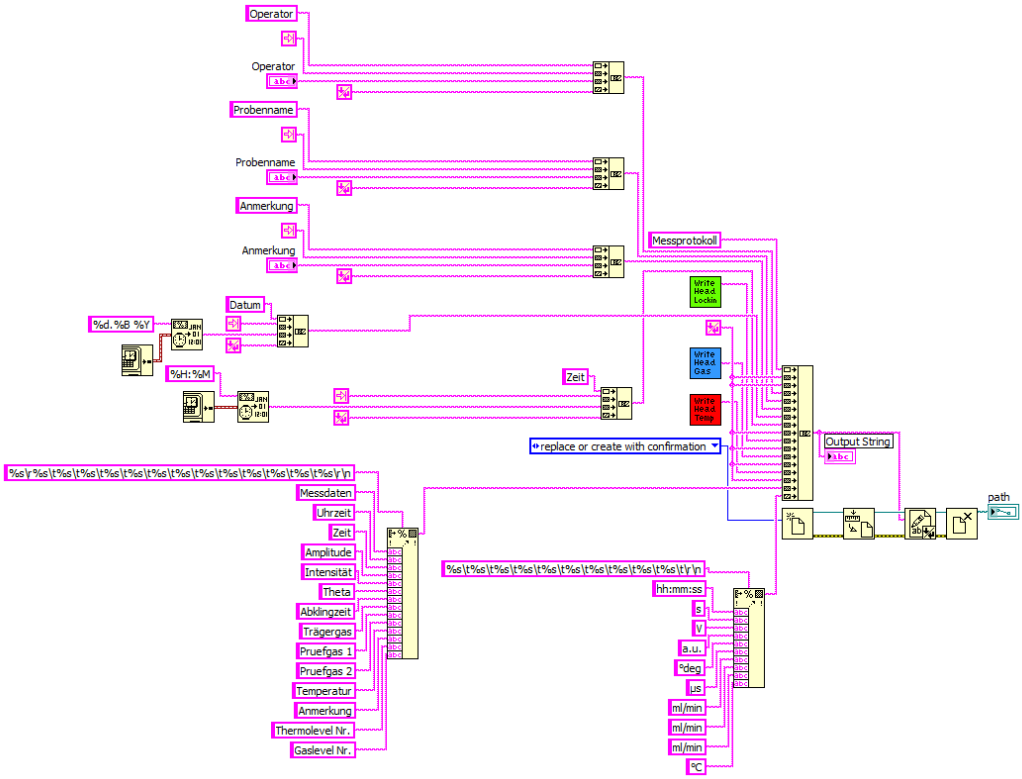

Figure 71: Block diagram of the SubVI *WriteHeadControl*

As depicted in Figure 71, the SubVI consists of numerous *Concatenate String* functions, which combines all information necessary to form the header. On the upper left part on the block diagram the user-provided measurement information (see Figure 58) and the date and time stamp are combined. On the right side further SubVIs can be seen, which combine the strings for the measurement and instrumentation parameters of lock-in (green SubVI), mass flow controller (blue SubVI) and thermostat (red SubVI). The last two strings of the main *Concatenate String* function define the headlines for the measurement values. Further functions to create, save and write into the logfile are placed below the main *Concatenate String* function

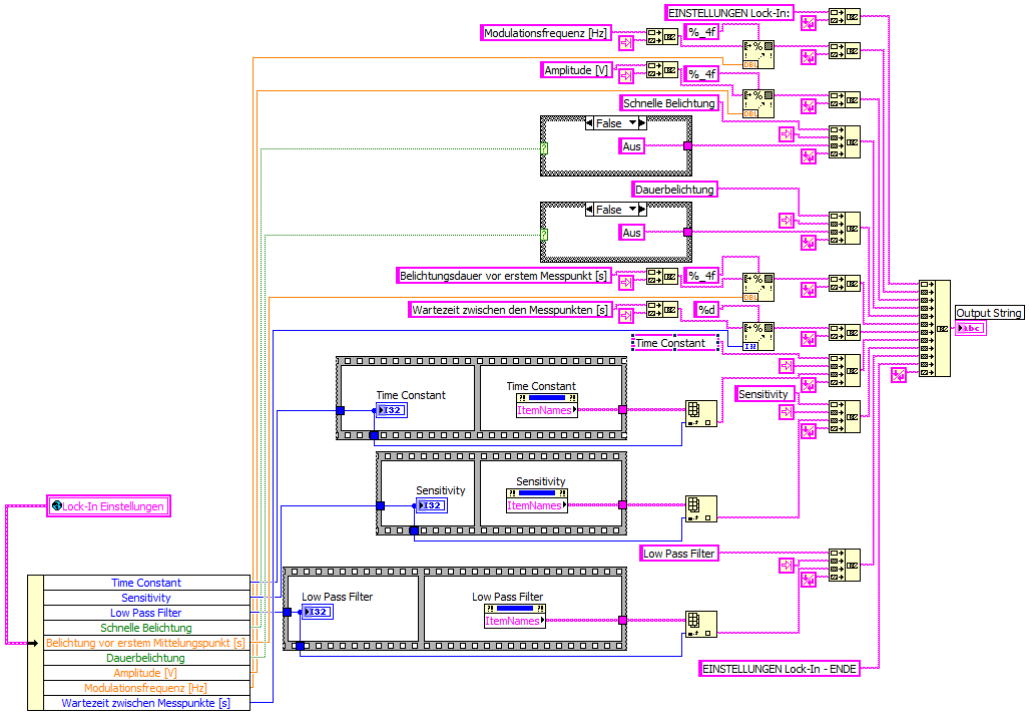

Figure 72: Block diagram of the SubVI *WriteHeadL*

As seen in Figure 72, the creation of the string containing the measurement parameters of the lock-in amplifier are carried out by reading the cluster *Lock-In Einstellungen* within the global variable *Lock-In Variablen*. The cluster *Lock-In Einstellungen* is unbundled (lower left corner of the block diagram) and each parameter is concatenated with string constants, tabulators and *End Of Line* feeds to lines (middle part of the block diagram), which then are concatenated to the Output String (right side of the block diagram). This output string contains all information between the lines “EINSTELLUNGEN Lock-In:” and “EINSTELLUNGEN Lock-In – ENDE” of the logfile’s header, and is passed to the SubVI *WriteHeadControl* on the end of the block diagram.

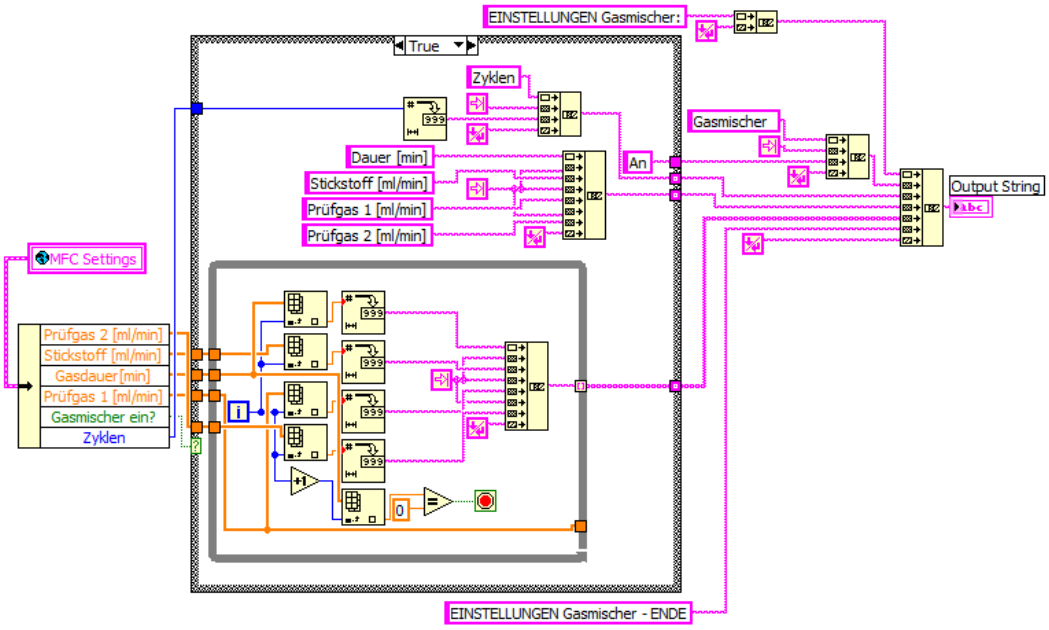

Figure 73: Block diagram of the SubVI WriteHeadG

Figure 20 shows the block diagram of the SubVI *WriteHeadG*, which forms the string of the measurement parameters regarding the control of all used mass flow controller. For this, the cluster *MFC Settings* of the global variable *Massflow Variablen* is read, unbundled and then concatenated into an output string. Since the number of gas mixing step can vary at each experiment, the read-out system is based on a While Loop, which reads at each loop iteration, the corresponding element of each array (duration and flow rate of each MFC). The loop is automatically closed if the next iteration would be recognized as zero.

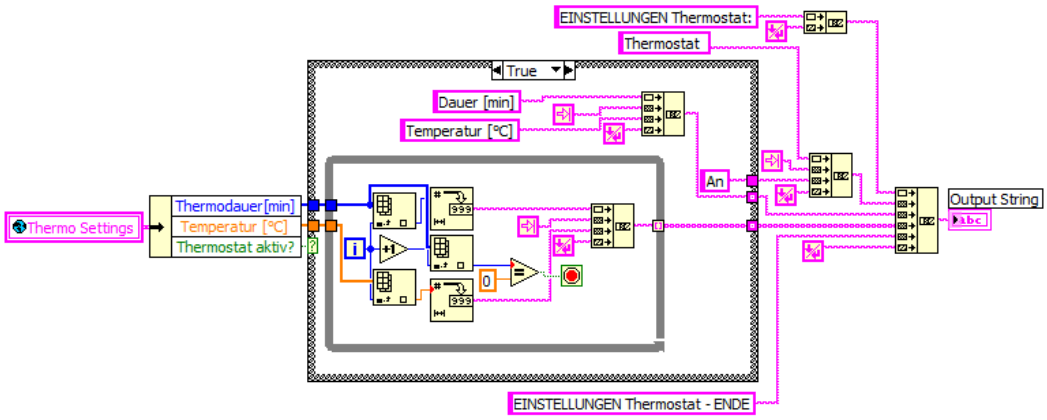

Figure 74: Block diagram of the SubVI *WriteHeadT*

The block diagram of the SubVI *WriteHeadT* is shown in Figure 74. It is similar to the block diagram of the SubVI *WriteHeadG.* The cluster *Thermo Settings* of the global variable *Thermo Variablen* is read, unbundled and concatenated to the output string. The varying length of the temperature step list is read out by a While Loop, which is closed when the thermostat's duration of the loop's next iteration is detected to be zero.

Loading the Header

The user can load measurement and instrumentation parameters of previous measurements by reading out the header of these logfiles. This step is done in the state *Load Header* and executed by the SubVI *ReadLog*. This SubVI consist of an flat sequence with three windows, each containing functions to deconstruct the logfile's header. The sequence's first window reads the lock-in parameters, the second window reads the mass flow controller parameters, and the third reads the thermostat parameters.

In the first window the whole header string is read, cut from everything before the string "EINSTELLUNGEN Gasmischer:" and deconstructed by a *Scan from String* function. The following format string defines the data position within the string.

```
%s\s%s\n%s\s%s\t%_4f\n%s\s%s\t%_4f\n%s\s%s\t%s\n%s\t%s\n%s\s%s\s%s\s%s\s%
s\s%_4f\n%s\s%s\s%s\s%s\s%s\s%d\n%s\s%s\t%s\s%s\n%s\t%s\s%s\n%s\s%s\s%s\t
%s\s%s
```

%s, \s, \n and \t are the syntax elements for strings, spacings, end of line characters and tabulators, respectively. t%_4f is the format syntax for a four-digit floating point number. The values are processed if necessary (Boolean values or integer values of 1D arrays), bundled and written in the cluster *Lock-In Einstellungen* within the global variable *Lock-In Variablen* (see Figure 75).

The second window of the sequence (see Figure 76) accesses the measurement parameters of the mass flow controller. It reads the string passed from the sequence's first window and cuts it at the string "EINSTELLUNGEN Thermostat:". The activation of the MFC, the number of gas cycles, the flow durations and the flow rates are read from the residual part after this cut.

The flow durations and the flow rates are localized by a *Search/Split Sting* function, read, converted into a two dimensional array, transposed and then split into four different, one-dimensional arrays (one array for gas duration and three arrays for flow rates).

The third and last window (see Figure 77) reads the thermostat's measurement parameters within the header. It has the same design as the sequence's second window, since the algorithm of writing the header part dealing with the thermostat's measurement parameters is similar ot the algorithm of writing the header part dealing with the MFC's measurement parameters.

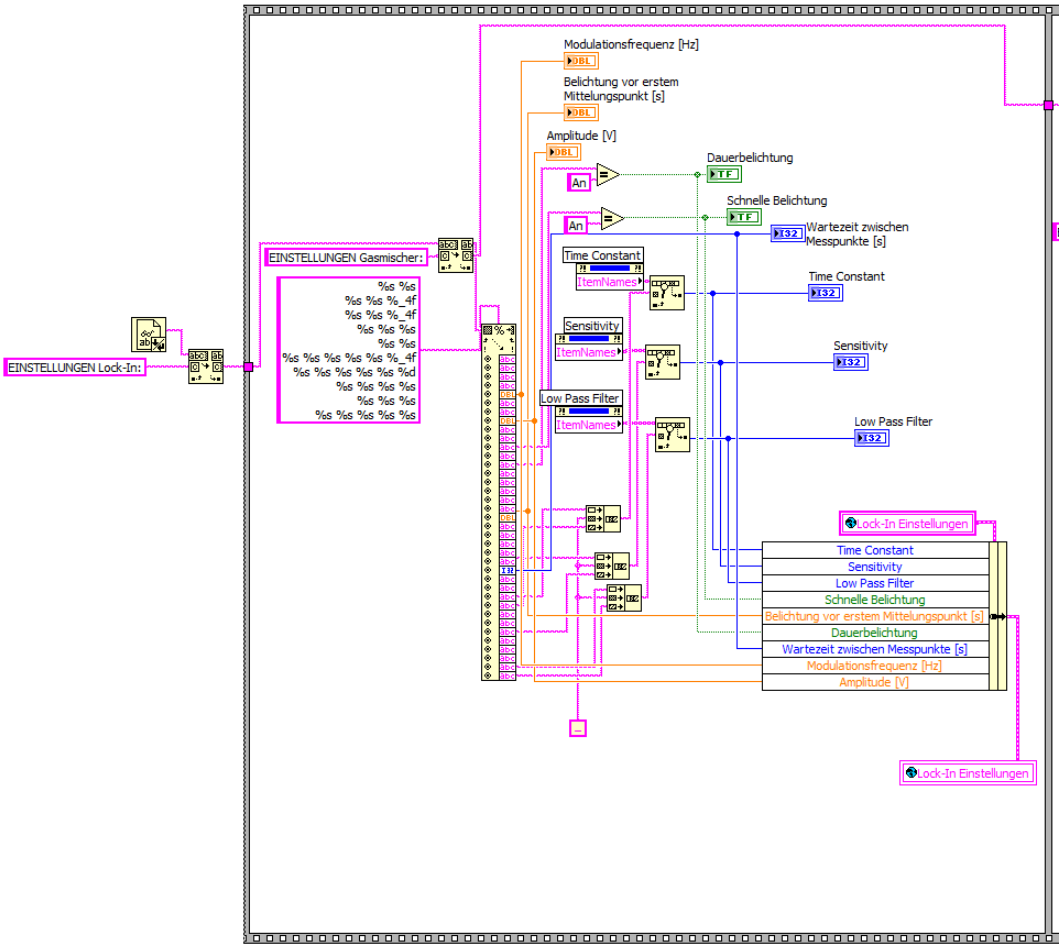

Figure 75: First sequence window of the Block diagram of *ReadLog*.

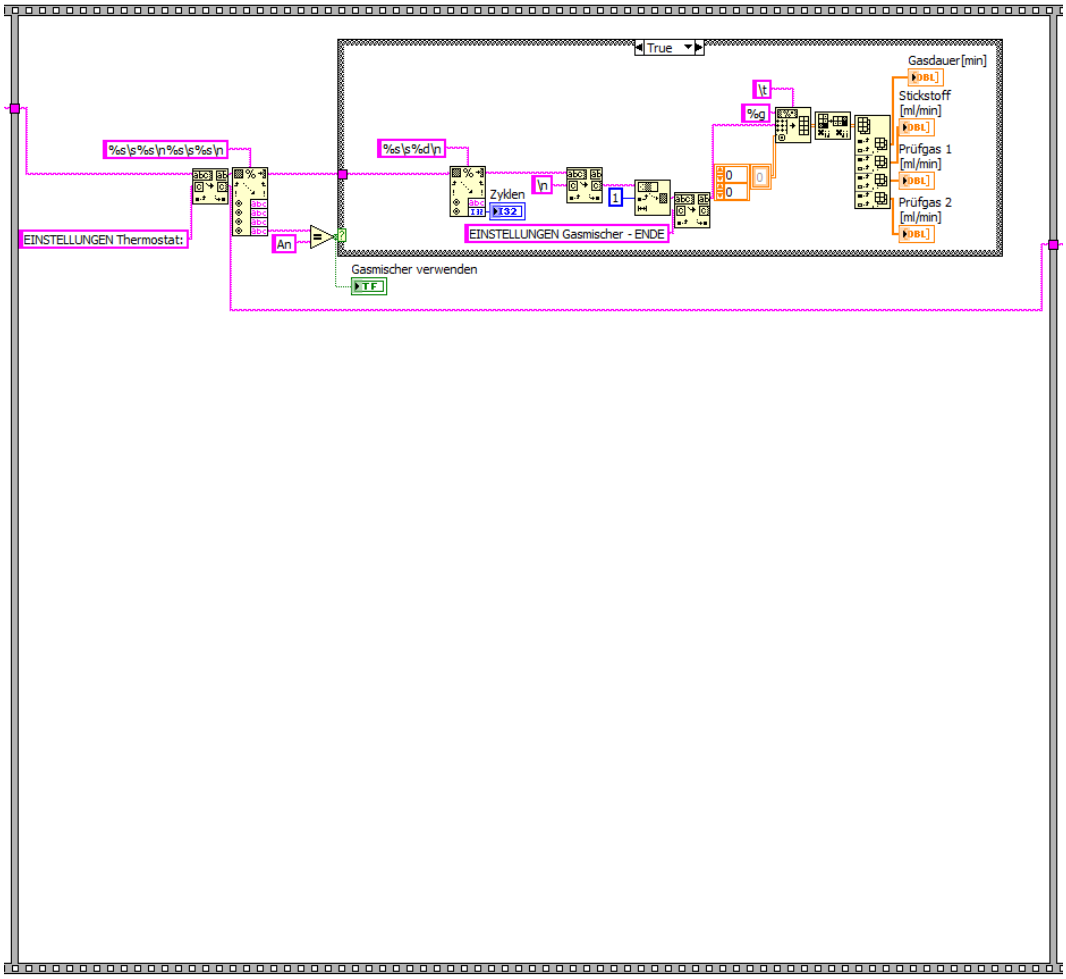

Figure 76: Second sequence window of the Block diagram of *ReadLog*.

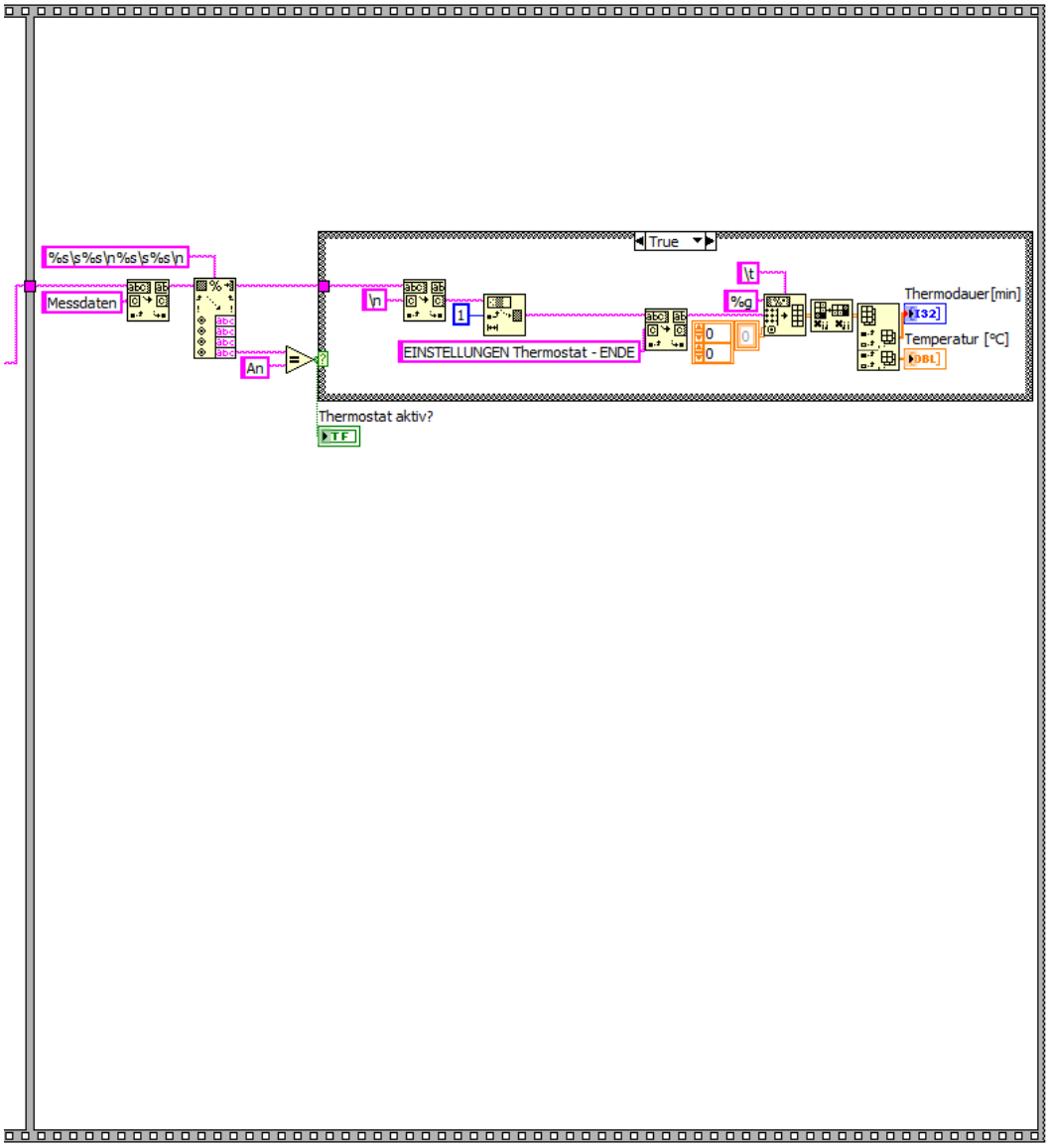

Figure 77: Third sequence window of the Block diagram of *ReadLog*.

Control of lock-in amplifier

Main control of the lock-in

The central part of the program is the input and output control of the lock-in amplifier. It is realized with a While Loop in the *Measure and Display* state (see Figure 78).

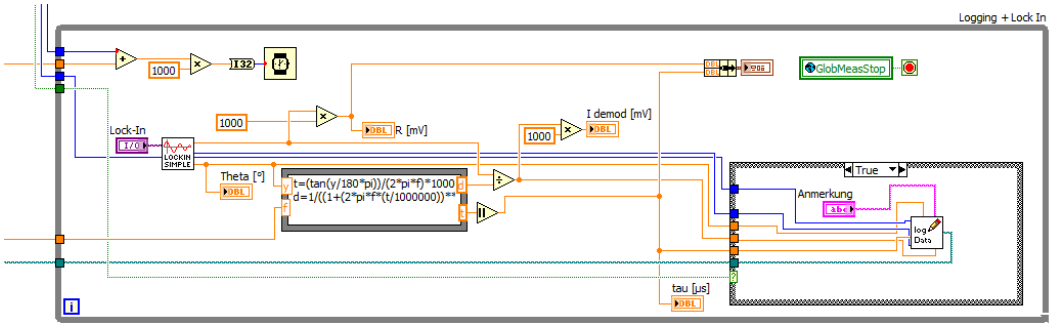

Figure 78: Block diagram of the main input and output control of the lock-in amplifier.

The main parts of this loop are as follows:

- A SubVI called *Lock-In Control* to which all necessary parameters are transmitted. This SubVI sends the measurement parameters to and reads the measurement values from the lock-in amplifier
- A *Formula Node*, which calculates the demodulated intensity and the decay time according to the measurement values read by the *Lock-In Control* SubVI and the measurement parameters defined by the user. The decay time is calculated based on the measured phase shift by equation 12 (τ: decay time [s], φ: phase shift, f: modulation frequency [Hz]) and the demodulated intensity is calculated from the measured amplitude by equation 14 (A: measured amplitude, f: modulation frequency [Hz], τ: decay time [s]).

$$\tau = \frac{tan\,\varphi}{2 \cdot \pi \cdot f} \quad (13)$$

$$d = \frac{A}{\sqrt{1 + (2 \cdot \pi \cdot f \cdot \tau)^2}} \quad (14)$$

- A *Case Structure*, which controls the logging of the measured and calculated values. The FALSE case is empty, following the user's desire not to log any data. The TRUE case contains a SubVI called *Datalogging*.
- A *Wait (ms)* function, which controls the time lag between two measurement points.

Figure 79 shows a simple diagram depicting the sequence of the Lock-In Control cycle.

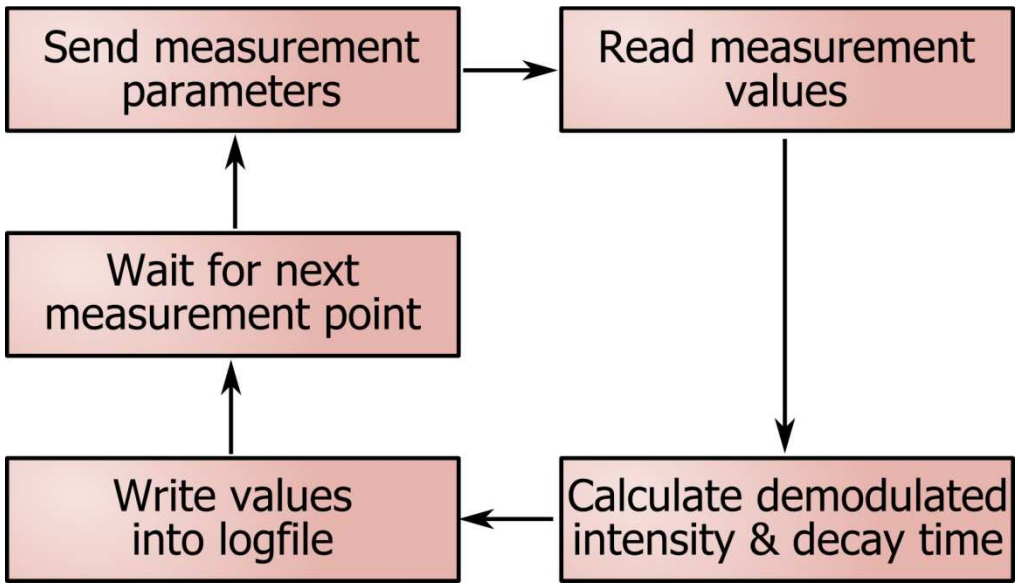

Figure 79: Basic scheme of the Lock-In Control cycle.

SubVI *Lock-In Control*

The SubVI *Lock-In Control* is accessed every iteration of the While Loop controlling the lock-in amplifier. It is a simple state machine, in which the sequence of states is determined by the user's defined measurement parameters. This SubVI sends commands and receives measurement data from the lock-in via two SubVIs: *Lock-In Write* and *Lock-In Read*. The first SubVI sets parameters on the lock-in amplifier, while the second SubVI reads measurement values. The communication is based on string commands, documented in the manual of the SR830 lock-in amplifier (see manual, chapter 1-7[4]).

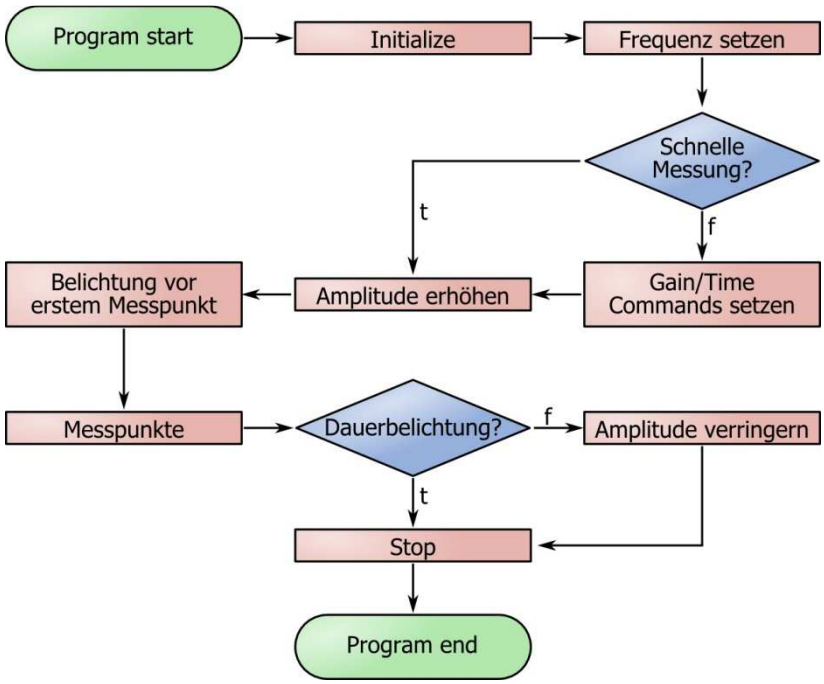

Figure 80: Sequence of the states used in the state machine of the SubVI *Lock-In Control*.

A predefined communication port for the RS-232 communication (*VISA resource name* on the block diagram) is accesses from the main program and predefined by the user. The communication port is opened and closed every time the SubVI *Lock-In Control* is executed. While this takes a minimal amount of time, it reassures that during a non-scheduled abortion of the main VI the port is not active and ready for use of another VI instance.

The first state (*Initialize*, see Figure 81) is an empty state, only referring to the second state. This state is part of every state machine and is empty, because no initialization of a front panel is necessary in this SubVI. The second state (*Frequenz setzen*, see Figure 82) sets the user defined modulation frequency. The third state (*Gain/Time Commands setzen*, see Figure 83) sets three parameters, defining the sensitivity, the time constant and the low-pass filter intensity. This state is only executed, if the Boolean variable *Schnelle Messung* is FALSE, in this case the fourth state would follow the second state. *Amplitude erhöhen,* the fourth state (see Figure 84), raises the amplitude to the value of the measurement, which is defined by the user. This state is followed by the fifth state, *Belichtung vor erstem Messpunkt* (see Figure 85), in which *Wait (ms)* function is executed to wait a predefined millisecond value predefined by the

user. Afterwards the sixth state, *Messpunkte* (see Figure 86), is executed, in which the measurement values from the lock-in amplifier are read. Also, the CPU time of the moment receiving the current measurement value is determined. Depending on another Boolean Variable, *Dauerbelichtung*, the seventh state is *Amplitude verringern* (see Figure 87). In this state the amplitude is reset to 0. If *Dauerbelichtung* is TRUE, the seventh state is not executed and the sixth state is followed by the eighth and final state, *Stop* (see Figure 88). This state primarly defines the end of the While Loop which contains the Case Structure of the state machine.

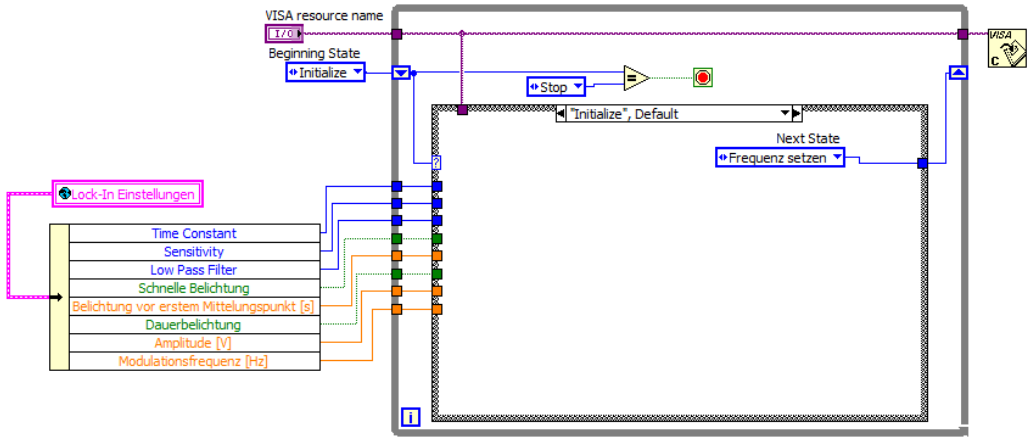

Figure 81: Block diagram of the state *Initialize* of the *Lock-In Control* SubVI.

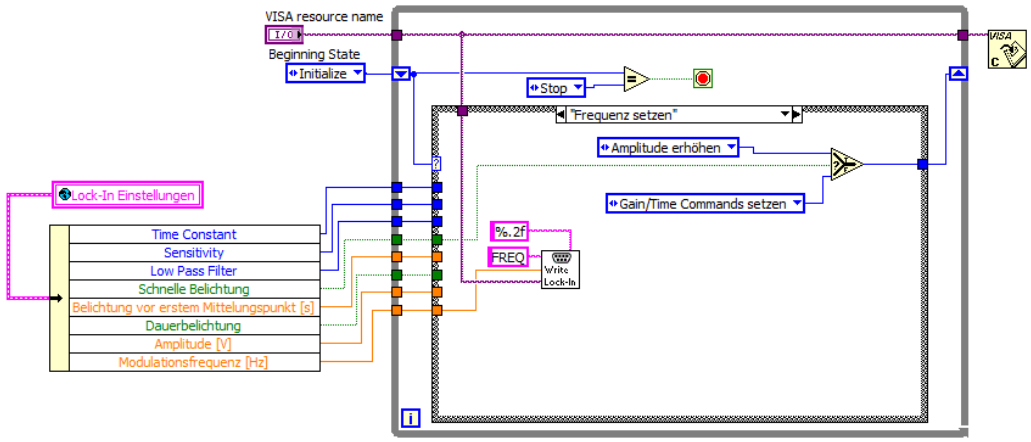

Figure 82: Block diagram of the state *Frequenz setzen* of the *Lock-In Control* SubVI.

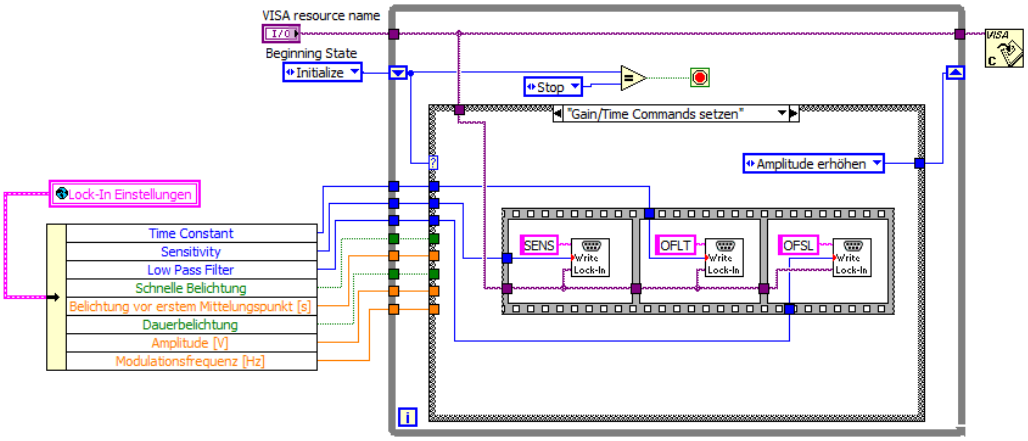

Figure 83: Block diagram of the state *Gain/Time Commands setzen* of the *Lock-In Control* SubVI.

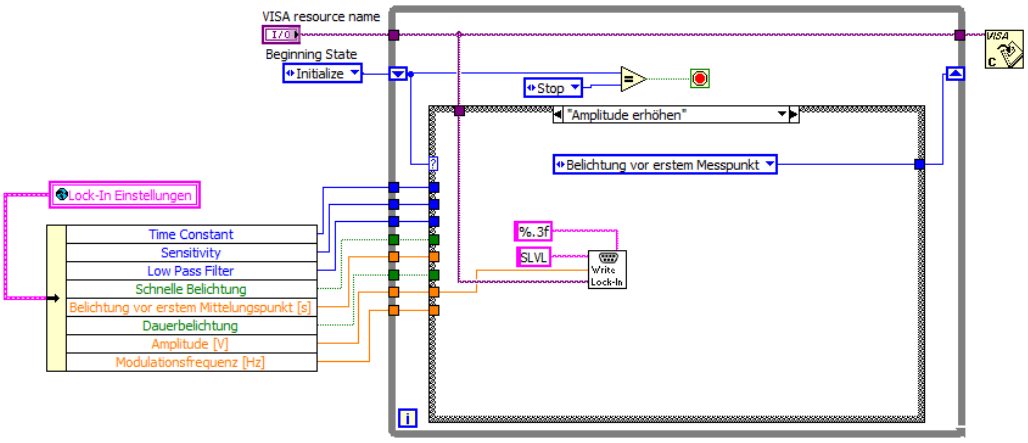

Figure 84: Block diagram of the state *Amplitude erhöhen* of the *Lock-In Control* SubVI.

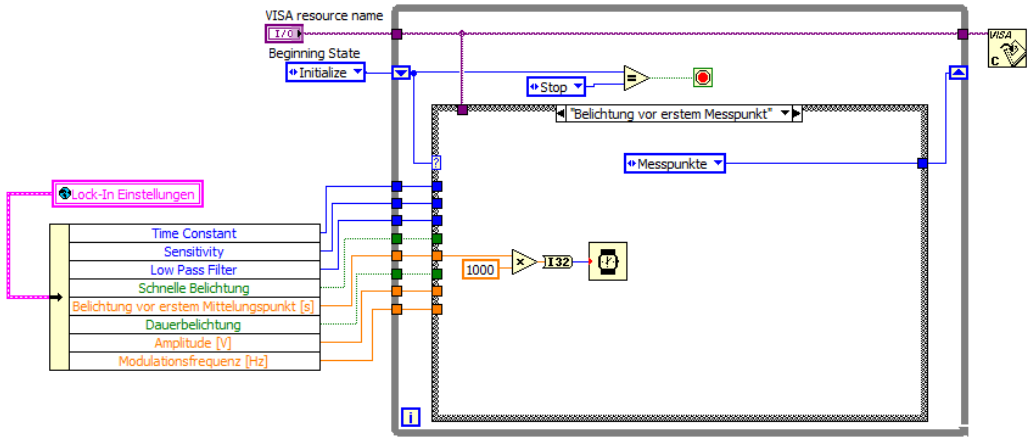

Figure 85: Block diagram of the state *Belichtung vor erstem Messpunkt* of the *Lock-In Control* SubVI.

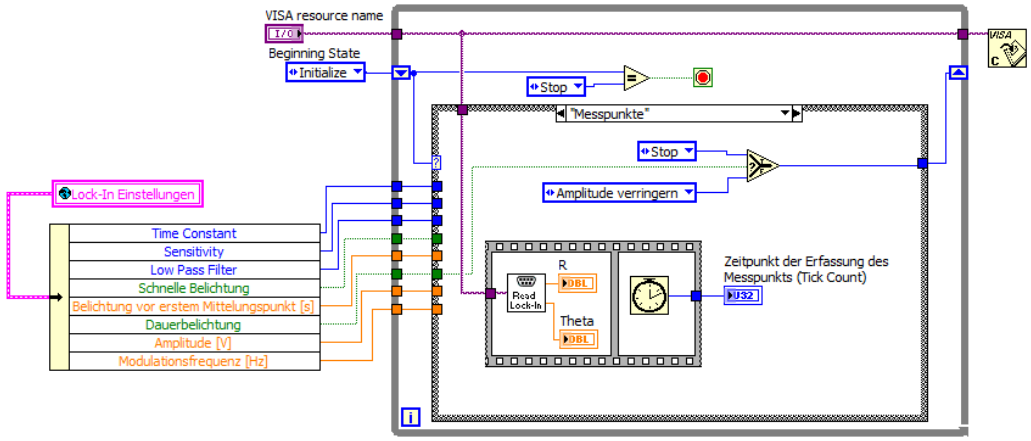

Figure 86: Block diagram of the state *Messpunkte* of the *Lock-In Control* SubVI.

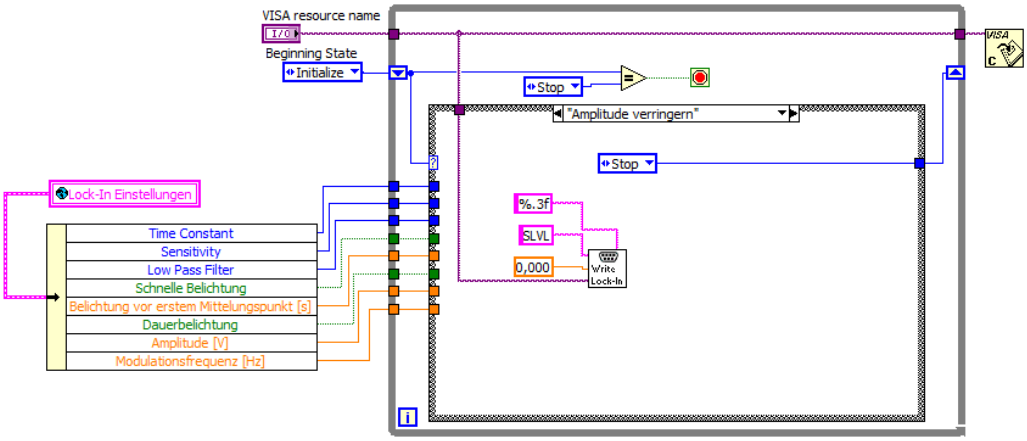

Figure 87: Block diagram of the state *Amplitude verringern* of the *Lock-In Control* SubVI.

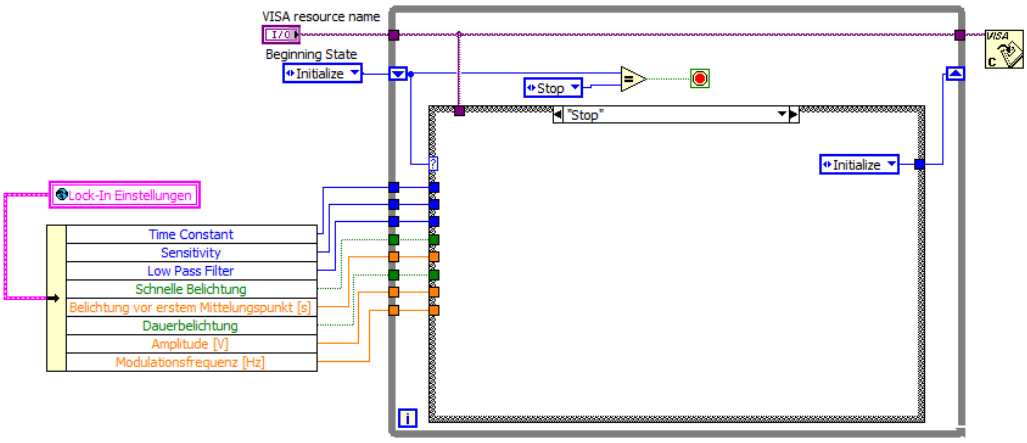

Figure 88: Block diagram of the state *Stop* of the *Lock-In Control* SubVI.

Input and output of the lock-in amplifier

The first SubVI within the SubVI *Lock-In Control* is *Lock-In Write* (see Figure 89). This VI only sets different parameters on the lock-in amplifier and does not get any output from the said amplifier. It is a fairly simply VI, which combines a command according to the syntax of the lock-in with an number, carrying the settings value and formats it according to a format string provided by its higher VI *Lock-In Control* (upper part of the block diagram). Afterwards this string is sent to the lock-in via a *VISA Write* function.

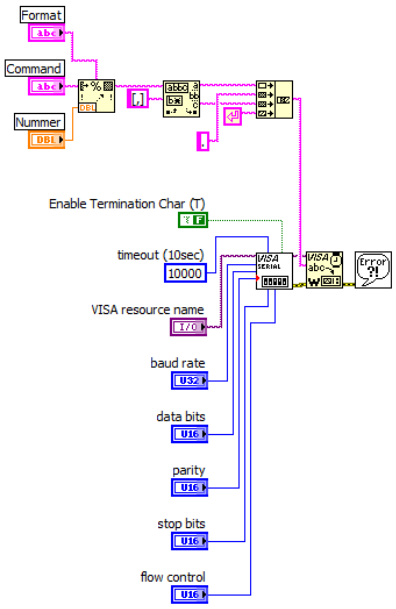

Figure 89 Block diagram of the SubVI *Lock-In Write.*

The second SubVI within the SubVI *Lock-In Control* is *Lock-In Read* (see). In contrast to *Lock-In Write,* it handles output from the lock-in amplifier, namely the measurement values of the amplitude and the phase shift. The SubVI sends a command string to the lock per a *VISA Write* function and receives after 75 milliseconds an string, which contains the information of amplitude and phase shift (middle part of the block diagram). The string is the separated into two numbers and formatted to two floating-point numbers in scientific notation with 6 significant digits. These two numbers are then sent to the superior VI *Lock-In Control*.

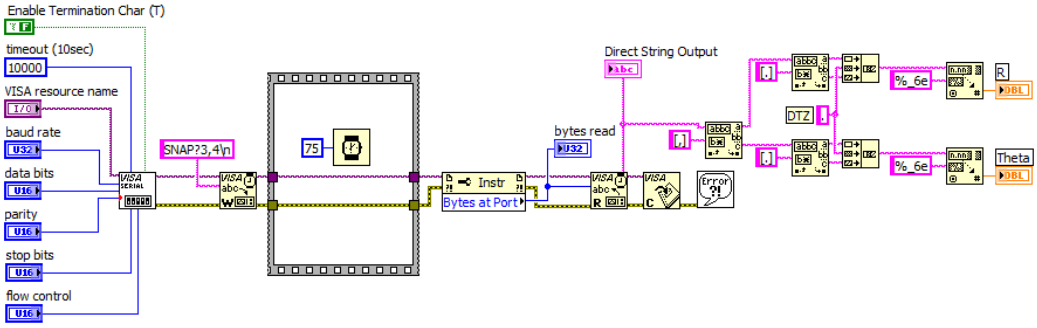

Figure 90: Block diagram of the SubVI *Lock-In Read.*

Logging of measurement values

The main core of the program is the input and output control of the lock-in amplifier, which can't be disabled like the control of the mass flow controller or the thermostat. Thus, the measurement value logging feature is directly linked to the lock-in control loop (see Figure 78 and Figure 79).

The data logging is carried out by a SubVI called *Datalogging*. It accesses measurement values from the lock-in amplifier (e.i. measured amplitude and phase shift), its derived values (demodulated intensity and decay time), timing information (CPU time of the program's start and the current measurement point) and additional information (notes and file path) directly via data wires. Other information from associated instruments (mass flow controller and thermostat) is accessed by global variables.

The block diagram of the SubVI Datalogging is shown in Figure 91. It consists of a *Format into String* function, which bundles and formats all information into one string. The data is separated by tabulators (\t in the format string wired to the top of the function) and the string is closed with an *End of Line* character (\n in the format string wired to the top of the function). The logged data is as follows:

- Current time in 24-hour format
- Elapsed time since the start of the program in seconds
- Measured amplitude in millivolt
- Demodulated intensity in arbitrary units
- Measured phase shift in arc degree

- Decay time or life time in microseconds
- Gas flow of nitrogen (carrier gas) in milliliter per seconds
- Gas flow of test gas 1 in milliliter per seconds
- Gas flow of test gas 2 in milliliter per seconds
- Temperature in degree Celsius
- Notes as ASCII string
- Thermolevel (stepnumber of thermostat schedule, when the desired temperature is reached)

The formatted string is added to the end of the logfile.

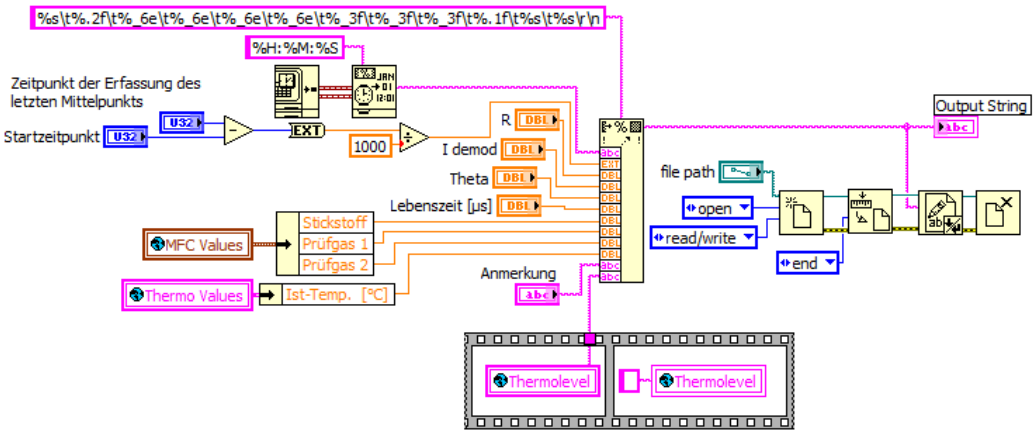

Figure 91: Block diagram of the SubVI *Datalogging*.

Control of MFCs

The mass flow controllers are controlled by a SubVI called *Massflow Sync* (see Figure 92). It is accessed in a sequence within the sixth state (*Measure and Display*) of the main VI. The SubVI (together with the SubVI controlling the thermostat) is wired to a for loop, which creates a time lag between lock-in measurement and mass flow controller access. This compensates time differences of gas flows between mass flow controllers and measurement.

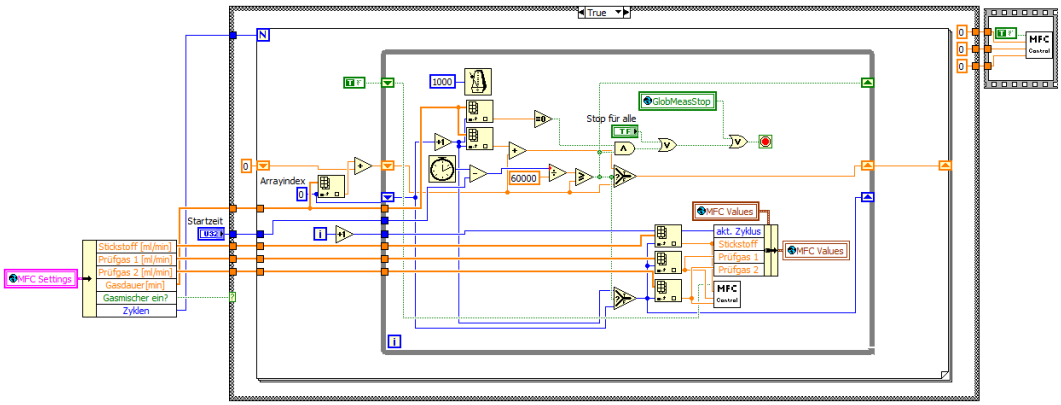

Figure 92: Block diagram of the SubVI *Massflow Sync*.

The *Massflow Sync* SubVI is responsible for the synchronization and the assigning of flow rates of each gas mixing ste to the mass flow controller. It is based on a 1000 millisecond timed While Loop. Every iteration it is checked, if the elapsed time excesses a time limit. This time limit is calculated by the system time of the start of the main program's state *Measure and Display* and the duration of every gas task. If the time limit is exceeded, the SubVI allocates the flow rates of the subsequent gas task to the mass flow controller per another SubVI called *Massflow Control* and recalculates the limit time for the new gas task. Figure 93 shows a flowchart of this loop.

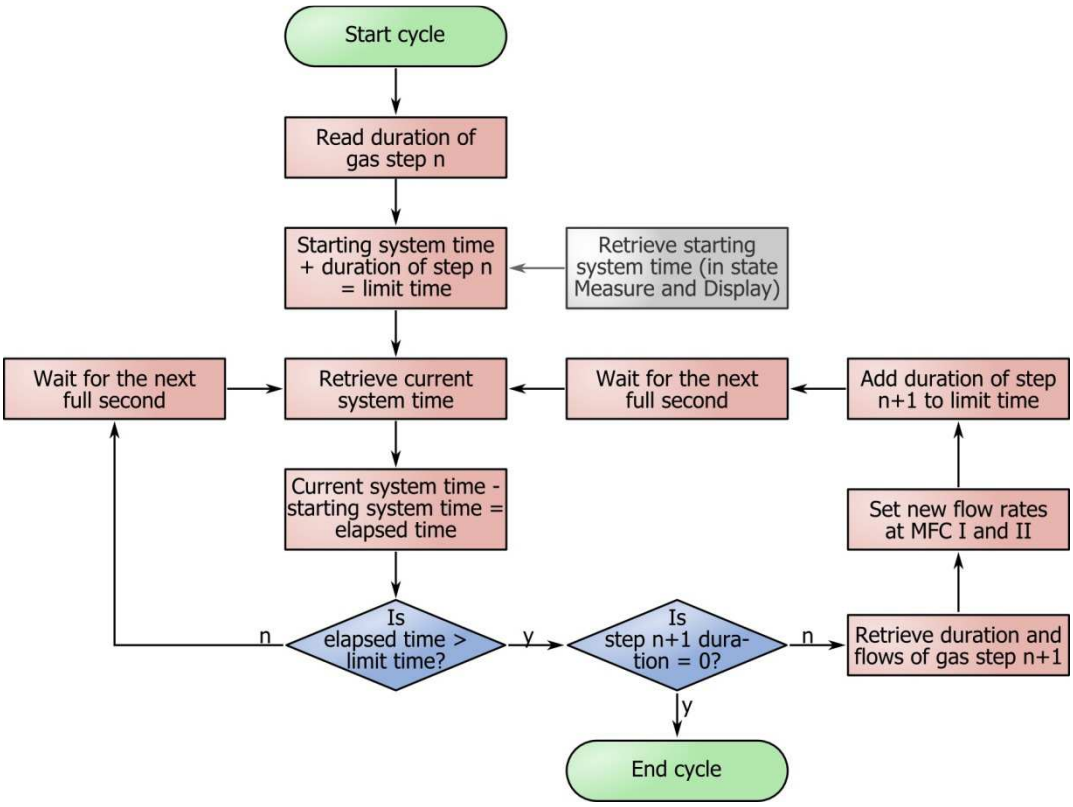

Figure 93: General synchronization and allocations scheme of the SubVI *Massflow Sync*.

The While Loop is automatically quit if the subsequent gas task would contain a flow duration value of zero minutes or it is canceled by the global variable *GlobMeasStop*. This variable can be changed by the user by using the STOP button of the main program's front panel. Before quitting, the program assigns a flow rate of zero to all mass flow controllers.

The SubVI *Massflow Control* is responsible for the allocation of gas flow rates to the mass flow controller and is executed at every iteration of the while loop. It contains a case structure, with an empty false case and a true case containing the mass flow controller interface functions. The true case is executed if the elapsed time has exceeded the limit time, thus assigning the subsequent gas task to the mass flow controllers.

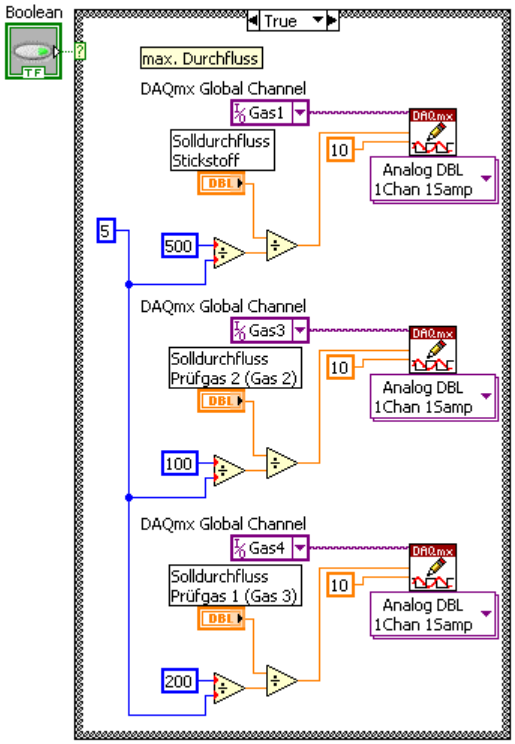

Figure 94: Block diagram of the SubVI *Massflow Control*.

The mass flow control function is based on *global virtual DAQmx Channels* and applied voltages, which ranges from zero (closed mass flow controller) to five volts (maximum flow rates, based on controller unit). These channels can be assigned in the Measurement and Automation Explorer, a program part of the LabVIEW program family, as long as the control card has been installed correctly.

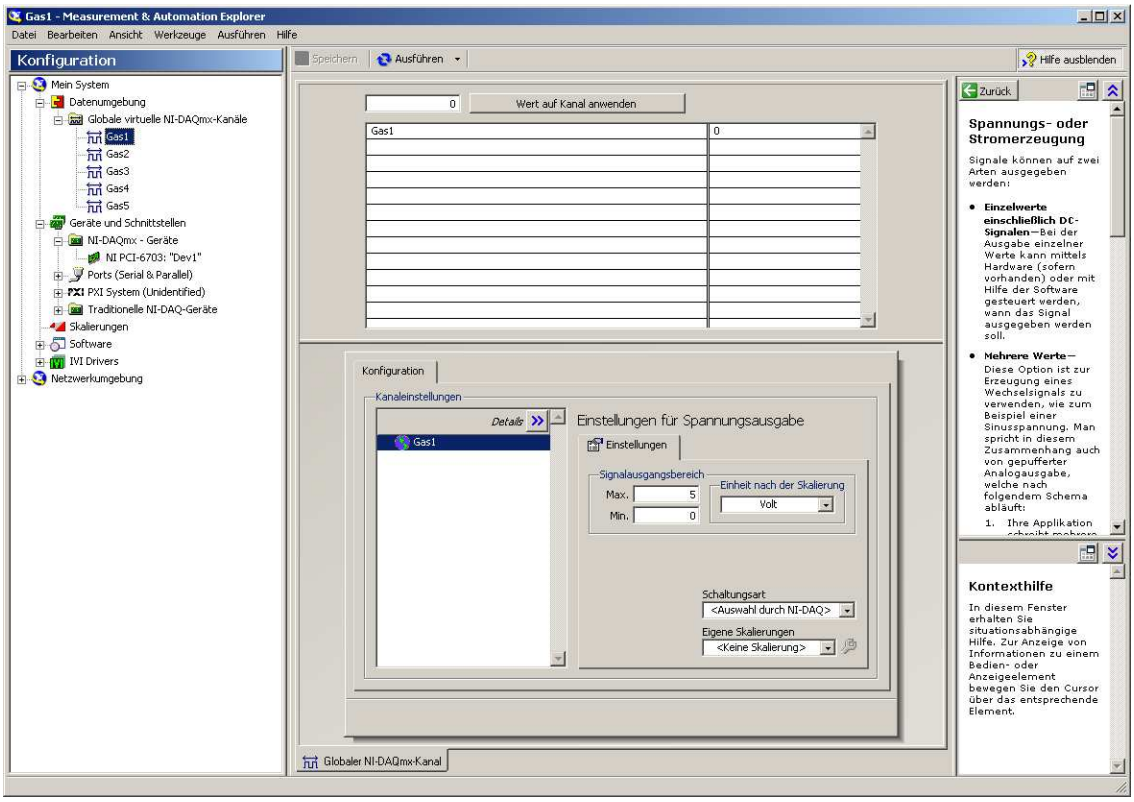

Figure 95: *Global virtual DAQmx Channels* in the Measurement and Automation Explorer.

Control of Thermostat

The SubVI (see controlling the thermostat is located in the same structure within the main program's state *Measure and Display* as the program controlling the mass flow controllers. It is designed similar to the SubVI *Massflow Sync*. The main differences are the data (only one array containing the desired temperature instead of three arrays containing three different flow rates) and an additional variable called *Thermolevel* (marking the beginning of a new temperature task in the log file).

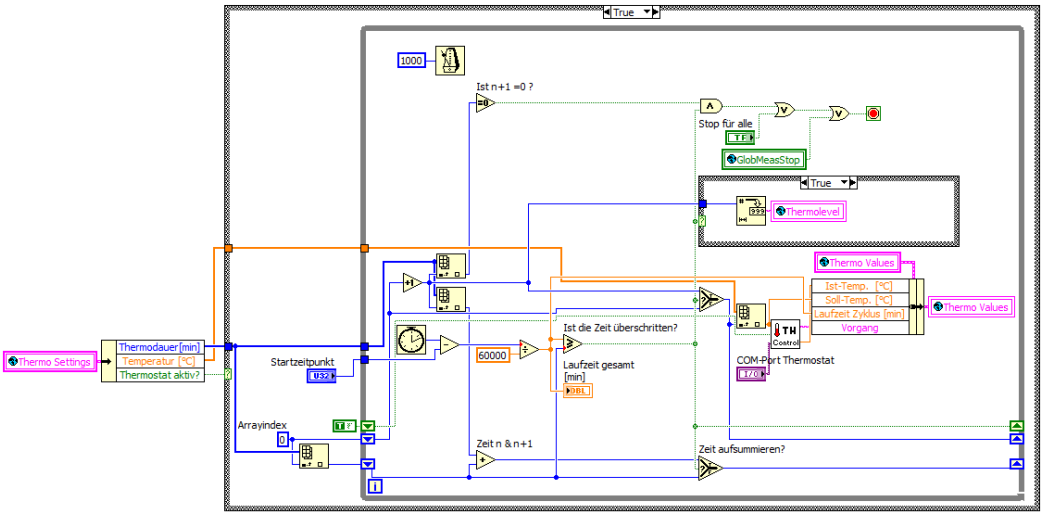

Figure 96: Block diagram of the SubVI *Thermo Sync*.

The synchronization control is identical to the synchronization control of the mass flow controller, as shown in Figure 92 and Figure 93. It is also the same system as used in the program PLATON.

Since the mass flow controllers are connected per proprietary hardware and the thermostat is connected by RS-232 cable, the program controlling the input and output of the thermostat (*Thermo Control*) differs from the program controlling the mass flow controllers. Connection instructions and communication syntax for the thermostat can be found in its manual[5].

Thermo Control consists of a small state machine with 4 states: *Temperaturmessung* (see Figure 97), *Temperaturvergleich* (see Figure 98), *Temperatur setzen* (see Figure 99) and *Stop* (empty state, not shown in a figure). In the state *Temperaturmessung* the SubVI

requests the current temperature measured by the thermostat's built-in thermometer per string code "R\sI\r"[6].

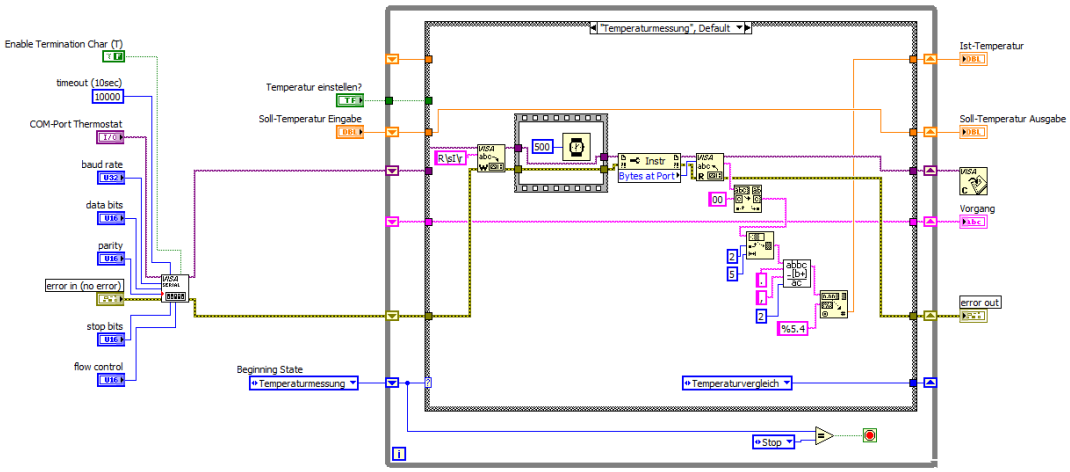

Figure 97: Block diagram of the state *Temperaturmessung* in the SubVI *Thermo Control*.

In the next state, *Temperaturvergleich*, compares the measured temperature to the programmed temperature. If both values concur within a range of ±0.1°C, the program will show the string "Temperatur konstant". If the values do not concur, the program will display the string "Ändere Temperatur".

The third state, *Temperatur setzen*, is only executed, if the VI *Thermo Sync* passed the Boolean variable "Temperatur einstellen" as TRUE. Otherwise the subsequent state to *Temperaturvergleich* would be *Stop*, which simply quits and exits the SubVI *Thermo Control*. In the state *Temperatur setzen* the program allocates a temperature to the thermostat, using the string command "W\sS0\sXX.XX\r", in which XX.XX stands for a 4 digit number with 2 decimal digits.

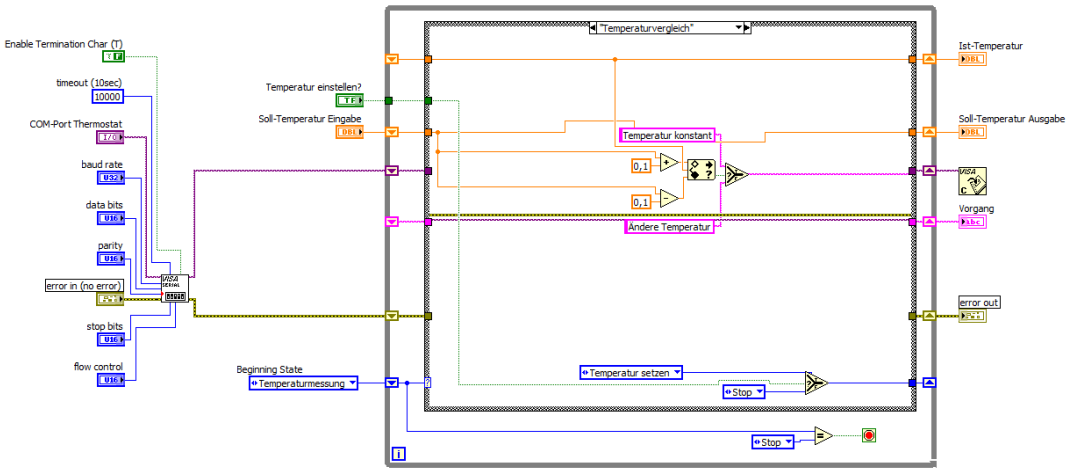

Figure 98: Block diagram of the state *Temperaturvergleich* in the SubVI *Thermo Control*.

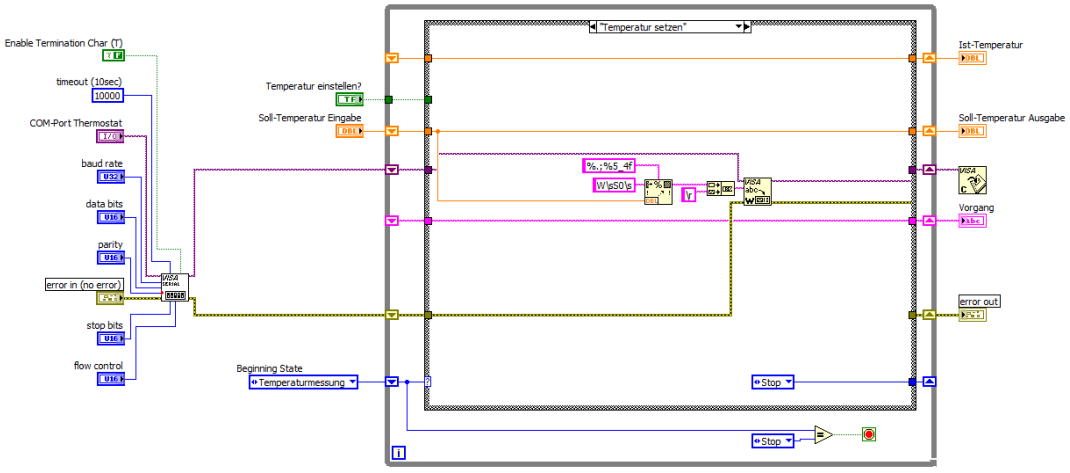

Figure 99: Block diagram of the state *Temperatur setzen* in the SubVI *Thermo Control*.

Display of current values

During the measurement the front panel of the program is updated every second with measured values. Since all three instruments are used at different sampling rates, the read-out and display of current values is based on a While Loop (Figure 100). This loop iterates every second and reads out every measurement variable. Also, this loop displays the elapsed time of the measurement, based on the system time difference of current iteration and system time of the beginning of the state *Measure and Display*.

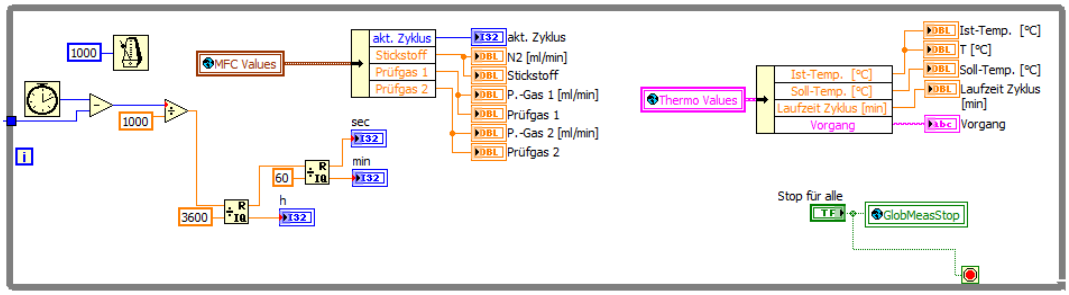

Figure 100: Block diagram of the loop, which contains all display elements

Integration

The program itself is designed to be mobile in terms of systems. It can be used on every other LabVIEW System, since no Express-VIs have been used. A conversion to earlier LabVIEW versions is necessary for the program to be used on systems based on LabVIEW 7.8 or earlier.

The control of each instrument is completely self-contained and independent from other instruments. This approach permits the integration of SOKRATES or parts of SOKTRATES into other LabVIEW-based programs.

Acknowledgement

Some parts of the program which are older were used for inspiration or even built in partially into the SOKRATES program. Specifically the SubVIs *Lock-In Write* and *Lock-In Read* are based loosely on the program “Time Drive V 2.0” by Michael Zankl from the 28th of April 1998.

---

[1] http://www.mksinst.com/product/Product.aspx?ProductID=68

[2] http://zone.ni.com/reference/en-XX/help/371361H-01/lvconcepts/glob_variables/ as of 11th of September 2012.

[3] http://digital.ni.com/public.nsf/allkb/5A5A050A3019A573862575F30061D49B as of 11th of September 2012.

[4] http://www.thinksrs.com/downloads/PDFs/Manuals/SR830m.pdf as of 12th of September 2012.

[5] http://www.thermo.fr/com/cda/product/detail/1,1055,1000000013961,00.html as of 14th of September 2012

[6] In contrast to closing characters used before (*End of Line*), the Haake DC50 demands a *Carriage Return* as closing character.

PLATON - A two channel mass flow controller unit with LabVIEW based virtual control

Abstract

Controlling gas concentrations in sensor measurements is a very crucial point for every experiment to determine gas sensor characteristics and response. The design of a two-channel mass flow controller unit and the development of a program controlling said unit is reported. The mass flow controller unit can mix two gases with a maximum flow of 200 sccm down to a 1 sccm at a maximum ratio of 100:1. The LabVIEW based program features a ten step control of both mass flow controllers, an easy communication port check and a System time based time control

Introduction

The control of the mixing ratios of gases in gas sensor measurements is a very important step. It is crucial to assure an accurate and precise mixing ratio to gain correct sensor calibration characteristics as well as quick response time of the mass flow controller (MFC) to avoid distorted sensor response times. Furthermore, exact I/O timing of the gas mixing protocol is highly desired, if other instruments are used within the experiment, which are not synchronized by the MFC program.

A two channel gas blender consisting of two MFCs has been designed and assembled and a program to control both MFCs based on LabVIEW 2009 has been programmed. The program's project name was *PLATON*.

Materials and programs

Mass flow controller

Two mass flow controller "ReadY smart series" by vögtlin instruments have been purchased (retail seller: Burde Co. Präzisionsarmaturen GesmbH, Vienna, Austria). For specifications of the MFCs see Table 4. The computer I/O was realized with an USB-to-DE9-cable and a RS-485 communication port (drivers were provided by vögtlin

instruments). The programming was carried out on a PC with Windows 7 Enterprise (6.1.7600). The whole system ist used on a PC with Windows XP Service Pack 3.

All used tubings, tee connectors and valves are made of stainless steel and are based on 6 mm metric tube systems (DIN 17458 07/85).

Table 4: Specifications of vögtlin ReadY smart thermal mass flow controller

Category	Value
Type	GSC-A4TA-BB23
Range	2-200 ln/min
Accuracy	+/-0.3% full scale /-0.5% measured value
Medium	Air
Temperature	20 °C
P inlet	1.013 bar a
P outlet	1 bar a
Fitting	G1/4" female thread
Body	Aluminium
Seal	FKM
Power supply	+24 Vdc
Setpoint	RS-485 + 4-20 mA
Output	RS-485 + 4-20 mA

Assembling

All parts have been mounted on a small, wooden plate and connected with each other. The used bending radius for the 6 mm steel tubing is about 15 mm. No specific adapters have been used for either the gas inlets or the gas mix outlet. Instead screw/band hose clamps have been used to attach plastic tubes, changing with each diameter of each specific use (e.g. microscopy, spectrometry, lab-on-a-chip). Figure 101 shows a schematic view and photos of the assembled device.

MFC driver

Drivers[1] are delivered together with the MFCs, which are – when connected to a PC – compatible with Windows XP and Windows 7. The driver allocates a communication port for the MFC at *Ports (COM & LPT)* in the Windows device manager. Communication port number, baud rate and further properties can be changed in the submenu of the Windows device manager.

MFC LabVIEW interface and communication

The core of the LabVIEW based controlling program is a LabVIEW SubVI provided by vögtlin[2]. Even though there is a detailed documentation how to embed the Sub-VI into a self-made program, the SubVI itself is unfortunately password protected. Hence, it can't be edited and even the blockdiagram can't be displayed. Specific information about this Sub-VI can't be given and the programmer has to trust vögtlin instruments and the SubVI.

Different LabVIEW SubVIs are available, designed for the use with LabVIEW 6[3] and higher, LabVIEW 8.6[4] and higher, or LabVIEW 2010[5] and higher. The SubVI based on LabVIEW 6 and higher was implemented, due to the reason, that the program can be used with older LabVIEW workstations.

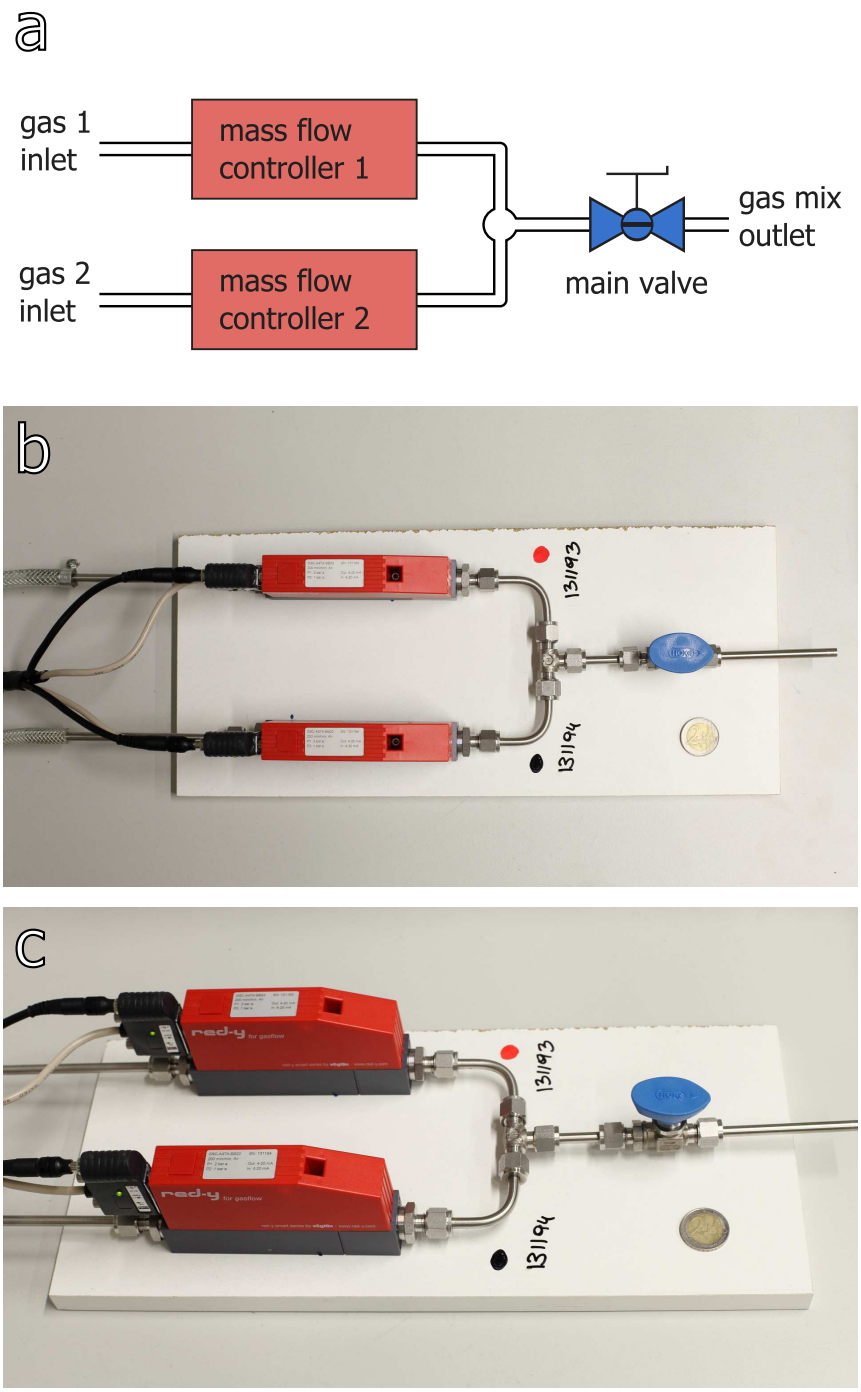

Figure 101: The assembled gas mixing unit. Sketch (a) and photos (b and c) of the assembled gas mixing unit (2 Euro coin for size comparison in the lower right corner)

LabVIEW based control program

Interface

The program's interface (front panel) is a non-tabbed, non-dynamic, single-window program with an emphasis on usability. It is shown in Figure 102. It is built up of 4 parts. The main part on the left consists of an array for different gas flow rates and times, and a control field for the number of cycles. The remaining 3 parts on the right side are responsible for communication port allocation and identification, for displaying actual gas cycles, rates, and elapsed time, and for main control per start and stop button. To simplify the use of the program each interface will be grayed out if it can't be used at any specific moment during the program's execution.

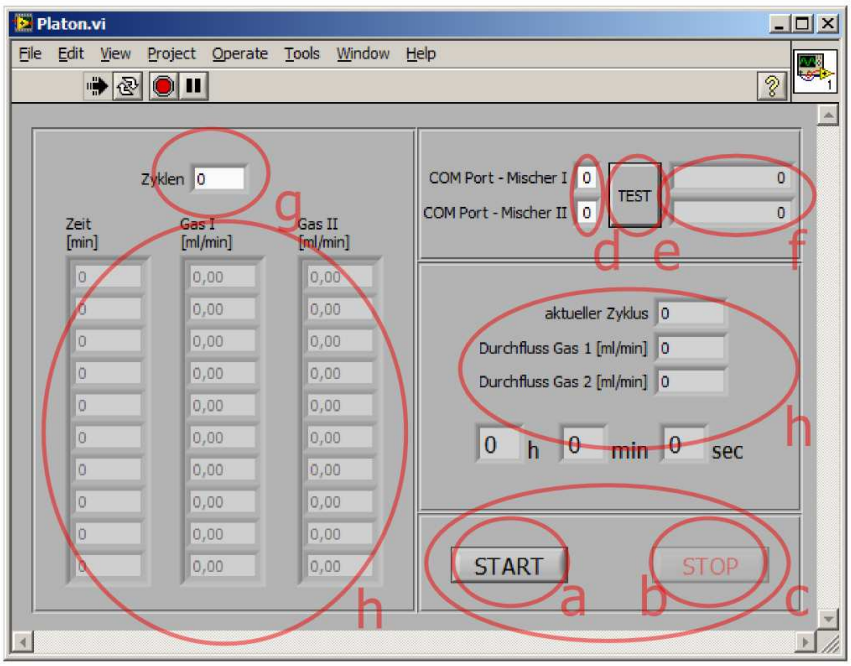

Figure 102: Front panel (user interface) of PLATON.Start (a) and Stop (b) button for the main command (c) of the program. Communication port (d) and test button (e) for the display MFC's serial numbers (f). Number of gas cycles (g) and array for gas flow rates and times (h).

Main design

The main design of the block diagram is based on a state machine with 5 different states. The state machine is timed by a 50 millisecond cycle and can be stopped at any time during the *Gasrun* state. They states are as following:

- **Initialize**: The state *Initialize* is the default and first state, which is only executed once. It is followed by the *Wait for Input* state. The state is responsible to assign the right enable states and values to the interface buttons.
- **Wait for Input**: The second state is executed repeatedly. In this state the user can assign used communication ports, gas flow rates and times and gas cycles. This state can be left by entering the *Initialize Gasrun* state (pressing START button) or by entering the *Check Ports* state (pressing TEST button).
- **Check Ports**: This state is optional and is activated by the user action of pressing the TEST button. In this state the MFCs return their serial number, which is also noted on the MFC unit to identify the different MFCs or gas flows. If incorrect communication ports have been entered, no serial numbers will be returned. This state is executed once and is succeeded by the *Wait for Input* state.
- **Initialize Gasrun**: This state is activated by the Boolean change of the START button and is only executed once. It is followed by the *Gasrun* state.
- **Gasrun**: This state is the main state for the program control. It controls the MFCs input and output, as well as the display of current gas flows and elapsed time. It will be automatically left by the program at the end of the last gas cycle or by the user action of pressing the STOP button.
- **Stop**: This state is either automatically entered after the last step of the last gas cycle from the state *Gasrun* or will be entered by the user action of pressing the STOP button. It shuts down both gas flows and ends the program.

Figure 60 shows an overview of the used states and their sequence.

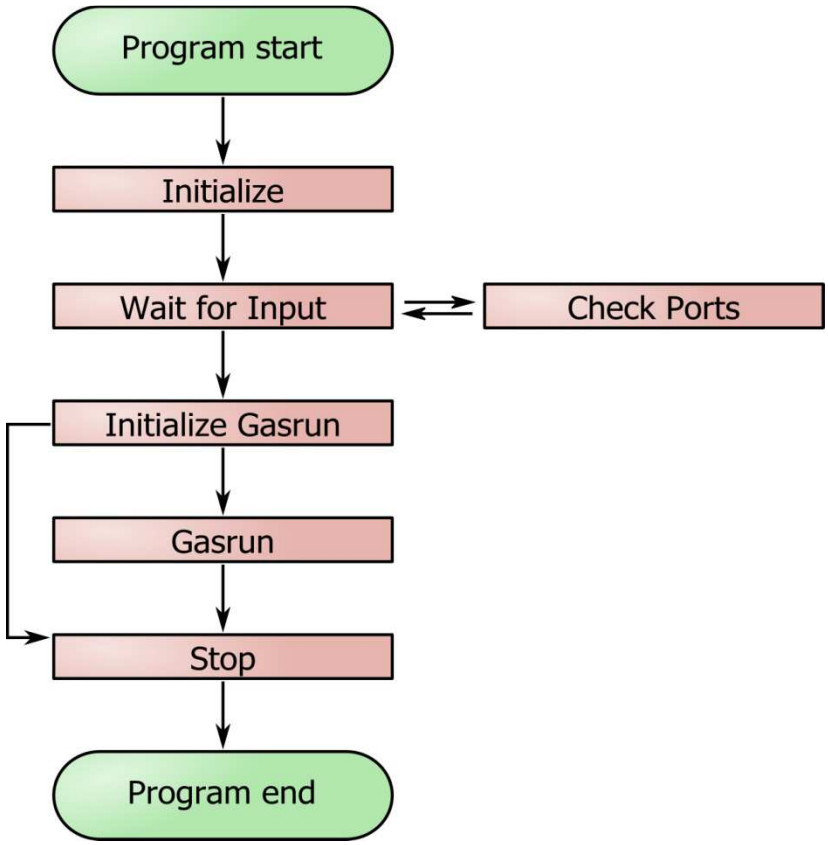

Figure 103: Sequence of states used in PLATON

Following every state will be described together with its block diagram.

State “Initialize”

The first state is the default state and the program starts without exception with this state. As to be seen on the left side in Figure 104, outside of the while loop the beginning state is marked as *Initialize.*

On the upper right hand corner a *Wait (ms)* function and an integer constant of 50 defines the state machine cycle time (50 ms). The *Wait (ms)* function should not be used for exact synchronization purposes during the *Gasrun* state, but within the states prior to the gas control no time precision is needed. The routine for stopping the whole program can be seen on the bottom of the while loop.

Inside the case structure three property nodes control the values and enable states of the three buttons within the front panel: start, stop and test. This state is succeeded by the state *Wait for Input* as seen on the right side.

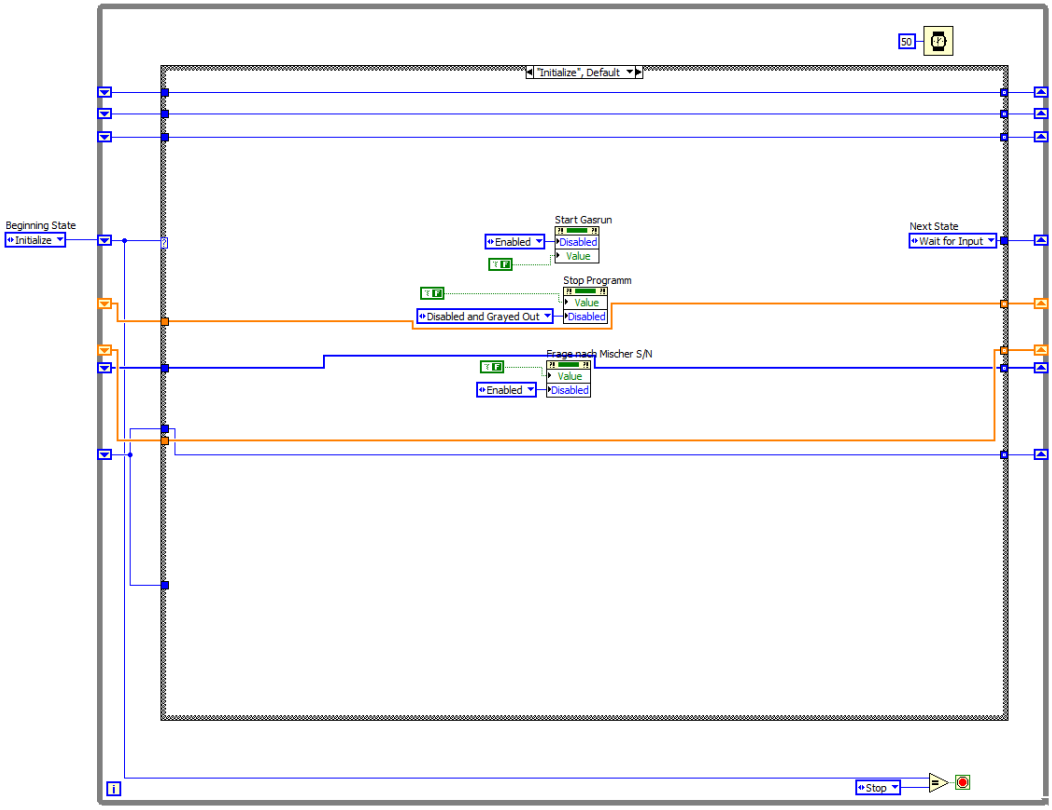

Figure 104: Block diagram of the state *Initialize*.

State “Wait for Input”

The second state is *Wait for Input* (see Figure 105).This state is repeated every 50 milliseconds and only changes to another state by the user’s actions of either triggering the start or test button to enter the *Check Ports* or *Initialize Gasrun* states (see middle part of the case structure).

All input elements are placed on the right side of the case structure, beginning from the top: the number of cycles of the gas program (*Zyklen*), the communication port number of both MFCs (*COM Port – Mischer I* and *COM Port – Mischer II*), the arrays for the flow rates of both MFCs (*GAS I [ml/min]* and *GAS I [ml/min]*) and the duration time for each step (*Zeit [min]*). All input elements pass their information to a shift register on the right side of the While Loop. Since the elements are only active within this frame, changes in later states won’t be considered by the program.

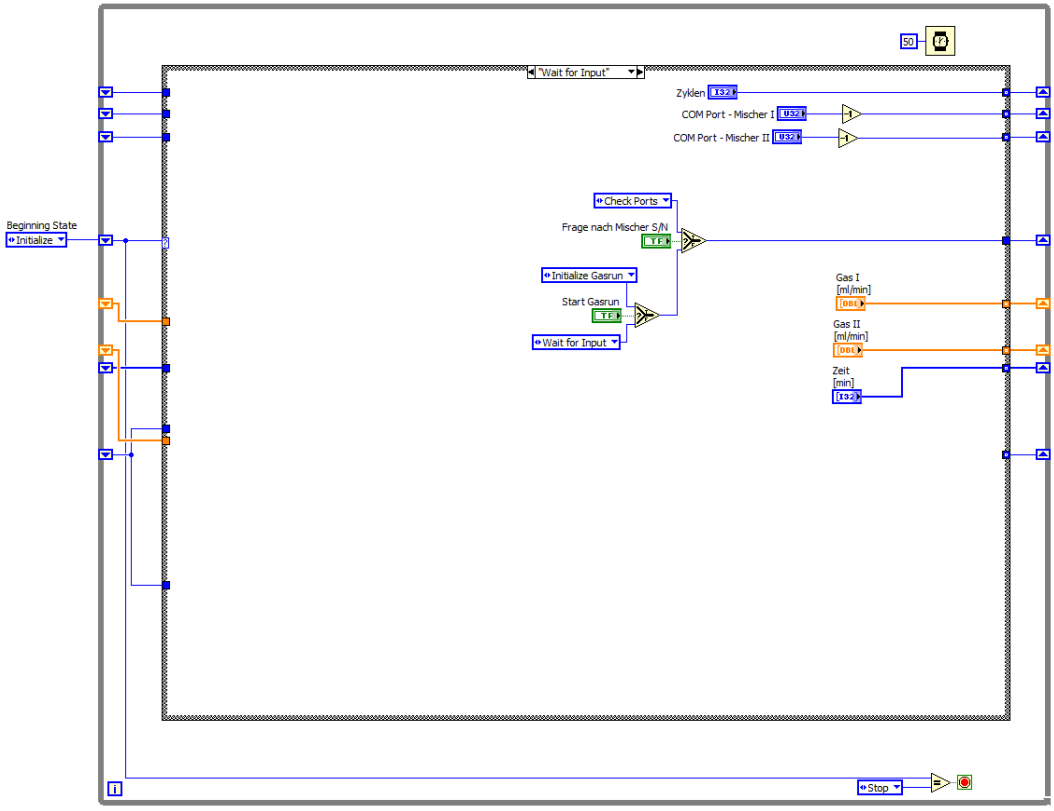

Figure 105: Block diagram of the state *Wait for Input*.

State “Check Ports”

The state *Check Ports* (see Figure 106) is entered by the user action of pressing the test button on the front panel. This state is executed only once and afterwards the program will return to the *Wait for Input* state. The state duration is 50 milliseconds.

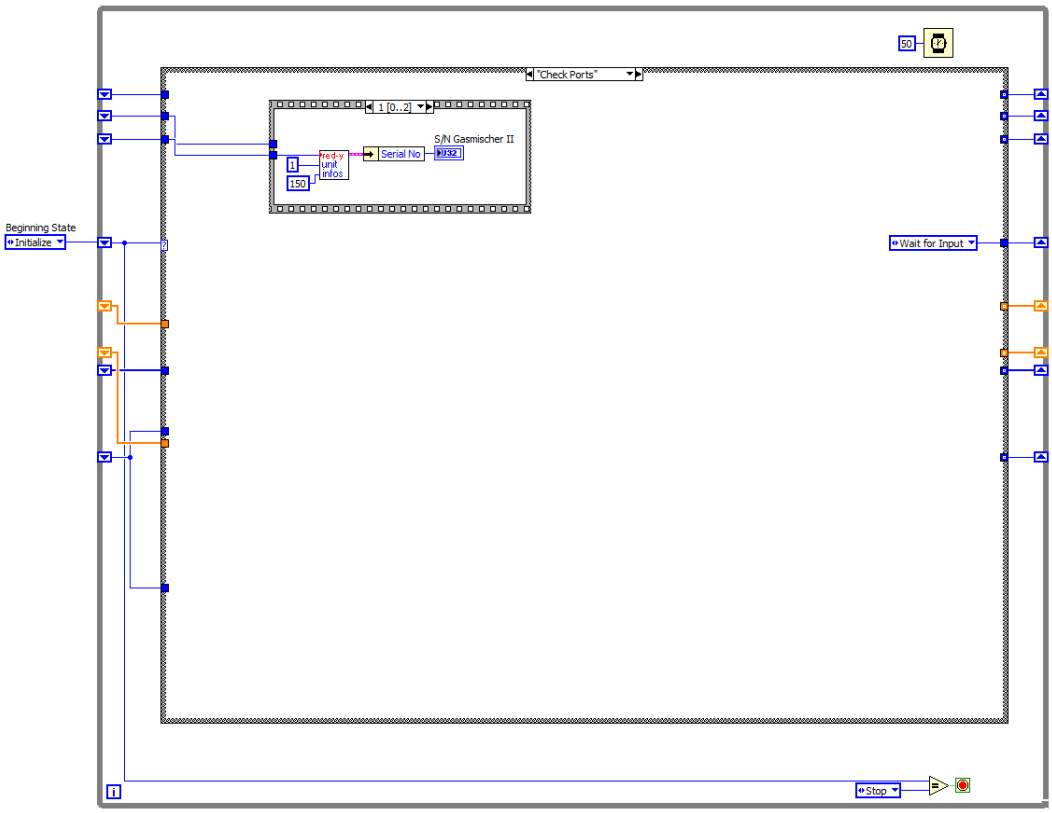

Figure 106: Block diagram of the state *Check Ports*.

The task of this state is the retrieval of the MFCs serial numbers. The necessary user input are the (assumed) port numbers, which are the second and third data nodes on the upper left side of the case structure. The serial numbers are accessed within a stacked sequence based on the port numbers. In the first and second frame of the sequence (Figure 107a and b) the serial numbers are retrieved and displayed in the numeric indicators *S/N Gasmischer I* and *S/N Gasmischer II*. Afterwards the Boolean state of the

test button is set back to false (which has been set to true by the user to activate the *Check Ports* state).

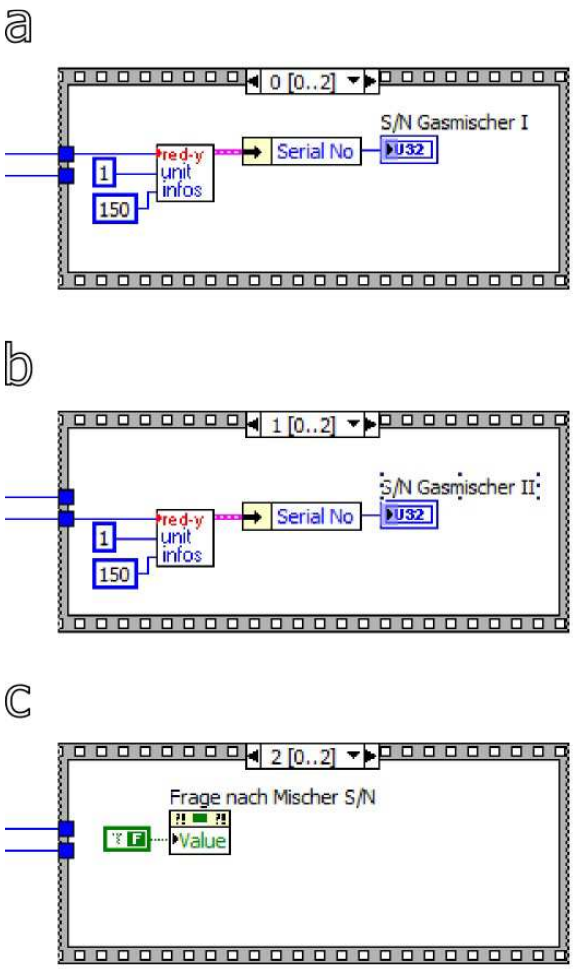

Figure 107: Stacked sequence of the Check Ports state for retrieving the serial numbers of the MFCs

If incorrect communication port numbers have been entered by the user, no serial number will be displayed and the program will return to the *Wait for Input* state. It is possible for the user to then change the communication port numbers and call the *Check Ports* state again.

State “Initialize Gasrun”

If the correct communication ports have been assigned, a gas mixing schedule is entered, and the button START is pressed, the program will change to the state *Initialize Gasrun*. It is only executed once and will be succeeded by the state *Gasrun*.Similar to the *Initialize* state, this state is responsible to manage the front panel usability. Three property nodes control the values and states of the three buttons on the front panel: The start and the check ports button are deactivated, since they are not used anymore in further states and the stop button will be activated (for the first time in the program). The system time is also noted, as to be seen in Figure 108 on the right side in the case structure. This is necessary to synchronize the gas schedule

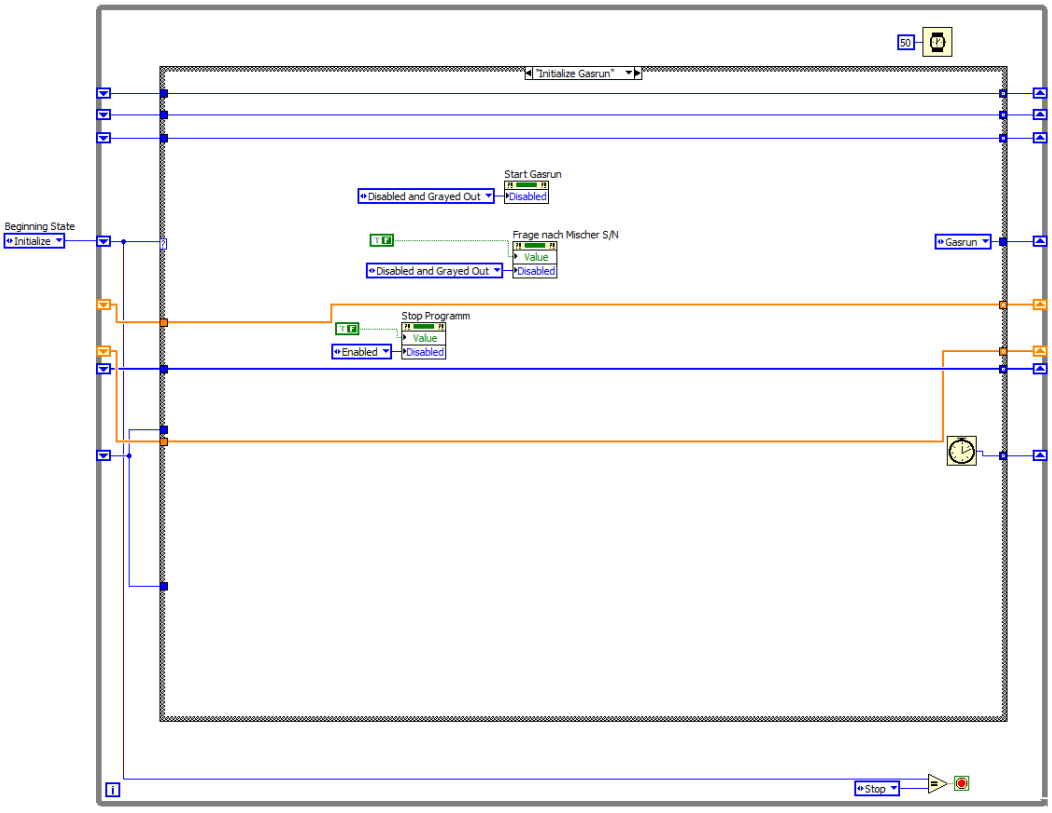

Figure 108: Block diagram of the state *Initialize Gasrun*.

State “Gasrun”

This state is the main state of the program and responsible for input of the different steps of a gas mixing schedule, and output/ display of current gas flows and elapsed time.

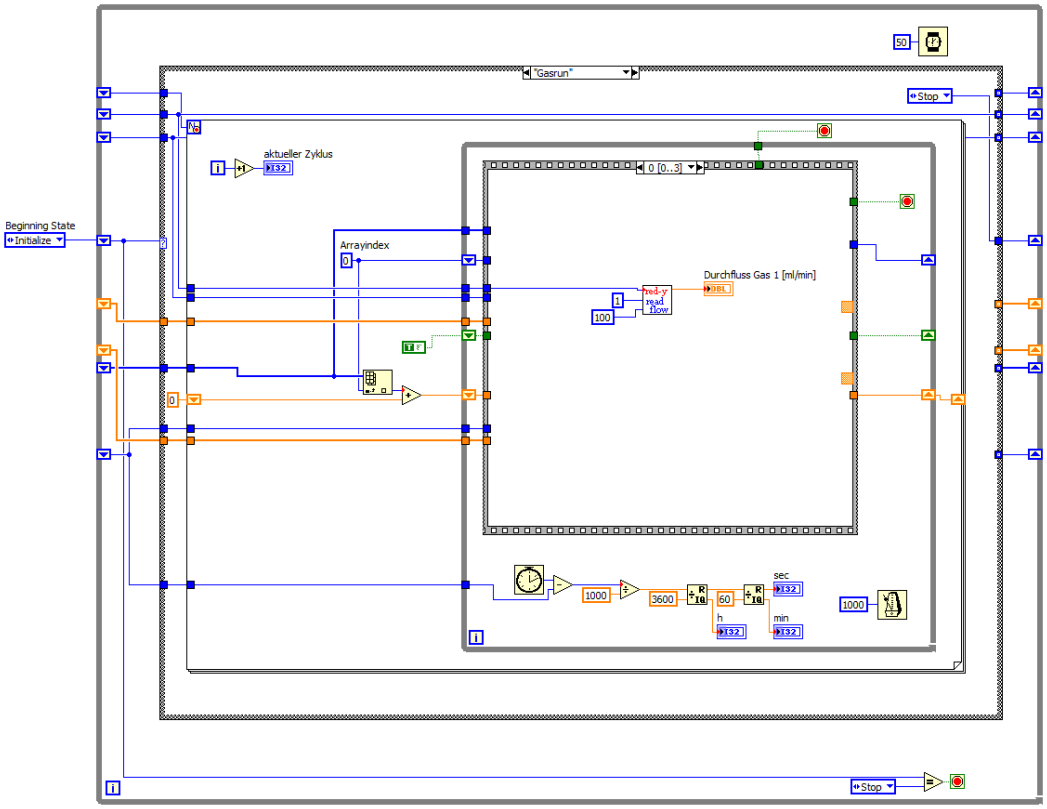

Figure 109: Block diagram of the state Gasrun.

The case structure of this state consists of a For Loop which contains and *Index Array* function of the Zeit [ms] Array, a Loop count which displays the actual cycle number, a Boolean true constant and a While Loop inheriting the gas schedule control (see Figure 109).

The While Loop consists of three main parts: A *tick count* function (current system time) which calculates the elapsed time since the first execution of the While Loop based on the system time noted in the state *Initialize Gasrun*, a *Wait Until Next ms Multiple* function with an integer constant of 1000 to synchronize the gas schedule to every second

(1000 milliseconds) and a *stacked sequence*, which inherits the further gas schedule control.

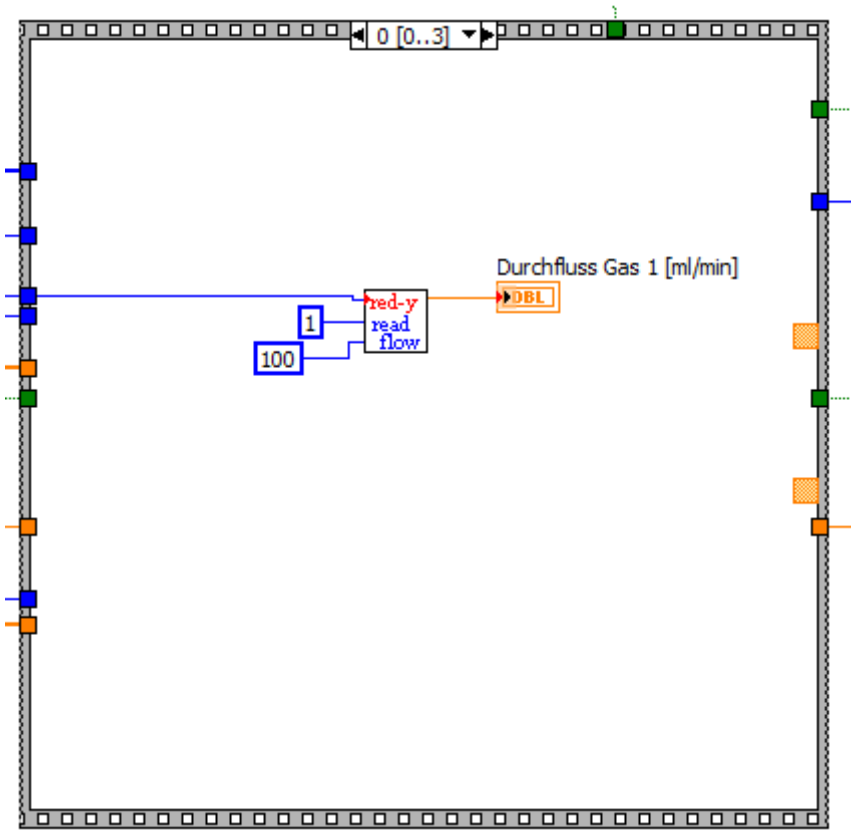

Figure 110: Block diagram of the first sequence window of the gas schedule control within the state *Gasrun*.

The first two windows of the stacked sequence (window zero and one, see Figure 110 and Figure 111) are responsible for an I/O operation to display the current flow rates in every cycle (each second). Window 0 and window 1 queries and displays the current flow rate of MFC I and MFC II respectively.

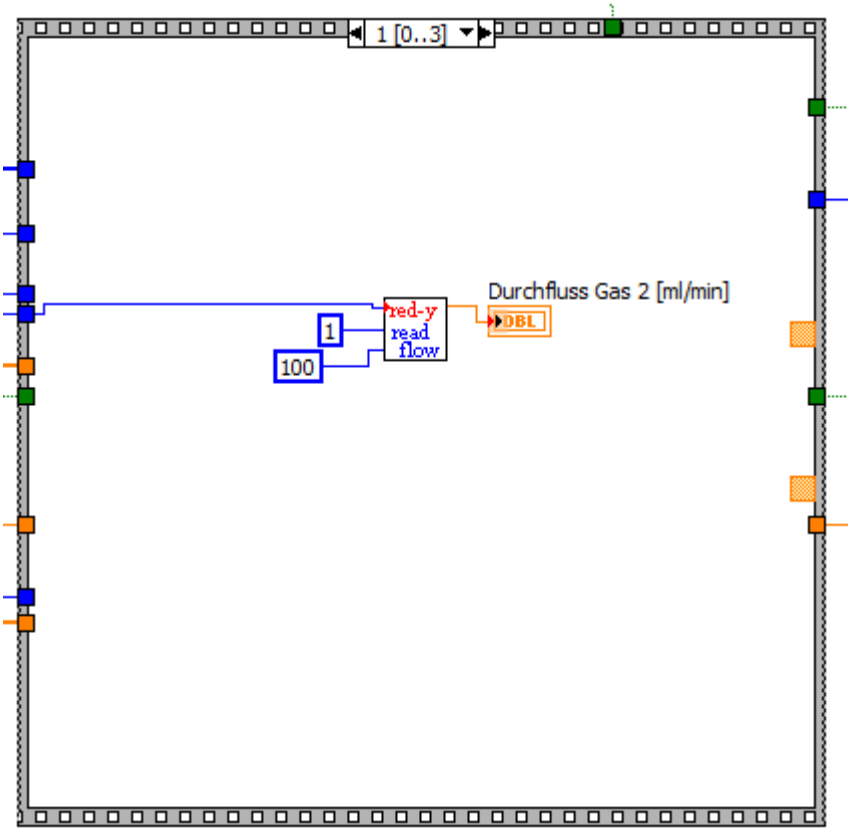

Figure 111: Block diagram of the second sequence window of the gas schedule control within the state *Gasrun*.

It is useful to display the measured flow rate every second, but not necessary to send every second the same input of flow rates. To avoid this, window three of the gas schedule control sequence (Figure 112) contains a logical sequence to control at each loop iteration if the end of the duration of the currently executed gas mixing step has been reached and the next step in the array has to be executed, or if no change in flow rates is necessary. Furthermore the loop tests at each execution, if the next step in the array has duration of 0 minutes. If this is true and the end of the currently executed gas mixing step has been reached, the *While Loop* (current cycle) will be quit and ended. See the chart in Figure 113 for a better understanding of the logical sequence of window two.

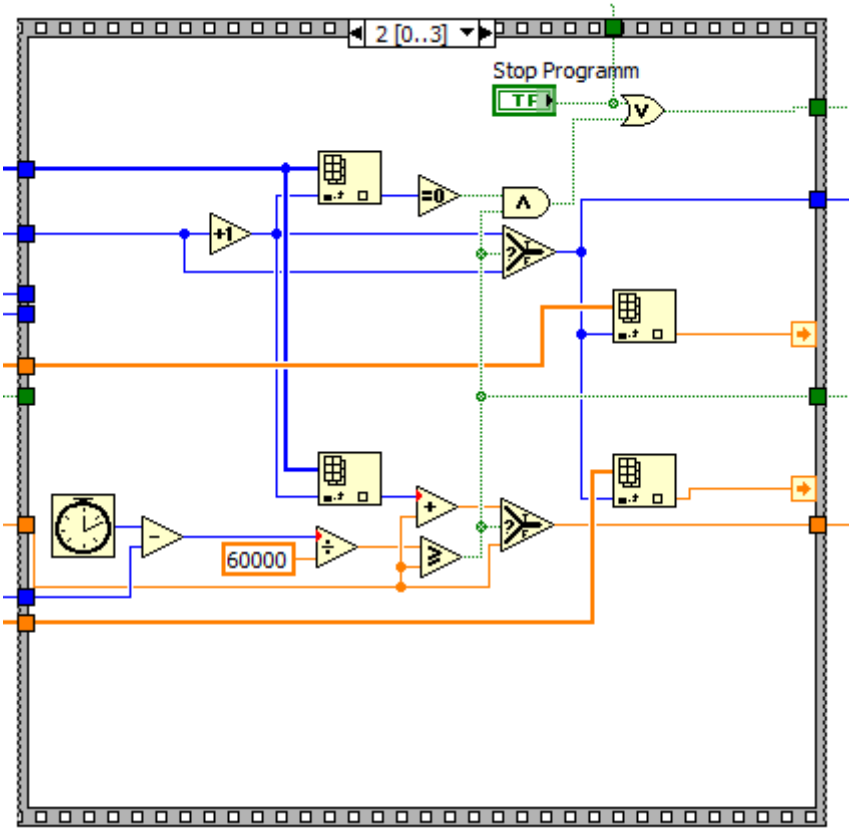

Figure 112: Block diagram of the third sequence window of the gas schedule control within the state *Gasrun*.

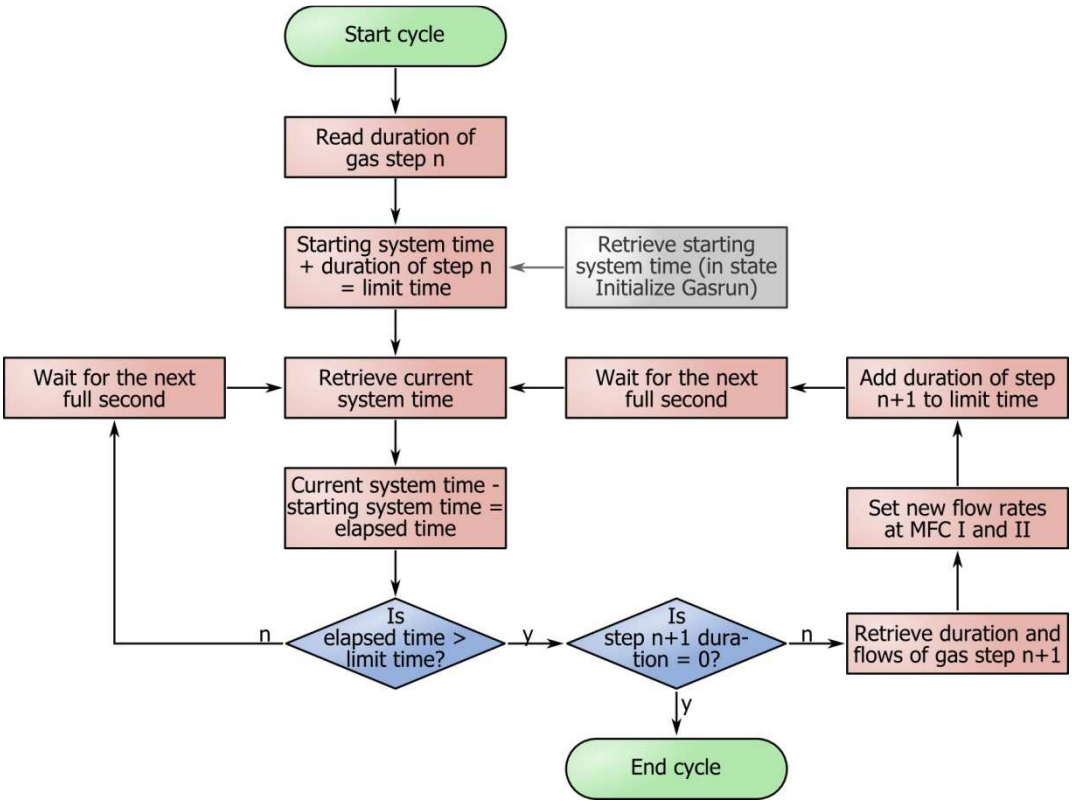

Figure 113: Schematic view of the logical function of sequence window 3 (Figure 112).

The fifth and last window (window three) of the gas control sequence contains a case structure. The “false” case contains no functions and is executed if no new flow rates have to be assigned to the MFCs. The “true case” contains a 2-window stacked sequence, containing the vögtlin SubVI to assign new flow rates. Each window assigns flow rates to one MFC.

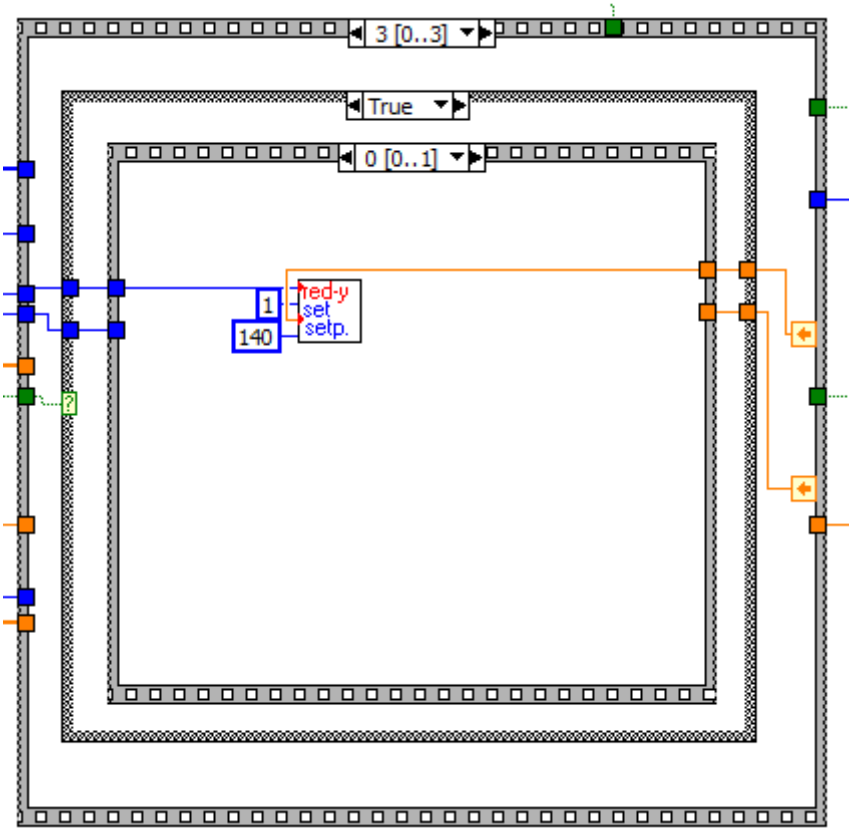

Figure 114: Block diagram of first sequence window within true case of the fourth sequence window of the gas schedule control within the state *Gasrun.*

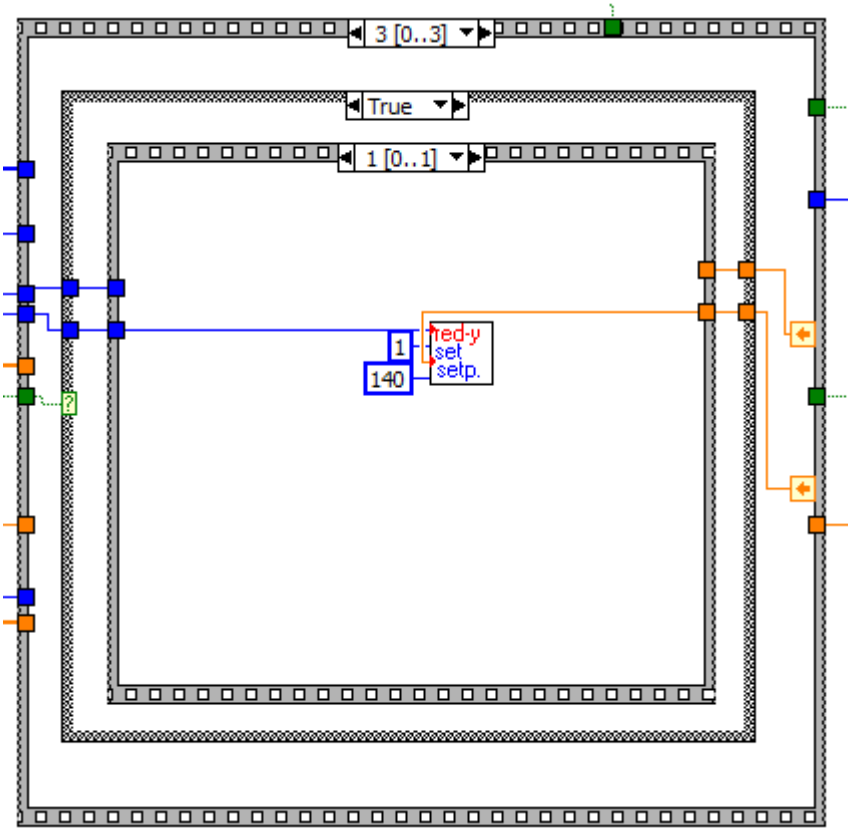

Figure 115: Block diagram of second sequence window within true case of the fourth sequence window of the gas schedule control within the state *Gasrun.*

The *While Loop* containing the gas control sequence is placed inside a *For Loop*, which will be executed for as many times, as the user has assigned it in the associated control field (see Figure 102, part g). If all loops are finished and closed, the state will automatically be succeeded by the state *End*.

State “End”

The state *End* is the last state and closes the program PLATON after being executed one time. It contains a 2 window flat sequence, which closes both MFCs by assigning a flow rate of 0.

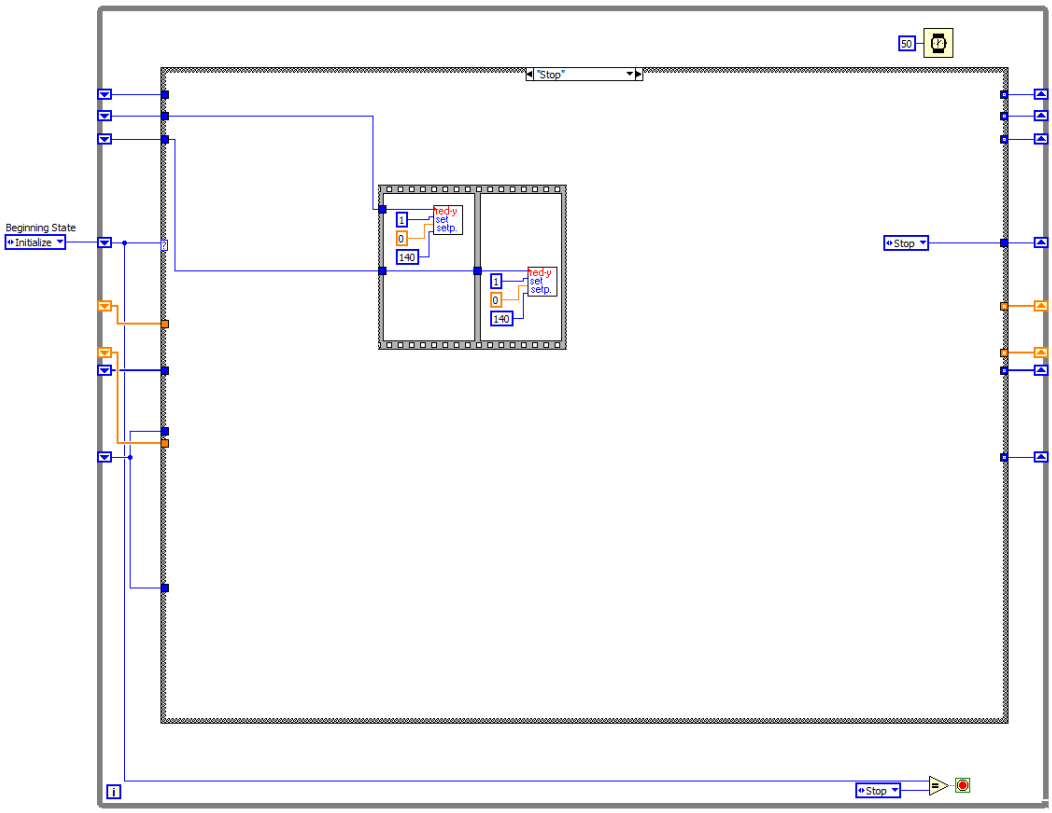

Figure 116: Block diagram of the state *End*.

Adaptability

Since no complex structures, functions or variables have been used, the program itself is easily integrated as SubVI into other programs. The design as state machine also allows integrate further states to control other instruments and expand the functionality of this program.

---

[1] http://vögtlin.sharepointhosting.ch/DOCUMENTS/PDM-U.zip (28th of August, 2010)

[2] http://vögtlin.sharepointhosting.ch/DOCUMENTS/Forms/SoftwareRedy.aspx (28th of August, 2010)

[3] http://vögtlin.sharepointhosting.ch/DOCUMENTS/LabVIEW_6.zip (28th of August, 2010)

[4] http://vögtlin.sharepointhosting.ch/DOCUMENTS/LabVIEW_8_6.zip (28th of August, 2010)

[5] http://vögtlin.sharepointhosting.ch/DOCUMENTS/LabVIEW_2010.zip (28th of August, 2010)

List of figures

List of tables

Table of abbreviations

a. u.: arbitrary units
boPET: Biaxially-oriented polyethylene terephthalate
BPB: Bromophenol Blue
Bphen : 4,7-diphenyl-1,10-penantroline
C545T: Coumarin 545T
CA: cellulose acetate
CCD: Charge-Coupled Device
CHES: N-Cyclohexyl-2-aminoethanesulfonic acid
CMOS: Complementary Metal–Oxide–Semiconductor
Coumarin 30 or C30
CTAC: Hexadecyltrimethylammonium chloride
CuPc: Copper(II)phthalocyanine
DAQ: Device Acquisition
DLR: Dual Lifetime Referencing
EC: Ethyl Cellulose
EL: Emitting Layer
ETL: Electron Transport Layer
FRET: Förster Resonance Energy Transfer
HOMO: Highest Occupied Molecular Orbital
HPTS: 8-Hydroxypyrene-1,3,6-trisulfonic acid
HPTS-Na: 8-Hydroxypyrene-1,3,6-trisulfonic acid trisodium salt
HTL: Hole Transport Layer
IC: Internal Conversion
ISC: Intersystem Crossing
ITO: Indium Tin Oxide
LED: Light Emitting Diode
LED: Light Emitting Diode
LUMO: Lowest Unoccupied Molecular Orbital
mCP: m-Cresol Purple

MES: 2-(N-morpholino)ethanesulfonic acid

MFC: Mass Flow Controller

MFR: Macrolex Fluorescent Red G

MFY: Macrolex Fluorescent Yellow 10 GN

MOPS: 3-(N-morpholino)propanesulfonic acid

NI: National Instruments

OLED: Organic Light Emitting Diode

OPD: Organic Photo Detector

P_1-t-Oct: tert-Octylimino-tris(dimethylamino)phosphorane

PdTFPP: Palladium(II) 5,10,15,20-meso-tetrakis-(2,3,4,5,6-pentafluorphenyl)-porphyrin

PEDOT:PSS: Poly[3,4-(ethylenedioxy)-thiophene]:poly(styrene sulfonate

PMT: Photomultiplier Tube

PTCBi: 3,4,9,10-perylenetetracarboxylicbisbenzimidazole

PTFE: Polytetrafluoroethylene

PtTFPP: Platinum(II) 5,10,15,20-meso-tetrakis-(2,3,4,5,6-pentafluorphenyl)-porphyrin

TEOS: Tetraethoxysilane

THF: Tetrahydrofuran

TOA: Tetra-N-octylammoinum

TOA^+Cl^-: Tetra-N-octylammoinum chloride

TOA^+OH^-: Tetra-N-octylammoinum hydroxide

TWR: Two Wavelength Referencing